1994

Photodissociation and photoionization of organosulfur radicals

Chia-Wei Hsu
Iowa State University

INFORMATION TO USERS

This manuscript has been reproduced from the microfilm master. UMI films the text directly from the original or copy submitted. Thus, some thesis and dissertation copies are in typewriter face, while others may be from any type of computer printer.

The quality of this reproduction is dependent upon the quality of the copy submitted. Broken or indistinct print, colored or poor quality illustrations and photographs, print bleedthrough, substandard margins, and improper alignment can adversely affect reproduction.

In the unlikely event that the author did not send UMI a complete manuscript and there are missing pages, these will be noted. Also, if unauthorized copyright material had to be removed, a note will indicate the deletion.

Oversize materials (e.g., maps, drawings, charts) are reproduced by sectioning the original, beginning at the upper left-hand corner and continuing from left to right in equal sections with small overlaps. Each original is also photographed in one exposure and is included in reduced form at the back of the book.

Photographs included in the original manuscript have been reproduced xerographically in this copy. Higher quality 6" x 9" black and white photographic prints are available for any photographs or illustrations appearing in this copy for an additional charge. Contact UMI directly to order.

UMI

University Microfilms International
A Bell & Howell Information Company
300 North Zeeb Road, Ann Arbor, MI 48106-1346 USA
313/761-4700 800/521-0600

Order Number 9503564

Photodissociation and photoionization of organosulfur radicals

Hsu, Chia-Wei, Ph.D.

Iowa State University, 1994

Photodissociation and photoionization of organosulfur radicals

by

Chia-Wei Hsu

A Thesis submitted to the

Graduate Faculty in Partial Fulfillment of the

Requirements for the Degree of

DOCTOR OF PHILOSOPHY

Department: Chemistry
Major: Physical Chemistry

Approved:

Signature was redacted for privacy.

In Charge of Major Work

Signature was redacted for privacy.

For the Major Department

Signature was redacted for privacy.

For the Graduate College

Iowa State University
Ames, Iowa

1994

TABLE OF CONTENTS

ACKNOWLEDGEMENTS

Many people have helped me during my Ph.D. studies at Iowa State University. In these past five years, a great deal of assistance from many people has led to my success in graduate school. At this time, I would like to express my cordial appreciation to them.

First, I deeply thank Dr. Ng for his support, understanding, assistance and encouragement in my research. To be frank, I received a lot pressure from Dr. Ng ever since I joined his group. The most frequent words he said to me were " Are you doing O.K? ". Whenever I heard these words I felt I needed to accomplish something before I met him the next time. It was this motivation that really inspired me and had a tremendous impact on my life. His past guidance will continue to benefit me for the rest of my life.

I would also like to thank Chung-Lin Liao for his assistance in my academic studies. He also taught me how to do the experiments from the very beginning. He is very thorough and knowledgeable, and always comes up with ingenious ideas to solve experimental difficulties. I improved my skill and knowledge in science through work and discussion with him. I acknowledge Jerry Flesch for helping me to safely pass some very difficult times during my work in Ames Lab. He also took care of every detailed work in our lab. Without him, my work would surely have been delayed. I acknowledge Chu-Xiong Liao for helping me in fixing the apparatus. He patiently explained problems to me whenever I came to ask him for help. I also thank Eldon Ness, Terry Soseman, and Dick Egger in the chemistry machine shop for their invaluable service. They were always helpful and friendly and did an excellent job in the construction of my apparatus. I

especially thank Eldon for his understanding and suggestions as well as for rapidly completing my job whenever it was urgent.

Finally, I deeply thank my family for their support and understanding. My wife, I-Quei Wang, has given me a lot of support and encouragement. She took care of the family very well so that I could concentrate on my work. She always encouraged me to do my best whenever I encountered difficulties. Her support for my study keeps me striving for success.

This work was performed at Ames Laboratory under contract no. W-7405-eng-82 with the U.S. Department of Energy. The United States government has assigned the DOE Report number 1709 to this thesis.

GENERAL INTRODUCTION

Explanation of the Thesis Format

The thesis is composed of five papers prepared in a format ready for publication. The tables, figures, and references mentioned in each paper pertain only to that paper. The specific experimental conditions used in each study are described in each paper. The references quoted in the general introduction and general conclusion are listed after the general conclusion. The appendix contains the computer programs used for the simulation of the experimental data.

Background

Sulfur, which occurs naturally in crude oil and coal in the range from 0.2% to 10%, is an important species contributing to air pollution in the atmosphere. The modelings of the combustion and oxidation of sulfur compounds represent important steps for the control of both the production and the elimination of sulfur-containing pollutants[1]. The studies of the photodissociation and photoionization of H_2S and organosulfides like CH_3SH and CH_3SSCH_3, etc., have been major subjects in our group[2-6]. They have provided valuable information on the energetics and photochemical processes of these molecules. However, the study of the intermediate reactive radicals, such as SH and CH_3S, remains an open area in research, mainly due to their instability. In a continuing effort to study organosulfur compounds, I focused my attention primarily on the studies of these two radicals.

The first three papers of the thesis contain the photodissociation studies of CH_3S,

SH , CH_3SH, and H_2S. Basically, these experiments directly measure the nascent electronic state distributions of $S(^3P_{2,1,0};^1D_2)$ atoms formed in the 193 nm photodissociation of CH_3SCH_3, H_2S, and CH_3SH using 2+1 resonance-enhanced multiphoton ionization (REMPI) detection schemes[7-9]. Using the rate equation scheme, we have estimated the 193 nm photodissociation cross section of the nascent radicals CH_3S and SH initially formed in the photodissociation of CH_3SCH_3, H_2S, and CH_3SH. To our knowledge, this is the first report on the absolute photodissociation cross sections at 193 nm for these radicals. The dominant product from CH_3S is $S(^1D)$, while that from SH is $S(^3P)$.

The fourth and fifth papers focus on the photoionization studies of SH and CH_3S. The experiments use pulsed field ionization (PFI)[10], which is a version of the zero-kinetic-energy (ZEKE)[11,12] photoelectron (PE) technique. The ZEKE/PFI detection scheme relies on delayed PFI of long-lived high-n-Rydberg states populated by laser excitation at a few wavenumbers below the ionization threshold. In the experiments, a one-color three-photon process is involved. That is, the SH [CH_3S] radical is first prepared from H_2S [CH_3SH] by the absorption of a signal photon. The subsequent ionization of SH [CH_3S] is accomplished by the nonresonant two-photon (N2P) excitation of SH [CH_3S] to the high-n-Rydberg state $SH^*(n)$ [$CH_3S^*(n)$] followed by PFI of $SH^*(n)$ [$CH_3S^*(n)$]. This is the first report on rotationally resolved PE spectrum of SH and vibrationally resolved PE spectrum of CH_3S[13-15].

PAPER 1.

A STUDY OF THE $S(^3P_{2,1,0}; {}^1D_2)$ PRODUCTION IN THE 193 nm PHOTODISSOCIATION OF $CH_3S(\tilde{X})$

ABSTRACT

The dynamics of $S(^3P_{2,1,0}; {}^1D_2)$ production from the 193nm photodissociation of CH_3SCH_3 has been studied using 2+1 REMPI techniques. The 193nm photodissociation cross section for the formation of S from CH_3S initially prepared in the photodissociation of CH_3SCH_3 is estimated to be $1x10^{-18}$ cm^2. The branching ratio for $S(^3P)/S(^1D)$ is found to be 0.15/0.85. The fine-structure distribution observed for product $S(^3P_{2,1,0})$ is nearly statistical. Possible potential energy surfaces involved in the 193nm photodissociation of $CH_3S(\tilde{X})$ have been examined theoretically along the CH_3-S dissociation coordinate in C_{3v} symmetry. These calculations suggest that predissociation of $CH_3S(\tilde{C}^2A_2)$ via the repulsive $CH_3S(\tilde{E}^2E)$ surface is most likely responsible for the efficient production of $S(^1D)$. For vibrationally excited $CH_3S(\tilde{X})$, a viable mechanism for the dominant production of $S(^1D)$ may involve direct dissociation via the $CH_3S(\tilde{E}^2E)$ state formed in the 193nm photoexcitation.

INTRODUCTION

Unlike unimolecular dissociation on the ground electronic potential energy surface, molecular dissociation in excited electronic states often involves predissociation due to nonadiabatic interactions with other electronic states. Translational energy distributions, internal state distributions, and final product branching ratios can be critically sensitive to the predissociating excited potential energy surfaces. In the past decade, tremendous progress has been made in understanding the photodissociation dynamics of triatomic molecules.[1-3] However, the photodissociation study of radicals, especially polyatomic radicals, has remained essentially an unexplored research area. Detailed state-to-state photodissociation cross sections for radicals in the ultraviolet (UV) and vacuum ultraviolet (VUV) provide challenges not only for dynamical calculations, but also for *ab initio* quantum chemical studies.

Recent photofragmentation studies on a series of organosulfur compounds[4-8] performed in our laboratory have yielded valuable information on the energetics and the photodissociation dynamics of these molecules. Based on the kinetic energy distributions observed for S,[5,6] the photodissociation studies of CH_3SSCH_3 and CH_3SCH_3 suggest that the CH_3S photofragment can further dissociate by the absorption of a second 193nm photon to produce S predominantly in the ^1D state. In order to examine this suggestion, we have measured directly the nascent electronic state distributions of $S(^3P_{2,1,0}; ^1D_2)$ atoms formed in the 193nm photodissociation of CH_3SCH_3 [processes (1) and (2)] using 2+1 resonance-enhanced multiphoton ionization (REMPI) detection schemes.[9,10]

$$CH_3SCH_3 + h\nu\ (193nm) \rightarrow CH_3S(\tilde{X}) + CH_3 \quad (1)$$

$$CH_3S(\tilde{X}) + h\nu\ (193nm) \rightarrow CH_3 + S(^3P_{2,1,0};\ ^1D_2) \quad (2)$$

The previous 193nm laser photofragmentation time-of-flight (TOF) studies[5,6] indicate that $S(^3P_J,^1D_2)$ atoms are produced from CH_3SCH_3 via processes (1) and (2).

Many kinetic[11-14] and spectroscopic[15-21] investigations have been made involving CH_3S radicals produced by excimer laser photodissociation of CH_3SCH_3 and CH_3SSCH_3. Also, the energetics and geometries of CH_3S in the ground and excited electronic states have been the subject of many *ab initio* calculations.[22-28]

The measurements of absolute UV and VUV photodissociation cross sections of organosulfur radicals are relevant to the modeling of atmospheric sulfur chemistry. To our knowledge, absolute UV and VUV photodissociation cross sections for organosulfur radicals have not been reported. By using 2+1 REMPI detection schemes to monitor the formation of $S(^3P_{2,1,0};\ ^1D_2)$, and by calibrating the S^+ intensities due to $S(^3P_{2,1,0};\ ^1D_2)$ from process (2) to those from process (3), we have obtained an estimate of the absolute photodissociation cross section for the formation of $S(^3P_{2,1,0};\ ^1D_2)$ from the 193nm photodissociation of $CH_3S(\tilde{X})$.

$$CS_2 + h\nu\ (193nm) \rightarrow CS(v) + S(^3P_{2,1,0};\ ^1D_2) \quad (3)$$

The absolute cross sections for process (3) are known.[29] The branching ratio for $S(^3P)/S(^1D)$ (=2.78) and the fine-structure distribution of $S(^3P_{2,1,0})$ resulting from the

193nm photodissociation of CS_2 have also been measured previously by the VUV laser-induced fluorescence[30] and time-of-flight (TOF) mass spectrometric[31] methods.

In order to rationalize the experimental observations, we have examined the *ab initio* multi-configuration-self-consistence-field (MCSCF) potential energy surfaces of CH_3S along the CH_3-S dissociation coordinate. In addition, the geometrical parameters for the $CH_3S(\tilde{X},\tilde{A})$ have been optimized by MCSCF calculations.

EXPERIMENTAL

The experiment basically involves the delayed 2+1 REMPI detection of $S(^3P_{2,1,0};^1D_2)$ produced by processes (1) and (2). The schematic diagram of the experimental setup is shown in Fig. 1. A home-built TOF mass spectrometer of the two-stage Wiley-McLaren design[32] is used to detect S^+ ions [see Fig. 2]. A pulsed beam of neat CH_3SCH_3 is produced by supersonic expansion through a commercial pulsed valve (General Valve No. 9, nozzle diameter = 0.5 mm, temperature $\approx$ 298 K, stagnation pressure $\leq$ 150 Torr). The molecular beam is skimmed (7 cm from the nozzle) by a conical skimmer (1 mm dia.) and intersects with both the dissociation and ionization lasers 8.3 cm downstream from the skimmer. The molecular beam source chamber is pumped by a liquid-nitrogen trapped 6 in. diffusion pump (pumping speed $\approx$ 2,000 ℓ/s), while the photodissociation and detection chamber is evacuated by a 50 ℓ/s turbomolecular pump. For a pulsed valve repetition rate of 17 Hz, the beam source and photodissociation chambers are maintained at pressures of $\approx 1\times10^{-4}$ and 2×10^{-6} Torr, respectively. The ArF photodissociation laser (Questek 2460) is operated in the constant pulse energy mode. The laser beam is attenuated by layers of stainless steel wire mesh and is spatially filtered by two irises before being focused by a (200 mm f.l.) fused-silica lens to a spot of $\approx$ 2x2 mm^2 in the intersection region. The laser energies used are in the range of 160 to 1000 μJ/pulse.

The ionization of $S(^3P_{2,1,0};\ ^1D_2)$ is accomplished with an excimer laser (Lambda Physik EMG 201 MSC) pumped dye laser (FL 3002) system. Rhodamine 6G and Kiton

Figure 1. Schematic diagram of the experimental setup.

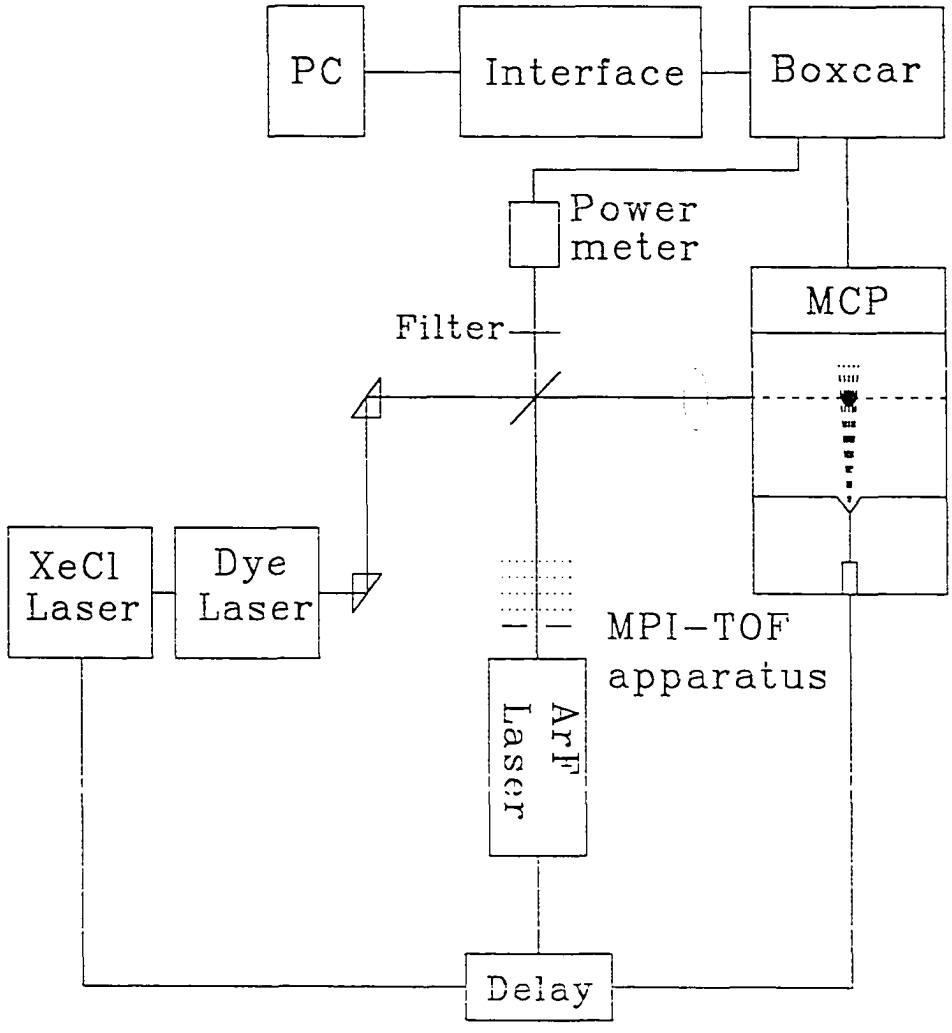
PC
Interface
Boxcar
Power meter
MCP
Filter
XeCl Laser
Dye Laser
MPI-TOF apparatus
ArF Laser
Delay

Figure 2. Cross section view of the TOF mass spectrometer. (1)photodissociation photoionization chamber; (2) photodissociation and photoionization region; (3) beam source chamber; (4) pulsed valve; (5) skimmer; (6) TOF tube; and (7) microchannel plate detector.

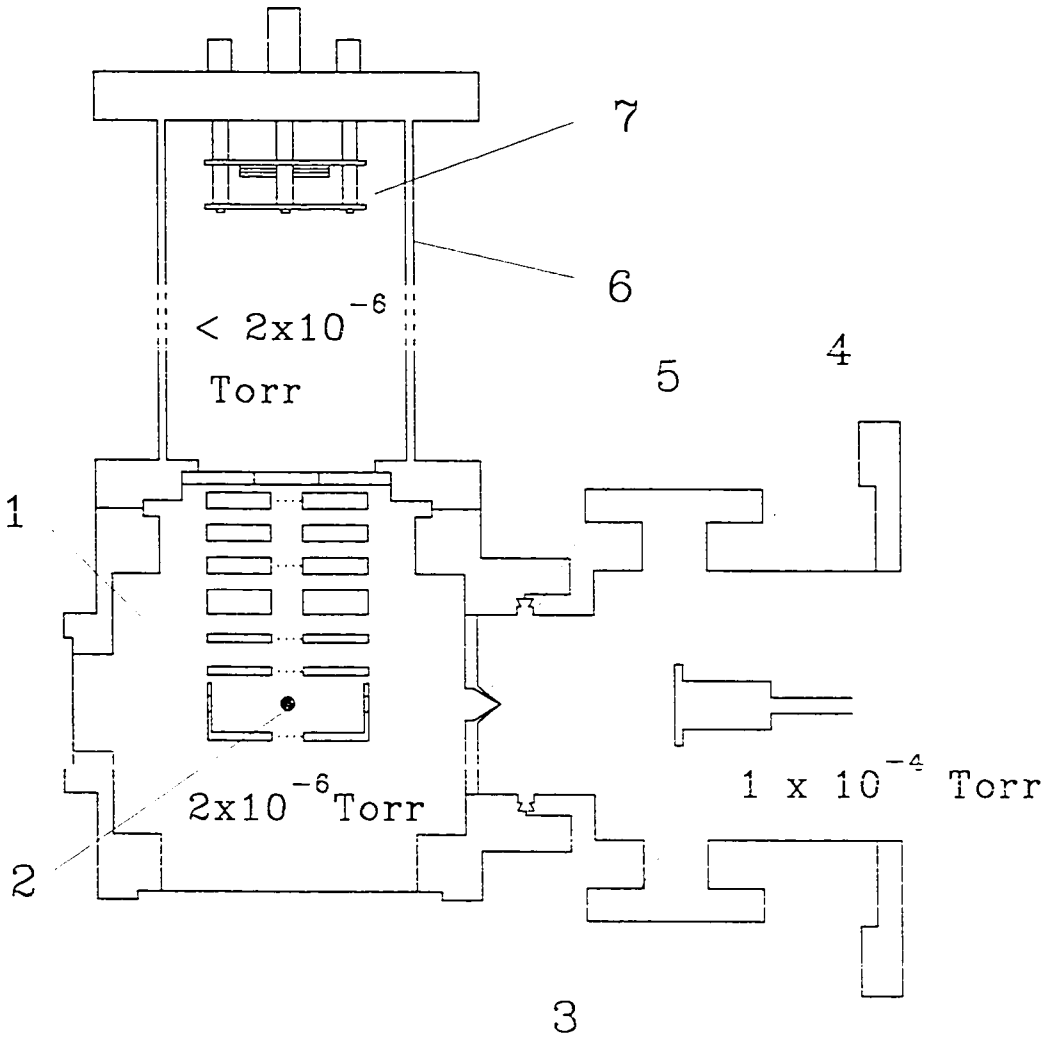
7
6
< 2x10^-6
Torr
5
4
1
2
2x10^-6Torr
1 x 10^-4 Torr
3

Red are used to produce the fundamental in the 570-630 nm region. The UV second harmonic is generated using a temperature stabilized angle-tuned BBO crystal (FL-37-1). The pulse energy, typically 200μJ/pulse, is monitored with a pyroelectric detector (Molectron J3-05). The dye laser beam propagates coaxially with the ArF laser beam into the reaction chamber and intersects with the molecular beam at 90°.

The firing of the dissociation excimer laser is delayed by 570 μs with respect to the triggering pulse for opening the pulsed valve. We find that the S^+ intensity remains nearly constant when the delay between the photodissociation and ionization lasers is varied in the range of 30-100 ns. Therefore, a delay of 50 ns between the two lasers is set for all the experiments. The firing sequence of the pulsed valve and the two lasers is controlled by two digital delay units (Stanford Research, Model DG 535). The ion signal from the microchannel plate (MCP) and the excimer laser signal from the pyroelectric detector are fed into two identical boxcar integrators (Stanford Research, SR-250), which are interfaced to an IBM AT computer.

The liquid CS_2 and CH_3SCH_3 samples (99% purity) were obtained from Aldrich. The liquid CH_3SCH_3 sample was degassed by a series of freeze-and-thaw-cycles before use in the experiment.

A. Detection of $S(^3P_{2,1,0})$ and $S(^1D_2)$

Probing of the $S(3^3P_J)$ and $S(3^1D_2)$ atomic states is accomplished by 2-photon absorption, $S(3^3P_J) \rightarrow S(4^3P_J)$ and $S(3^1D_2) \rightarrow S(4^1F_3)$, followed by absorption of a third photon to produce S^+ in the $^4S^\circ$ and $^2D^\circ$ states, respectively (Fig. 3). These schemes have been used previously for the detection of $S(^3P_{2,1,0}; {}^1D_2)$ formed in the photodissociation of

Figure 3. 2+1 REMPI detection schemes for $S(^3P_{2,1,0})$ and $S(^1D_2)$.

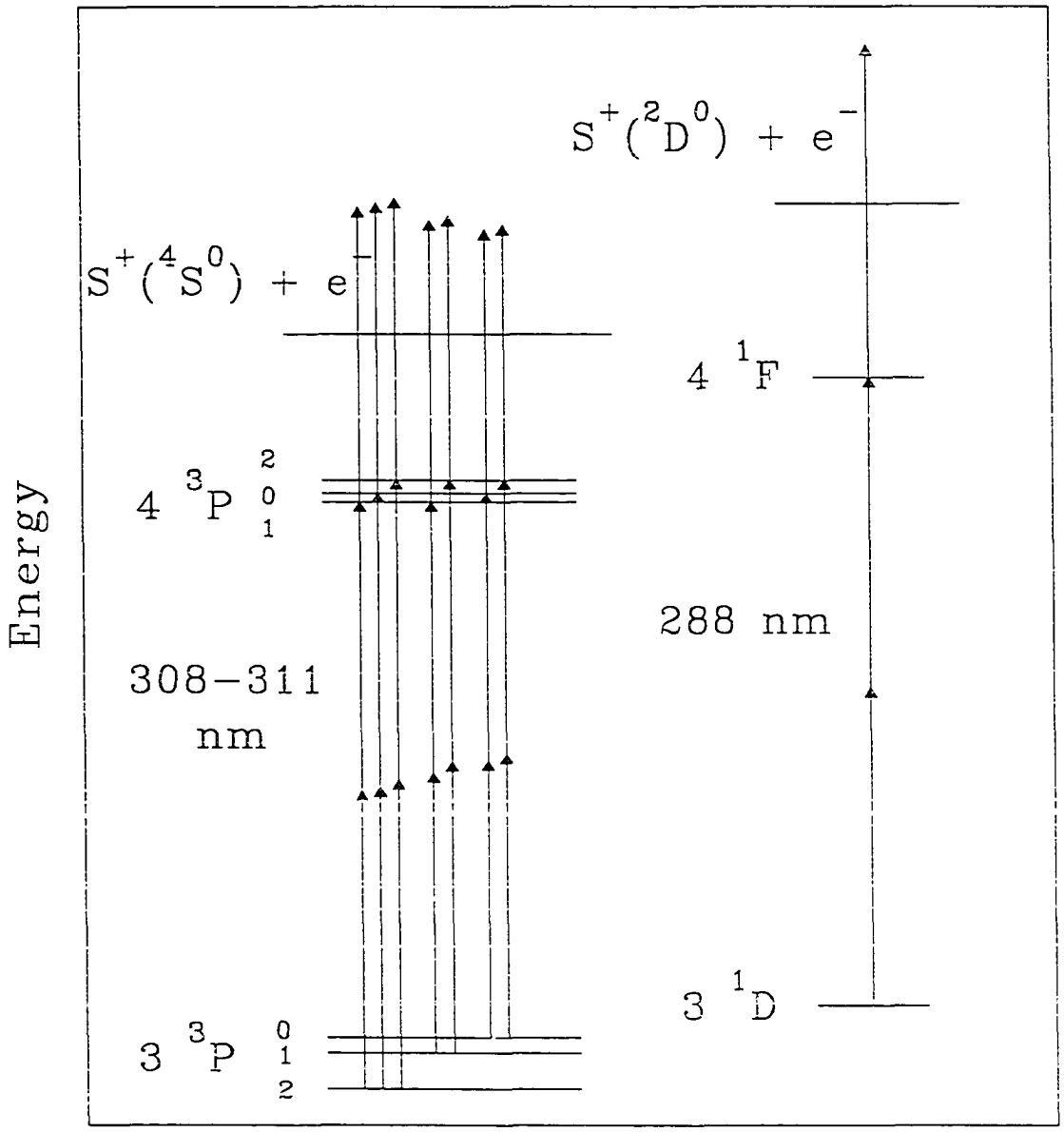
Energy
$S^+(^2D^0) + e^-$
$S^+(^4S^0) + e^-$
$4\ ^1F$
$4\ ^3P\ ^{2\ 0\ 1}$
288 nm
308–311 nm
$3\ ^1D$
$3\ ^3P\ ^{0\ 1\ 2}$

sulfur-containing molecules.[10,11] The ionization peaks corresponding to the detection of $S(^3P_{2,1,0})$ and $S(^1D_2)$ appear in the wavelength region of 308-311 nm and at 288.19 nm, respectively.

Ideally, the S^+ signal formed in the 2+1 REMPI of $S(^3P_2; ^1D_2)$ should have an E^n dependence with n=3, where E is the ionization dye laser power. For $S(^3P_2)$ and $S(^1D_2)$ formed by the 193nm photodissociation of CS_2 in a dissociation excimer laser power range of 0.18-1.2 mJ, we observe that n = 2.3-2.4 in an E range of 0.01-0.40 mJ. This compares with n = 2.7-3.0 observed for the S^+ signal produced from CH_3SCH_3 in an E range of 0.03-0.40 mJ and a dissociation excimer laser power range of 0.54-5.7 mJ. The higher power dependence observed for S^+ from CH_3SCH_3 is interpreted that S atoms are also produced from the dissociation of CH_3S by the dye laser. The ionization of these S atoms by the dye laser contributes to the observed S^+ signal from processes (1) and (2). Using the observed ionization laser power dependence of S^+ from CS_2 as a normalization factor, we have subtracted the background S^+ signal attributed to dye laser photodissociation of CH_3S.

The fine-structure distribution of $S(3^3P_{2,1,0})$ is measured by summation over the peak intensities corresponding to transitions to the upper $S(4^3P_{2,1,0})$ fine-structure levels.[33] Figure 4 shows a typical spectrum for the ionization of $S(3^3P_{2,1,0})$ formed by process (3). The fine-structure distribution has been determined to be $^3P_2 : ^3P_1 : ^3P_0 = 0.71\pm0.02 : 0.20\pm0.02 : 0.09\pm0.04$, in excellent agreement with the result obtained by Waller and Hepburn[30] using the VUV laser-induced fluorescence technique.

Figure 4. Typical 2+1 REMPI spectrum for $S(^3P_{2,1,0})$ formed in the 193nm photodissociation of CS_2.

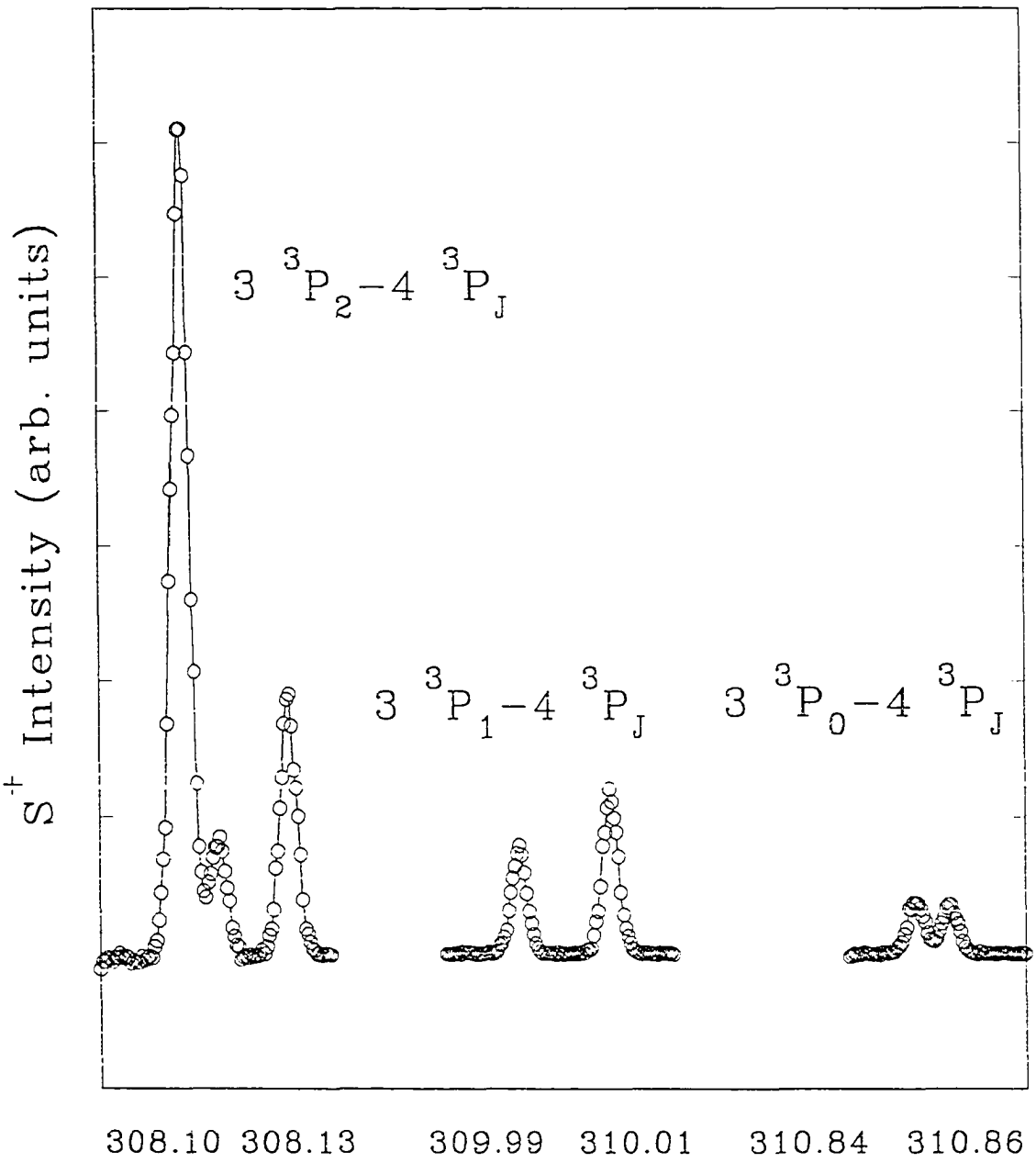
S^+ Intensity (arb. units)
3 $^3P_2$–4 ^3P_J
3 $^3P_1$–4 ^3P_J
3 $^3P_0$–4 ^3P_J
308.10
308.13
309.99
310.01
310.84
310.86

B. $S(^3P)/S(^1D)$ branching ratio and absolute cross section for process (2)

The rate equations applicable to processes (1) and (2) are:

$$d[CH_3SCH_3]/dt = -I\sigma_1[CH_3SCH_3], \quad (4)$$

$$d[CH_3S]/dt = I\sigma_1[CH_3SCH_3] - I\sigma_2[CH_3S], \quad (5)$$

$$d[S]/dt = I\sigma_2[CH_3S]. \quad (6)$$

Here, I is the ArF laser photon intensity [# of photons/(cm^2·sec)] and σ_1 and σ_2 represent the absolute cross sections for processes (1) and (2), respectively. The number densities for CH_3SCH_3 ($[CH_3SCH_3]$), CH_3S ($[CH_3S]$), and S ([S]) due to one laser pulse are related to σ_1, σ_2, the laser flux (F), and the initial number density of CH_3SCH_3 ($[CH_3SCH_3]_o$) by the relations:

$$[CH_3SCH_3] = [CH_3SCH_3]_o\exp(-\sigma_1 F), \quad (7)$$

$$[CH_3S] = [CH_3SCH_3]_o[\sigma_1/(\sigma_2-\sigma_1)][\exp(-\sigma_1 F) - \exp(-\sigma_2 F)], \quad (8)$$

$$[S] = [CH_3SCH_3]_o[\sigma_1\sigma_2/(\sigma_2-\sigma_1)][-(1/\sigma_1)\exp(-\sigma_1 F) + (1/\sigma_2)\exp(-\sigma_2 F) + 1/\sigma_1 - 1/\sigma_2]. \quad (9)$$

The laser flux F (# of photons/cm^2) is the intensity integrated over the laser pulse width. The S^+ signal resulting from the 2+1 REMPI is directly proportional to the number density of S. Since σ_1 is known to be $1x10^{-17}$ cm^2,[34] the $S(^3P)/S(^1D)$ branching ratio and the value for σ_2 can be determined by calibrating the S^+ signals due to the formation of $S(^3P_{2,1,0}; {}^1D_2)$ from CH_3SCH_3 to those from CS_2.

In principle, the best method for calibrating the S^+ signal of $S(^3P_{2,1,0}; {}^1D_2)$ from the photodissociation of CH_3SCH_3 to that from process (3) is to measure the S^+ signal due to CS_2 formed in the pulsed beam using the same expansion conditions as that used for the production of the CH_3SCH_3 beam. However, the S^+ signal from CS_2 observed in such an experiment saturates the microchannel plate detector. The S^+ signal from CS_2 is much higher than that from CH_3SCH_3 because process (3) is proportional to the dissociation excimer laser power, whereas the formation of S from processes (1) and (2) is proportional to the second power of the dissociation excimer laser power. For this reason, a slight contamination of the nozzle by CS_2 can affect significantly the measurement of the relative signals for $S(^3P_{2,1,0})$ and $S(^1D_2)$. We find that the most reliable measurement of the S^+ signal from CS_2 is obtained in a calibration experiment under gas cell conditions. This is achieved by leaking CS_2 through a leak valve into the photodissociation (and photoionization) chamber to a pressure of $2x10^{-6}$ Torr. The CS_2 calibration experiment can be performed immediately after the measurement of the S^+ from CH_3SCH_3 with all the other experimental conditions unchanged.

The number density of CH_3SCH_3 in the photodissociation region is needed to estimate the absolute cross section for process (2). The number density of CH_3SCH_3 at the photodissociation region is calculated by using a standard molecular beam flow formula[35] based on the known nozzle diameter and distance between the nozzle and the photodissociation region. The temporal profile for the pulsed beam is sufficiently broad that its intensity is essentially flat in the central portion used in this experiment.

In the estimation of the dissociation excimer laser flux, we assume that the mildly

focused laser beam has a Gaussian beam profile.[36] The photodissociation laser spot size has also been checked by examining the burn spots on thermal papers at various distances from the focusing lens. The variation of the laser beam spot size with distance from the focusing lens is consistent with that predicted by the Gaussian beam profile. In the photodissociation region the ionization laser beam spot is smaller than the photodissociation laser beam spot.

The volumes of product S atoms sampled by the ionization detector in the pulsed beam mode and in the gas cell mode are different. The determination of the intersection volume of the ionization laser beam and the CH_3SCH_3 beam, as well as that of the ionization laser beam and the CS_2 molecules in the gas cell, is necessary for the calibration. Here, the ionization dye laser beam profile is again assumed to conform with the Gaussian profile. The size of the CH_3SCH_3 beam is determined by the skimmer opening and the nozzle-skimmer distance.

AB INITIO CALCULATION

All calculations on the electronic structures of CH_3S are performed using of the GAMESS program.[37] The calculations are based on the MCSCF and the first order configuration interaction (FOCI) methods. The standard 6-31G** basis set is used. In order to properly describe the excited states of CH_3S, we have extended the basis set to include the Rydberg functions with $\alpha_{4s} = 0.023$, $\alpha_{4p} = 0.020$ and $\alpha_{3d} = 0.015$ for the sulfur atom and $\alpha_{3s} = \alpha_{3p} = 0.040$ for the carbon atom.

The electronic configuration for the $CH_3S(\tilde{X}^2E)$ ground state in C_{3v} symmetry is

$$1a_1^2 2a_1^2 3a_1^2 4a_1^2 1e^4 5a_1^2 2e^4 6a_1^2 7a_1^2 3e^3 8a_1^0 \ldots$$

The $1a_1$, $2a_1$, $3a_1$, $4a_1$, and 1e orbitals are the core orbitals corresponding to the 1s, 2s, and 2p orbitals of the sulfur atom and the 1s orbital of the carbon atom. The $5a_1$ and 2e orbitals are C-H bonding orbitals associated with the methyl group. The $6a_1$ and 3e orbitals correspond essentially to the 3s and ($3p_x$,$3p_y$) orbitals of sulfur, respectively. The $7a_1$ orbital is the C-S bonding orbital, while the $8a_1$ orbital is the C-S anti-bonding orbital. In the calculation of the potential energy curves along the CH_3-S dissociation coordinate, we restrict CH_3S to C_{3v} symmetry and we freeze the core and the $5a_1$ and 2e C-H bonding orbitals. The active space includes the $6a_1$, $7a_1$, $8a_1$, and 3e orbitals and the number of active electrons is seven. In the calculation of the excited states, we use the state-averaged MCSCF with equal weights for the three lowest states. The FOCI calculations are carried

out using the molecular orbitals obtained in the MCSCF calculations. The potential energy curves for CH_3S thus calculated are depicted in Fig. 5. The figure only includes the doublet excited states, which may be populated by spin-allowed transitions from the ground $CH_3S(\tilde{X}^2E)$ state.

The $CH_3S(\tilde{X}^2E)$ state is subjected to the Jahn-Teller distortion, and the actual structure for $CH_3S(\tilde{X})$ is expected to have a C_s symmetry. The previous studies, however, indicate that the Jahn-Teller stabilization is small[22] and is substantially smaller than the spin-orbit splitting (259 cm^{-1})[20] for $CH_3S(\tilde{X}^2E_{3/2,1/2})$. In a lower C_s symmetry, a_1 transforms as a′ and the e-orbitals are split into orbitals transformed as a′ and a″. The $CH_3S(\tilde{X}^2A')$ ground state has the electronic configuration,

$$1a'^2 2a'^2 3a'^2 4a' 5a'^2 1a''^2 6a'^2 7a'^2 2a''^2 8a'^2 9a'^2 3a''^2 10a'^1 11a'^0 \ldots$$

We have also optimized the ground $CH_3S(\tilde{X}^2A', {}^2A'')$ state and the first excited $CH_3S(\tilde{A}^2A_2)$ state using the MCSCF method.

Figure 5. *Ab Initio* potential energy curves for CH_3S in C_{3v} symmetry plotted as a function of the CH_3-S distance (see text).

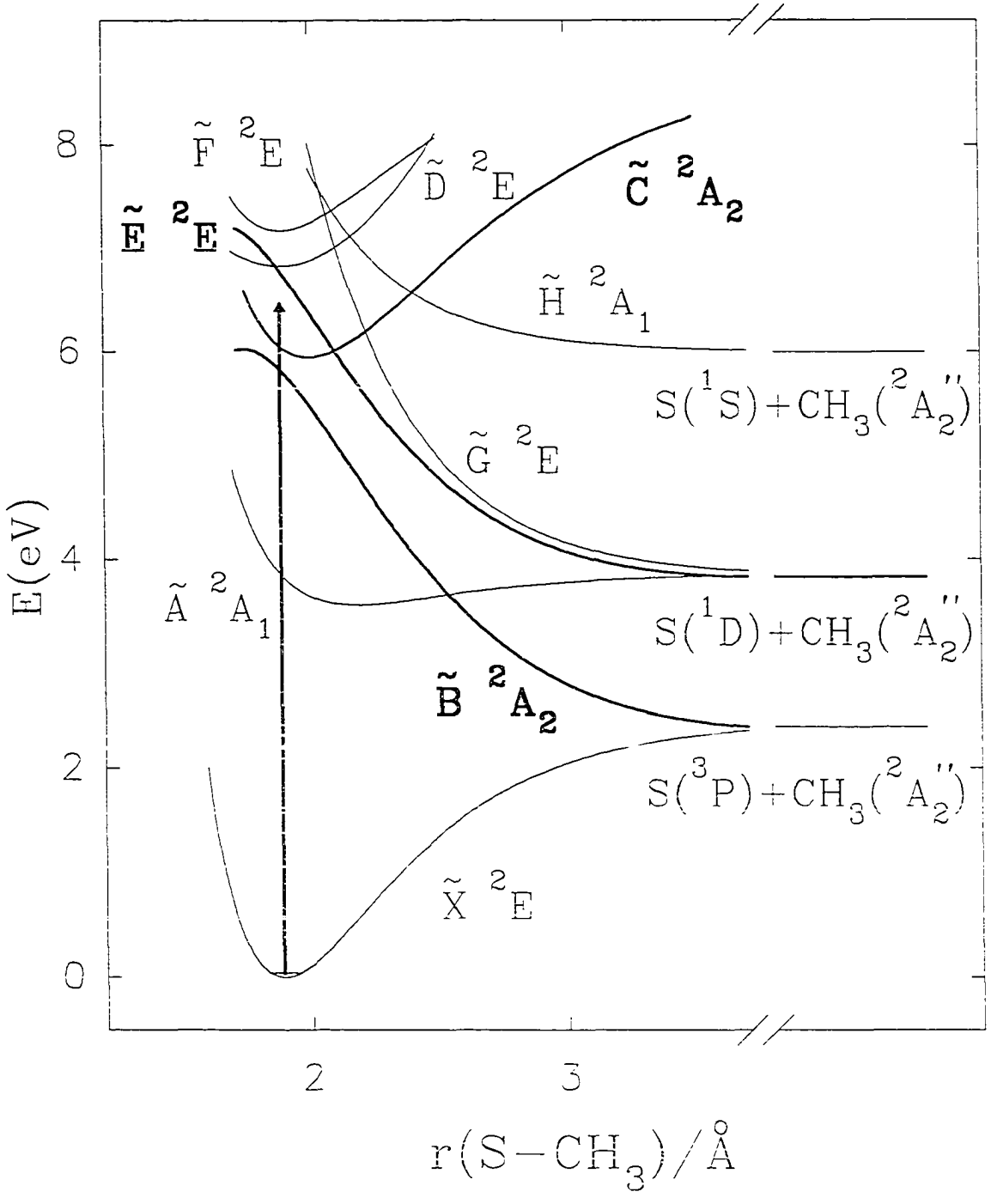
8
6
4
2
0
E(eV)
2
3
r(S−CH3)/Å
F̃ 2E
D̃ 2E
C̃ 2A2
Ẽ 2E
H̃ 2A1
S(1S)+CH3(2A2'')
G̃ 2E
Ã 2A1
S(1D)+CH3(2A2'')
B̃ 2A2
S(3P)+CH3(2A2'')
X̃ 2E

RESULTS AND DISCUSSION

A. Comparison of theoretical and experimental geometrical parameters for $CH_3S(\tilde{X},\tilde{A})$

Using the standard Gaussian program, the geometry of $CH_3S(\tilde{X})$ was examined by Janousek and Brauman in a restricted C_{3v} symmetry at the STO-3G and 4-31G levels.[22] Most recently, the structure of CH_3S in the ground $\tilde{X}^2A'$ state has been optimized using the density function (DF) method[27] and using the Gaussian program at the HF/6-31G*,[26] MP2/6-31G*,[23] and the MP2/6-31G** [28] levels. All these higher level *ab initio* calculations predict that CH_3S in the ground state has a C_s symmetry with the distance of one of the C-H bonds [r(C-H(1))] slightly longer than those for the other two C-H bonds [r(C-H(2))=r(C-H(3))]. In Table I, the geometrical parameters for $CH_3S(\tilde{X}^2A')$ predicted by the previous calculations are compared to those obtained here. The θ values shown in the table are the bond angles. The MCSCF parameters of this work are in fair agreement with those obtained from the MP2/6-31G* and MP2/6-31G** calculations.

Despite many previous experimental studies, detailed structural information for CH_3S is still lacking. In a recent high resolution laser-induced fluorescence study of jet cooled CH_3S, Hsu et al.[17] have analyzed the rotationally resolved spectra obtained in their experiment by considering a C_{3v} symmetry for CH_3S. By assuming a distance of 1.10 Å for r(C-H(1)) [=r(C-H(2))=r(C-H(3))], they have obtained estimates of 1.767 Å and 115.8° for r(C-S) and θ(S-C-H(1)) [=θ(S-C-H(2))=θ(S-C-H(3))], respectively. The θ(S-C-H) value thus deduced from the experiment is greater than the theoretical predictions[23,26-

Table I. Optimized geometrical parameters for CH_3S in the X^2A', $^2A''$, A^2A') states.

Methods	r(C-S) (Å)	r(C-H(1)) (Å)	r(C-H(2)) (Å)	θ(S-C-H(1)) (degree)	θ(S-CH(2)) (degree)
$CH_3S(\tilde{X}^2A')$					
UHF/4-31G[a]	1.76	1.10	1.10	110.9	110.9
MP2/6-31G* [b]	1.799	1.095	1.090	107.0	111.7
MP2/6-31G** [c]	1.797	1.090	1.085	106.9	111.7
DF[d]	1.762	1.116	1.107	106.0	113.0
MCSCF[e]	1.808	1.084	1.081	107.0	110.5
Expt[f]	1.767	1.10	1.10	115.8	115.8
$CH_3S(^2A'')$					
MCSCF[e]	1.808	1.080	1.083	111.3	108.3
$CH_3S(\tilde{A}^2A')$					
MCSCF[e]	2.191	1.073	1.073	99.1	99.3
Expt[f]	2.057	1.100	1.100	111.7	111.7

a) Reference 22.
b) Reference 23.
c) Reference 28.
d) Reference 27.
e) This work.
f) Reference 17. In the derivation of r(C-S) from experimental data, CH_3S is assumed to have a C_{3v} symmetry and r(C-H(1)) [=r(C-H(2))=r(C-H(3))] is assumed to have a value of 1.10 Å.

[28] by $\approx 6°$. The geometrical parameters for the first excited $CH_3S(\tilde{A}^2A_1)$ state have also been derived using similar procedures. These values are also included in Table I.

As a result of Jahn-Teller distortion, the $CH_3S(C_{3v}; \tilde{X}^2E)$ state is split into the $^2A'$ and $^2A''$ states. The geometrical parameters predicted by the MCSCF calculation for the $^2A''$ state are also listed in Table I. We find that the $^2A''$ state is higher than the $^2A'$ state by only 9 cm^{-1}. Therefore, these two states essentially remain degenerate. The Jahn-Teller barrier between these states is <50 cm^{-1}. These theoretical results are consistent with previous calculations.[22,25]

The geometrical parameters predicted by the MCSCF calculation for the first excited $CH_3S(\tilde{A})$ correspond to a structure deviating only slightly from a C_{3v} symmetry. Because of this, we have labelled the first excited state for CH_3S as $\tilde{A}^2A_1$. Since the $\tilde{A}^2A_1$ state corresponds to the excitation of an electron from the C-S bonding $7a_1$ orbital to the non-bonding 3e orbital, the C-S bond in $CH_3S(\tilde{A}^2A_1)$ is expected to be substantially weaker than that in $CH_3S(\tilde{X})$. The geometrical parameters for $CH_3S(\tilde{A}^2A_1)$ obtained in the experiment of Hsu et al.[17] and in the MCSCF calculation are in qualitative agreement. The experimental and theoretical values for r(C-S) in $CH_3S(\tilde{A}^2A_1)$ are >2 Å, significantly longer than r(C-S) in the ground state. As a result of this, the structure of the methyl group in this state comes close to that of the methyl radical. This is manifested by the observation that the bond angle θ(S-C-H) in $CH_3S(\tilde{A}^2A_1)$ is smaller than that in $CH_3S(\tilde{X})$. We note that the theoretical value for r(C-S) is greater than the experimental estimate by ≈ 0.13 Å, while the theoretical bond angle θ(S-C-H) is smaller than deduced from the experiment by more than 11°.

Based on the MCSCF total energies of the optimized $CH_3S(\tilde{X},\tilde{A})$ states, the energy difference between the potential wells of the $CH_3S(\tilde{X})$ and $CH_3S(\tilde{A})$ states is 3.34 eV, a value in good agreement with the transition energy of 3.29 eV for $\tilde{X}^2E_{3/2} \rightarrow \tilde{A}^2A_1$ obtained in a recent laser-induced fluorescence experiment.[20] The MCSCF calculation predicts that the well depth for $CH_3S(\tilde{A})$ with respect to $CH_3(\tilde{X}^2A_2'') + S(^1D)$ is 0.31 eV.

B. Potential energy curves for CH_3S calculated along the CH_3-S dissociation coordinate

The vertical arrow in Fig. 5 corresponds to the excitation energy of 6.41 eV in the absorption of a 193nm photon by $CH_3S(\tilde{X}^2E)$ in its ground vibrational state. Table II summarizes some properties of selected excited states for CH_3S ($\tilde{A}^2A_1$, $\tilde{B}^2A_2$, $\tilde{C}^2A_2$, $\tilde{D}^2E$, $\tilde{E}^2E$, $\tilde{F}^2E$), which may be involved in the 193nm photodissociation of $CH_3S(\tilde{X})$. Considering the internal excitation of CH_3S initially formed by process (1),[6] the excitation to the $\tilde{F}^2E$ state, which has a vertical transition energy (T_e) of 7.16 eV, is possible. Note that the potential energy curves plotted as a function of r(C-S) in Fig. 5 are calculated assuming a C_{3v} symmetry for CH_3S. It is expected that the T_e values corresponding to optimized CH_3S structures may be slightly different from those given in the table. The $\tilde{C}$ and $\tilde{D}$ states are Rydberg in nature and the $\tilde{B}$ and $\tilde{E}$ states are repulsive. Mouflih et al.[25] report the energies for CH_3S in the excited $\tilde{A}$, $\tilde{B}$, and $\tilde{D}$ states to be 4.02, 5.70, and 6.45 eV, respectively, relative to the ground CH_3S state. Their SCF molecular orbital calculations used a moderately large basis set, and configuration interaction calculations were included for all the electronic states. Their predictions are in reasonable accord with the corresponding T_e values obtained here. The $\tilde{G}$ (repulsive) and $\tilde{H}$ (repulsive) states,

Table II. Predicted spectroscopic properties for selected excited states which may be involved in the 193nm photodissociation of CH_3S.

Excited state CH_3S (C_{3v})	Vertical transition energy (eV) (From $\tilde{X}^2E$ state)	Oscillator strength (From $\tilde{X}^2E$ state)	Adiabatic product $S(^3P,^1D)$ states
$\tilde{A}^2A_1$	3.72	0.0035	$S(^1D)$
$\tilde{B}^2A_2$	5.82	0.0073	$S(^3P)$
$\tilde{C}^2A_2$	6.17	0.0408	...
$\tilde{D}^2E$	6.81	0.0014	...
$\tilde{E}^2E$	6.86	0.0006	$S(^1D)$
$\tilde{F}^2E$	7.12	...	...

which have theoretical T_e values greater than 8.0 eV, may not be directly populated in the 193nm excitation of $CH_3S(\tilde{X})$.

The radiative lifetimes measured for the ν_3 = 0, 1, and 2 vibrational states of $CH_3S(\tilde{A}^2A_1)$ indicate that the ν_3 = 1 and 2 states of $CH_3S(\tilde{A}^2A_1)$ are predissociative.[17-19] This observation is consistent with the crossing of the $\tilde{A}^2A_1$ and $\tilde{B}^2A_2$ states as shown in Fig. 5. The crossing occurs at 746 cm^{-1} above the potential well of the $CH_3S(\tilde{A}^2A_1)$ state. Since the ν_3 spacing for the $CH_3S(\tilde{A}^2A_1)$ state is measured to be 401±2 cm^{-1}, we expect that ν_3 = 0 is stable, whereas ν_3 > 0 states are predissociative, a prediction consistent with the experimental observation. Predissociation of $CH_3S(\tilde{A}^2A_1)$ via $CH_3S(\tilde{B}^2A_2)$, due to nonadiabatic interactions, should lead to the formation of $CH_3(\tilde{X}^2A_2'') + S(^3P)$.

C. Fine-structure distribution of $S(^3P_{2,1,0})$ and $S(^3P)/S(^1D)$ branching ratio

The fine-structure distribution of $S(^3P_J)$ produced in the 193nm photodissociation of CH_3S [process (2)] is determined to be $^3P_2 : {}^3P_1 : {}^3P_0$ = 0.59±0.02 : 0.32±0.02 : 0.09±0.04, which is close to the statistical distribution of 5/9 : 3/9 : 1/9.

The S^+ intensities observed in the 2+1 REMPI of $S(^3P_2)$ and $S(^1D_2)$ are plotted as a function of the 193nm photodissociation laser photon flux in Figs. 6(a) and 6(b), respectively. The similarity of the photon flux dependencies for S^+ due to $S(^3P_2)$ and $S(^1D_2)$ is consistent with the conclusion that both $S(^3P_2)$ and $S(^1D_2)$ originate from CH_3S formed in process (1). Based on the fine-structure distribution and the overall $S(^3P)/S(^1D)$ ratio known for process (3),[30,31] the $S(^3P)/S(^1D)$ ratio for process (2) is determined to be 0.15/0.85. According to six independent measurements, the fraction of $S(^1D_2)$ formed in the 193nm photodissociation of CH_3S is found to be 0.85±0.05. This finding is in accord

Figure 6. Photodissociation laser flux (# photons/cm^2) dependence of S^+ signal due to the ionization of (a) $S(^3P_2)$ and (b) $S(^1D_2)$ formed by processes (1) and (2). (o) experimental data; (•) best fit using Eq. (9).

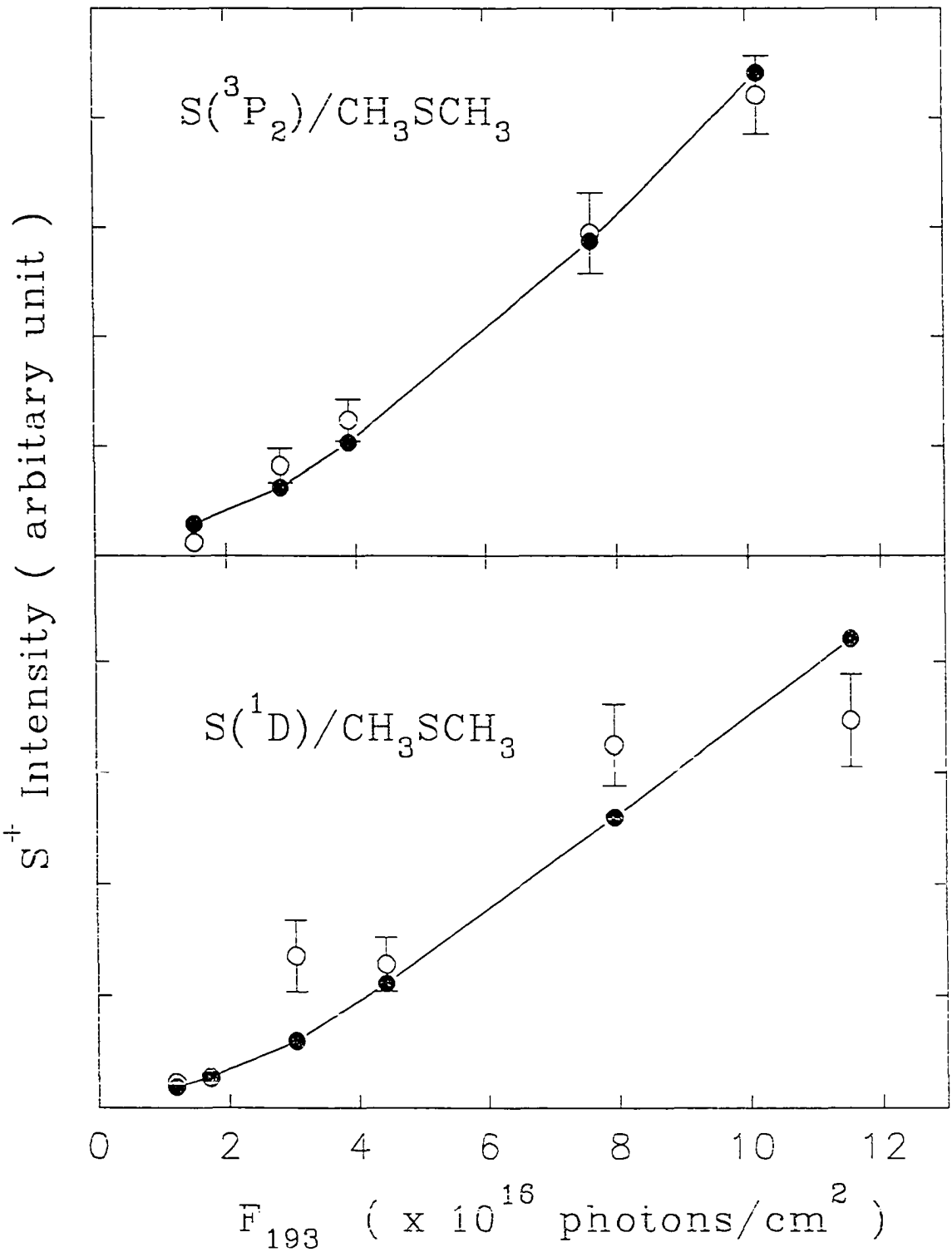
S(3P2)/CH3SCH3
S(1D)/CH3SCH3
S+ Intensity (arbitary unit)
0
2
4
6
8
10
12
F193 (x 10^16 photons/cm^2)

with the suggestion of the TOF experiment that S atoms formed in process (2) are predominantly in the ^1D state.[5,6]

The theoretical photodissociation study of Freed and co-workers[38] shows that photodissociation may proceed in two limiting cases, depending on the relative kinetic energy of the dissociation process. At low recoil energy, the fine-structure distribution is governed by the adiabatic potential surfaces. In this limit, symmetry correlation determines the fine-structure distribution. At the high energy limit a frame transformation would result in a statistical fine-structure distribution. The potential curves shown in Fig. 5 suggest that the formation of $S(^3P_J)$ proceeds most likely via the repulsive $CH_3S(\tilde{B}^2A_2)$ state and that the dissociation is a case of the high energy regime.

As shown in Table II, the transition $CH_3S(\tilde{X}^2E) \rightarrow CH_3S(\tilde{C}^2A_2)$ has by far the highest oscillator strength. This, together with the good match of the T_e value and the photon energy, the absorption of a 193nm photon by $CH_3S(\tilde{X}^2E)$ is expected to produce $CH_3S(\tilde{C}^2A_2)$. We note that $CH_3S(\tilde{C}^2A_2)$ is crossed by the repulsive $CH_3S(\tilde{E}^2E)$ state and that an avoided crossing exists between the $\tilde{B}$ and $\tilde{C}$ states. Due to nonadiabatic couplings, $CH_3S(\tilde{C}^2A_2)$ may predissociate via the $CH_3S(\tilde{E}^2E)$ state and lead to product $S(^1D_2)$ + $CH_3(\tilde{X}^2A'')$, while predissociation via the $CH_3S(\tilde{B}^2A_2)$ state yields $S(^3P_J)$ + $CH_3(\tilde{X}^2A'')$. The dominant formation of $S(^1D_2)$ by process (2) may be attributed to more favorable couplings of the $CH_3S(\tilde{E})$ and $CH_3S(\tilde{C})$ states. The previous 193nm laser photofragmentation TOF experiment indicates that the $CH_3S(\tilde{X})$ + CH_3 produced by process (1) may be excited internally by 1.3 eV. Assuming that the internal energies are partitioned according to the internal degrees of freedom of the photofragments, CH_3S may

be internally excited by ≈ 0.7 Ev, and the direct 193nm excitation to $CH_3S(\tilde{E})$ from $CH_3S(\tilde{X})$ formed in process (1) is possible. The direct formation of $CH_3S(\tilde{E})$ should favor the $S(^1D_2)$ + $CH_3(\tilde{X}^2A'')$ dissociation channel, a conclusion in accord with the experimental observation. We note that the inclusion of the interactions with potential curves of other multiplicities adds to the complexity of the photodissociation mechanism of this system.

We have also searched for the production of $S(^1S)$ from the 193nm photolysis of CH_3SCH_3. Within the sensitivity of our experiment, S^+ resulting from REMPI of $S(^1S)$ was not observed.

D. Absolute cross section for process (2)

Following the procedures described in the experimental section, we have obtained an estimate of $1x10^{-18}$ cm^2 for σ_2. The open circles shown in Figs. 6(a) and 6(b) are the experimental S^+ intensities from CH_3SCH_3 measured at specific ionization laser flux and the solid dots represent the best fits obtained using Eq. (9) and the cross sections for the formation of $S(^3P_2)$ and $S(^1D_2)$ by process (2). Due to the uncertainties involved in the calibration of the S^+ signals from CS_2 and CH_3SCH_3 as described above, we consider that the absolute value for σ_2 is a rough estimate. Furthermore, the absolute photodissociation cross section determined here for $CH_3S(\tilde{X})$ is characteristic of the $CH_3S(\tilde{X})$ radicals prepared by process (1), which contains significant internal excitations. The photodissociation cross section for $CH_3S(\tilde{X})$ may depend on its internal excitations. Nevertheless, we find that the $S(^3P)/S(^1D)$ branching ratios and absolute cross sections observed in the 193nm photodissociation of $CH_3S(\tilde{X})$ prepared by the photolysis of

CH_3SSCH_3 and CH_3SH[39] are consistent with those determined in this experiment. It will be interesting to examine the $S(^3P)/S(^1D)$ branching ratio due to the photodissociation of supersonically cooled CH_3S.[40]

According to energetic considerations, the 193nm photodissociation of CH_3S may lead to many exothermic channels other than process (2), for example

$$CH_3S(\tilde{X}) + h\nu(193nm) \rightarrow CH_2S(\tilde{X}^1A_1, \tilde{a}^3A_2, \tilde{A}^1A_2) + H(^2S) \quad (10)$$

$$\rightarrow CHS(\tilde{X}) + H_2. \quad (11)$$

For process (10), the exothermicities are -100, -59, and -53 kcal/mol for the formation of CH_2S in the $\tilde{X}^1A_1$, $\tilde{a}^3A_2$, and $\tilde{A}^1A_2$ states,[41,42] respectively. The exothermicity for process (11) is $\approx$-104 kcal/mol.[42] Although the good fits to the experimental data observed in Figs. 6(a) and 6(b) using Eq. (9) can be taken as evidence that process (2) is the major channel for the 193nm photodissociation of $CH_3S(\tilde{X})$, we cannot, however, eliminate other channels such as processes (10) and (11).

CONCLUSION

The distribution of $S(^3P_{2,1,0}; {}^1D_2)$ resulting from the 193nm photodissociation of $CH_3S(\tilde{X})$ prepared by process (1) has been determined by using 2+1 REMPI detection schemes and by calibrating the $S(^3P_{2,1,0}; {}^1D_2)$ formation from process (3). The fine-structure distribution of product $S(^3P_{2,1,0})$ is found to be nearly statistical, while the $S(^3P)$: $S(^1D)$ branching ratio is determined to be 0.15 : 0.85. Based on the potential energy curves calculated along the CH_3-S dissociation coordinate using the MCSCF and FOCI methods, we have rationalized the observed branching ratio for product S atoms. The MCSCF calculation shows that the curve crossing between $CH_3S(\tilde{A})$ and $CH_3S(\tilde{B})$ provides an efficient predissociation pathway for $CH_3S(\tilde{A})$ to form $CH_3(\tilde{X})$ + $S(^3P)$.

The geometries for $CH_3S(\tilde{X},\tilde{A})$ have been optimized using the MCSCF method. The geometrical parameters thus obtained are compared with those determined in previous calculations and experimental results.

The calibration of the S^+ signals from CH_3SCH_3 to that from CS_2 makes possible the estimation of the absolute 193nm photodissociation cross section of $CH_3S(\tilde{X})$.

ACKNOWLEDGEMENT

The authors thank Drs. M. W. Schmidt and T. S. Elbert for making available to us the GAMESS program, which is used for performing all the calculations presented in this article. Funds in the form of a Research Opportunity Award from NSF, which provided partial support for P.J.H.T. during his stay in Ames, are gratefully acknowledged.

REFERENCES

(1) See extensive references cited in *Dynamics of Molecular Photofragmentation*, Faraday Discussions of Chem. Soc., No. 82, 1986.

(2) M. N. R. Ashfold and J. E. Baggott, eds., *Molecular Photodissociation Dynamics*, Royal Society of Chemistry 1987.

(3) J. W. Hepburn in, *Vacuum Ultraviolet Photoionization and Photodissociation of Molecules and Clusters*, edited by C. Y. Ng (World Scientific, Singapore, 1991), p. 435.

(4) W. B. Tzeng, H.-M. Yin, W.-Y. Leung, J.-Y. Luo, S. Nourbakhsh, G. D. Flesch, and C. Y. Ng, J. Chem. Phys. 88, 1658 (1986).

(5) S. Nourbakhsh, C.-L. Liao, and C. Y. Ng, J. Chem. Phys. 92, 6587 (1989).

(6) S. Nourbakhsh, K. Norwood, H.-M. Yin, C.-L. Liao, and C. Y. Ng, J. Chem. Phys. 95, 5014 (1991).

(7) S. Nourbakhsh, K. Norwood, H.-M. Yin, C.-L. Liao, and C. Y. Ng, J. Chem. Phys. 95, 946, (1991).

(8) S. Nourbakhsh, H.-M. Yin, C.-L. Liao, and C. Y. Ng, Chem. Phys. Lett. 183, 348 (1991).

(9) P. Brewer, N. van Veen, and R. Bersohn, Chem. Phys. Lett. 91, 126 (1982).

(10) G. Black and L. E. Jusinski, J. Chem. Phys. 82, 789 (1985).

(11) G. Black and L. E. Jusinski, J. Chem. Soc. Faraday Trans. 2 82, 2143 (1986).

(12) R. J. Balla, H. H. Nelson, and J. R. McDonald, Chem. Phys. 109, 101 (1986).

(13) R. J. Balla, B. R. Weiner, and H. H. Nelson, J. Am. Chem. Soc. 109, 4804 (1987).

(14) G. S. Tyndall and A. R. Ravishankara, J. Phys. Chem. 93, 2426, 4707 (1989).

(15) K. Ohbayashi, H. Akimoto, and I. Tanaka, Chem. Phys. Lett. 52, 47 (1977).

(16) M. Suzuki, G. Inoue, and H. Akimoto, J. Chem. Phys. 81, 5405 (1984).

(17) Y.-C. Hsu, X. Liu, and T. A. Miller, J. Chem. Phys. 90, 6852 (1989).

(18) G. Black and L. E. Jusinski, J. Chem. Phys. 85, 5379 (1986).

(19) Y.-Y. Lee, S.-Y. Chiang, and Y. P. Lee, J. Chem. Phys. 93, 4487 (1990).

(20) S.-Y. Chiang and Y.-P. Lee, J. Chem. Phys. 95, 66 (1991).

(21) S. Nourbakhsh, K. Norwood, G.-Z. He, and C. Y. Ng, J. Am. Chem. Soc. 113, 6311 (1991).

(22) B. K. Janousek and J. I. Brauman, J. Chem. Phys. 72, 694 (1980).

(23) R. H. Nobes and L. Radom, Chem. Phys. Lett. 189, 554 (1992).

(24) K. K. Baldridge, M. S. Gordon, and D. E. Johnson, J. Chem. Phys. 91, 4145 (1987).

(25) B. Mouflih, C. Larrieu, and M. Chaillet, Chem. Phys. 119, 221 (1988).

(26) J. Fossey and J. Sorba, J. Mol. Struct. (Theochem), 186, 305 (1989).

(27) R. Fournier and A. E. DePristo, J. Chem. Phys. 96, 1183 (1992).

(28) C. Y. Ng, S.-W. Chiu, and W.-K. Li, J. Chem. Research, accepted.

(29) V. R. McCrary, R. Lu, D. Zakheim, J. A. Russell, J. B. Halpern, and W. M. Jackson, J. Chem. Phys. 83, 3481 (1985); J. W. Rabalais, J. M. McDonald, V. Scherr, and S. P. McGlynn, Chem. Rev. 71, 73 (1971).

(30) I. M. Waller and W. J. Hepburn, J. Chem. Phys. 87, 3261 (1987).

(31) W.-B. Tzeng, H.-M. Yin, W.-Y. Leung, J.-Y. Luo, S. Nourbakhsh, G. D. Flesch, and C. Y. Ng, J. Chem. Phys. 88, 1658 (1988).

(32) W. C. Wiley and I. H. McLaren, Rev. Sci. Instr. 26, 1150 (1955).

(33) D. J. Bamford, M. J. Dyer, and W. K. Bishel, Phys. Rev. A, 36, 3497 (1987).

(34) J. G. Calvert and J. N. Pitts, Jr., *Photochemistry* (Wiley, New York, 1966).

(35) H. Beijerinck and N. Verster, Physica 111C, 327 (1981).

(36) A. Yariv, *Quantum Electronics* (Wiley, New York, 1975).

(37) M. W. Schmidt, K. K. Baldridge, J. A. Boatz, J. H. Jensen, S. Koseki, M. S. Gordon, K. A. Nguyen, T. L. Windus, T. S. Elbert, QCPE Builetin, 10, 52 (1990).

(38) S. J. Singer, K. F. Freed, and Y. B. band, J. Chem. Phys. 79, 6060 (1983).

(39) C.-W. Hsu, C.-L. Liao, and C. Y. Ng, SPIE Conference Proceedings, *Optical Methods for Time- and State-Resolved Selective Chemistry*, edited by C. Y. Ng, Vol. 1638 (1992), in press.

(40) S. Nourbakhsh, K. Norwood, G.-Z. He, and C. Y. Ng, J. am. chem. Soc. 113, 6311 (1991).

(41) R. H. Judge, D. C. Moule, and G. W. King, J. Mol. Spectrosc. 81, 37 (1980).

(42) S. G. Lias, J. E. Bartmess, J. F. Liebman, J. L. Holmes, R. D. Levin, and W. G. Mallard, J. Phys. Chem. Ref. Data, 17, Suppl. 1 No. 1, 65 (1988).

PAPER 2.

A STUDY OF THE $S(^3P_{2,1,0}; {}^1D_2)$ PRODUCTION IN THE 193 nm PHOTODISSOCIATION OF HS and H_2S

ABSTRACT

The dynamics of the photodissociation processes, HS + hν(193nm) → H(^{2}S) + S(^3P_J,$^1D_2$) [process (A)] and H_2S + hν(193nm) → H_2(X) + S(^3P_J,$^1D_2$) [process (B)] have been studied using 2+1 resonance-enhanced-multiphoton-ionization techniques. By using the rate equation model and by calibrating the S(^3P_J,$^1D_2$) formation from processes (A) and (B) with that from the 193nm photodissociation of CS_2, we have determined the S(^{3}P) : S(^{1}D) branching ratios, the fine-structure distributions of S($^3P_{2,1,0}$), and the absolute cross sections for processes (A) and (B). The branching ratio S(^{3}P) : S(^{1}D) = 0.87 : 0.13 observed for process (A) supports the direct photodissociation mechanism for HS at 193nm via the excited repulsive HS($^2\Sigma$, $^2\Delta$) potential energy surfaces. The fine-structure distribution S($^3P_2$) : S($^3P_1$) : S($^3P_0$) = 0.68 : 0.24 : 0.08 for process (A) is colder than the statistical distribution. The absolute cross section for process (A) is estimated to be 1.1×10^{-18} cm^2. Process (B), which is estimated to have an absolute cross section of 0.3×10^{-18} cm^2, is minor compared to the formation HS + H in the 193nm photodissociation of H_2S.

INTRODUCTION

The ultraviolet and vacuum ultraviolet (VUV) photodissociation of H_2S has received considerable experimental[1-12] and theoretical[13-18] attention. Most of the experimental studies[1-5,7,8] have focused on the photodissociation process,

$$H_2S + h\nu(193nm) \rightarrow HS(X,v) + H. \quad (1)$$

Because of the rapid dissociation of vibrationally excited HS radicals in the $A^2\Sigma^+$ state, the determination of the HS(X) vibrational distribution has not been made by the laser-induced fluorescence method.[1] Previous laser photofragmentation time-of-flight (TOF) mass spectrometric[2,4,5] and Doppler spectroscopic[3] experiments indicate that HS(X) formed by process (1) is vibrationally excited up to v=6 with the HS vibrational distribution peaked strongly at v=0. Recently, Continetti et al.[5] have observed the 193nm photodissociation of HS(X,v) [process (2)] formed in process (1) at high photodissociation laser powers.

$$HS(X,v) + h\nu(193nm) \rightarrow H(^2S) + S(^3P,^1D) \quad (2)$$

By measuring the TOF distribution for H from process (2), they estimate that the branching ratio $S(^3P) : S(^1D)$ for process (2) is 3 : 1. Referring to the *ab initio* calculation[17], they suggest that $S(^3P)$ and $S(^1D)$ are produced by direct dissociation following the 193nm photoexcitation of HS from the ground $X^2\Pi$ state to the excited $^2\Sigma^-$

and $^2\Delta$ repulsive states, respectively. The 193nm photodissociation of HS to form S + H has also been reported in the recent photodissociation TOF mass spectrometric study of CH_3SH.[19]

As suggested by Roberge and Salahub,[18] the photodissociation process

$$H_2S + h\nu(193nm) \rightarrow H_2 + S(^3P_J;^1D_2) \qquad (3)$$

is a feasible channel which may be induced by the $2b_1 \rightarrow 6a_1$ excitation of H_2S. Below 2000 Å, S atoms have been observed in the flash photolysis of H_2S.[20] Recent multiphoton ionization studies[10,11] show that H_2S dissociates to form H_2 + $S(^3P,^1D,^1S)$ by two-photon absorption in the wavelength range of 285-297nm. However, process (3) has not been identified in previous photodissociation experiments. Thus, it may be concluded that the H_2 + S channel is of minor significance in the 193nm photodissociation of H_2S.

Using the 2+1 resonance-enhanced-multiphoton-ionization (REMPI) scheme to detect $S(^3P_J;^1D_2)$,[21] we have recently examined the 193nm photodissociation of the CH_3S radical.[22,23] By using the S^+ intensity from the 193nm photodissociation of CS_2 to calibrate the S^+ intensity from CH_3S, we have estimated the absolute photodissociation cross section for CH_3S at 193nm. The absorption cross section for CS_2 at 193nm is known.[24] The branching ratio $S(^3P)$: $S(^1D)$ and the fine-structure distribution $S(^3P_2)$: $S(^3P_1)$: $S(^3P_0)$ resulting from the 193nm photodissociation of CS_2 have been determined previously in VUV laser-induced fluorescence[25] and TOF mass spectrometric[26] experiments. Here, we report the application of the 2+1 REMPI scheme for detecting $S(^3P_{2,1,0};\ ^1D_2)$ formed by

processes (2) and (3). By careful analysis of the 193nm photodissociation laser power dependencies for the $S(^3P_2, {}^1D_2)$ formation from the 193nm photolysis of H_2S, we have determined the branching ratio $S(^3P)$: $S(^1D)$ and the fine-structure distribution $S(^3P_2)$: $S(^3P_1)$: $S(^3P_0)$ for process (2) as well as those for process (3).

EXPERIMENTAL

The schematic diagram of the experimental setup is shown in Fig. 1. A home-built TOF mass spectrometer of the two-stage Wiley-McLaren design (not shown here) is used to detect S^+ ions. The details of the experimental procedures have been described previously.[22] Briefly, a pulsed molecular beam of neat H_2S is produced by supersonic expansion through a pulsed valve (nozzle diameter = 0.5 mm, temperature $\approx$ 298K, stagnation pressure $\approx$ 125 Torr). The molecular beam is skimmed by a conical skimmer and intersects with both the dissociation and ionization lasers 15.3 cm downstream from the pulsed nozzle. The molecular beam source chamber and the dissociation chambers are pumped by a 2000 ℓ/s diffusion pump and a 50 ℓ/s turbomolecular pump, respectively. For a pulsed valve repetition rate of 17 Hz, the beam source and photodissociation chambers are maintained at pressures of $\approx 1 \times 10^{-4}$ and 2×10^{-6} Torr, respectively.

The ArF photodissociation laser (Questek 2460) is operated in the constant pulse energy mode. The laser beam is attenuated by layers of stainless steel wire mesh and is spatially filtered by two irises before being focused by a fused-silica lens (200 mm f.l.) to an $\approx$ 2x2 mm^2 spot in the intersection region. The ArF laser energies used are in the range of 160 to 1000 μJ/pulse.

The ionization of $S(^3P_{2,1,0}; {}^1D_2)$ is accomplished with an excimer laser (Lambda Physik EMG 201 MSC) pumped dye laser (FL 3002) system. The pulse energy, typically 200μJ/pulse, is monitored with a pyroelectric detector (Molectron J3-05). The dye laser beam propagates coaxially with the ArF laser beam into the reaction chamber and

Figure 1. Schematic diagram of the experimental setup.

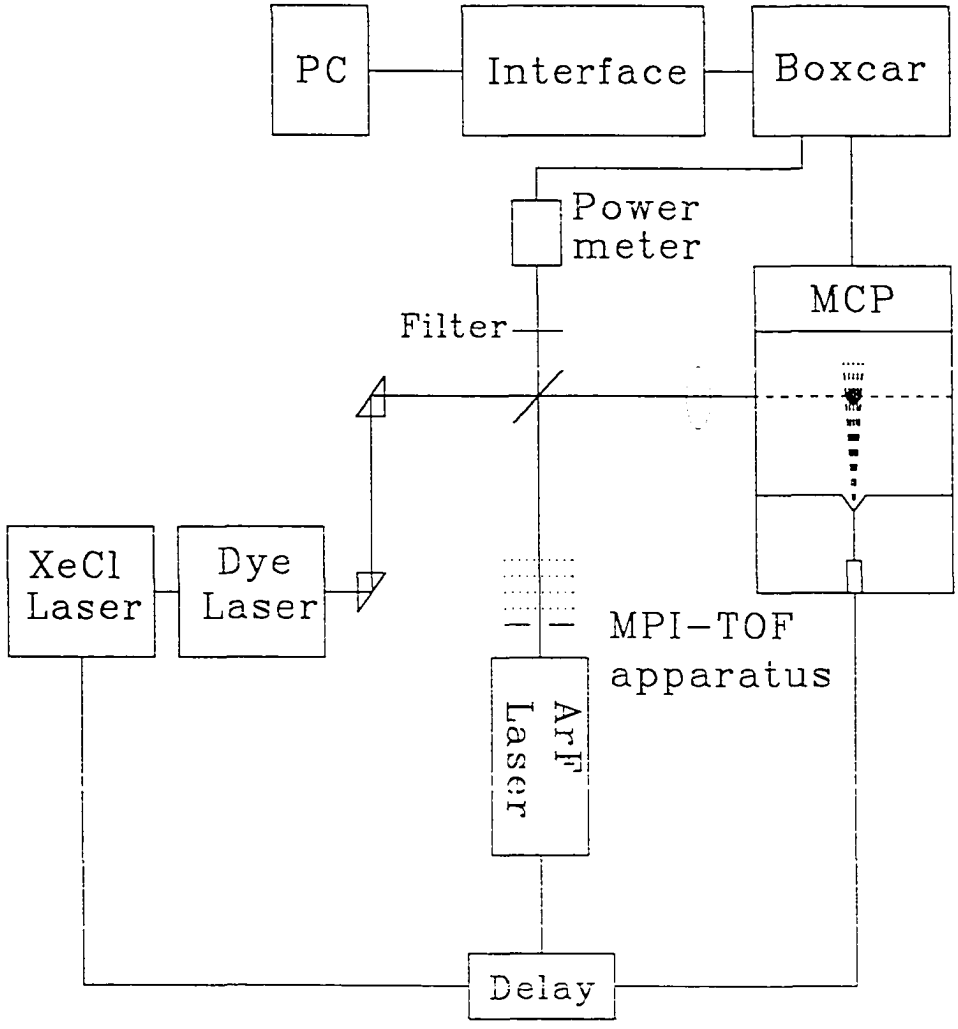
PC
Interface
Boxcar
Power
meter
MCP
Filter
XeCl
Laser
Dye
Laser
MPI-TOF
apparatus
ArF
Laser
Delay

intersects with the molecular beam at 90°.

The firing of the dissociation excimer laser is delayed by 630 μs with respect to the triggering pulse for opening the pulsed valve. The S^+ intensity remains nearly constant when the delay between the photodissociation and ionization lasers is varied in the range of 30-100 ns. Therefore, a delay of 50 ns between the two lasers is set for all the experiments. The firing sequence of the pulsed valve and the two lasers is controlled by two digital delay units (Stanford Research, Model DG 535). The ion signal from the microchannel plate (MCP) and the dye laser signal from the pyroelectric detector are fed into two identical boxcar integrators (Stanford Research, SR-250), which are interfaced to an IBM AT computer.

The CS_2 sample (99% purity) was obtained from Aldrich and the H_2S ($\geq$99.6% purity) was obtained from Matheson.

A. Detection of $S(^3P_{2,1,0})$ and $S(^1D_2)$

Probing of the $S(3^3P_J)$ and $S(3^1D_2)$ atomic states is accomplished by 2-photon absorption, $S(3^3P_J) \rightarrow S(4^3P_J)$ and $S(3^1D_2) \rightarrow S(4^1F_3)$, followed by absorption of a third photon to produce S^+ in the $^4S^\circ$ and $^2D^\circ$ states, respectively. The ionization peaks corresponding to the detection of $S(^3P_{2,1,0})$ and $S(^1D_2)$ appear in the wavelength region of 308-311 nm and at 288.19 nm, respectively.

The fine-structure distribution of $S(3^3P_{2,1,0})$ is measured by summation over the peak intensities corresponding to transitions to the upper $S(4^3P_{2,1,0})$ fine-structure levels.[27] The fine-structure distribution for $S(^3P_{2,1,0})$ from the 193nm photodissociation of CS_2 determined here using the 2+1 REMPI detection schemes is in excellent agreement with

that obtained using the VUV laser-induced fluorescence technique.[25]

B. $S(^3P)/S(^1D)$ branching ratio and absolute cross section for processes (1)-(3)

The rate equations applicable to processes (1), (2), and (3) are:

$$d[H_2S]/dt = -I(\sigma_1 + \sigma_3)[H_2S], \quad (4)$$

$$d[HS]/dt = I\sigma_1[H_2S] - I\sigma_2[HS], \quad (5)$$

$$d[S(2)]/dt = I\sigma_2[HS], \quad (6)$$

$$d[S(3)]/dt = I\sigma_3[H_2S]. \quad (7)$$

Here, I is the ArF laser photon intensity [# of photons/(cm^2·sec)] and σ_1, σ_2, and σ_3 represent the absolute cross sections for processes (1), (2) and (3), respectively. For each laser pulse, the number densities for H_2S ($[H_2S]$), HS ([HS]), and S from process (2) ([S(2)]) and process (3) [S(3)] are related to σ_1, σ_2, σ_3, σ_t (= $\sigma_1 + \sigma_3$), the laser flux (F) (# of photons/cm^2), and the initial number density of H_2S ($[H_2S]_o$) by the relations:

$$[H_2S] = [H_2S]_o\exp[-(\sigma_t)F], \quad (8)$$

$$[HS] = [H_2S]_o[\sigma_1/(\sigma_t-\sigma_2)][\exp(-\sigma_2F) - \exp(-\sigma_tF)]. \quad (9)$$

$$[S(2)] = [H_2S]_o[\sigma_1\sigma_2/(\sigma_t-\sigma_2)][-(1/\sigma_2)\exp(-\sigma_2F)+(1/\sigma_t)\exp(-\sigma_tF)+1/\sigma_2-1/\sigma_t]. \quad (10)$$

$$[S(3)] = [H_2S]_o(\sigma_3/\sigma_t)[1 - \exp(-\sigma_tF)]. \quad (11)$$

The S^+ signal resulting from the 2+1 REMPI is directly proportional to the number density of S, and σ_1 is known to be 6.8×10^{-18} cm^2.[6,20] In order to determine the $S(^3P)/S(^1D)$

branching ratio and the values for σ_2 and σ_3, the CS_2 calibration experiment is performed immediately after the measurement of the S^+ from H_2S.

In the estimation of the dissociation excimer laser flux, we assume that the mildly focused laser beam has a Gaussian beam profile.[28] The photodissociation laser spot size has also been checked by examining the burn spots on thermal paper at various distances from the focusing lens. The variation of the laser beam spot size with distance from the focusing lens is consistent with that predicted by the Gaussian beam profile. In the photodissociation region the ionization laser beam spot is smaller than the photodissociation laser beam spot.

RESULTS

The S^+ intensities (open circles) resulting from the REMPI of $S(^3P_2)$ and $S(^1D)$ formed by processes (1)-(3) are plotted as a function of the ArF photodissociation laser flux in Figs. 2(a) and 2(b), respectively. The slope for the S^+ intensity curve for $S(^3P_2)$ increases as F is increased, while the S^+ intensity curve for $S(^1D_2)$ shows a nearly linear dependency on F. The fraction of $S(^3P)$ is found to increase from 0.6 to 0.8 as F is increased in the range of $0.5\text{-}40\text{x}10^{16}$ photons/cm^2. The different laser flux dependencies observed for $S(^3P)$ and $S(^1D)$ indicate that $S(^3P, ^1D)$ atoms are produced by more than one process, and that the $S(^3P)$: $S(^1D)$ branching ratios due to these processes are different. We note that in the photodissociation experiment of CH_3S, where $S(^3P)$ and $S(^1D)$ are formed from CH_3S, the F dependencies for S^+ due to $S(^3P_2)$ and $S(^1D_2)$ are found to be the same.[21,22]

The cross sections and the $S(^3P_2)$: $S(^1D_2)$ branching ratios for processes (2) and (3) can be determined uniquely because process (3), which is linearly dependent on the photodissociation laser power, dominates at low F values, while process (2), which is proportional to the square of the photodissoication laser power, is expected to dominate at high F values. The simulations for the S^+ intensities due to ionization of $S(^3P_2)$ and $S(^1D_2)$ formed in processes (2) and (3) using Eqs. (10) and (11) are shown in Figs. 2(a) and 2(b) [$\triangle$ for process (2) and $\triangledown$ for process (3)]. The solid circles represent the sums of the contributions due to processes (2) and (3). The cross section values corresponding to the best fit are: $\sigma_1 = 6.5\text{x}10^{-18}$ cm^2, $\sigma_2 = 1.1\text{x}10^{-18}$ cm^2, and $\sigma_3 = 0.3\text{x}10^{-18}$ cm^2. The

Figure 2. Photodissociation laser flux (# photons/cm^2) dependence of S^+ signal due to the ionization of (a) $S(^3P_2)$ and (b) $S(^1D_2)$ formed by processes (2) ($\triangle$) and (3) ($\triangledown$). ($\circ$) experimental data; ($\bullet$) best fits using Eqs. (11) and (12).

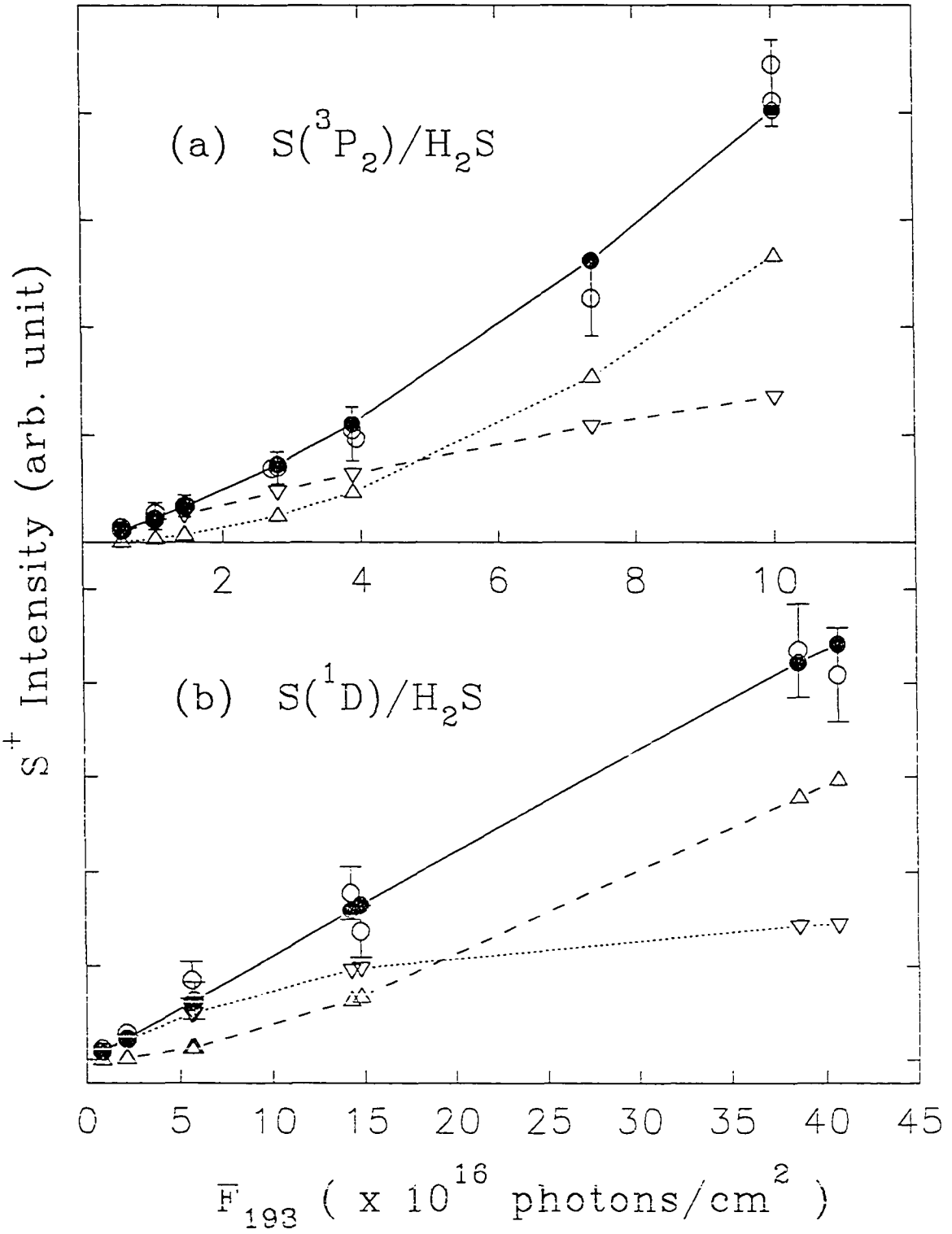
(a) S(3P2)/H2S
(b) S(1D)/H2S
S+ Intensity (arb. unit)
F193 (x 10^16 photons/cm^2)
0
5
10
15
20
25
30
35
40
45
2
4
6
8
10

absorption cross section for H_2S (6.8×10^{-18} cm^2)[6,20] is assumed to be $\sigma_t = \sigma_1 + \sigma_3$. This assumption is supported by the VUV photoabsorption and fluorescence experiment.[6] The $S(^3P)$: $S(^1D)$ branching ratios for processes (2) and (3) are determined to be 0.87 : 0.13 and 0.6 : 0.4, respectively.

The determination of the $S(^3P)$: $S(^1D)$ branching ratio from the $S(^3P_2)$: $S(^1D)$ ratio requires the values for the fine-structure distribution $S(^3P_2)$: $S(^3P_1)$: $S(^3P_0)$. The fine-structure distribution measured at F = 10×10^{16} photons/cm^2 is $S(^3P_2)$: $S(^3P_1)$: $S(^3P_0)$ = 0.68 ± 0.03 : 0.24 ± 0.03 : 0.08 ± 0.03. However, since the S^+ signal due to $S(^3P_0)$ is small, the population of $S(^3P_0)$ relative to $S(^3P_2)$ cannot be determined accurately at low F values. Based on this observation, we assume that the fine-structure distributions for both processes (2) and (3) are equal to that measured at F = 10×10^{16} photons/cm^2. Because the populations of $S(^3P_{2,1})$ are overwhelmingly greater than that of $S(^3P_0)$, the fine-structure distribution used has a very minor effect on the values reported here for the $S(^3P)$:$S(^1D)$ branching ratios of $S(^3P,^1D)$ formed in processes (2) and (3).

DISCUSSION

In order to gain some insight about the photodissociation process of HS, we show in Fig. 3 the *ab initio* potential energy curves calculated by Bruna and Hirsch[17] as a function of the H-S distance [r(H-S)] in atomic units (Bohr radius = a_o). The HS($^2\Sigma^-$) and HS($^2\Delta$) potential curves are repulsive and correlate asymptotically with the formation of S(^{3}P) + H(^{2}S) and S(^{1}D) + H(^{2}S), respectively. The *ab initio* calculation of Bruna and Hirsch does not report the oscillator strengths for transitions from the ground HS($X^2\Pi$) state to the HS($A^2\Sigma^+$, $^2\Sigma^-$, $^2\Delta$) states. In order to obtain estimates for these oscillator strengths, we have performed MCSCF calculations on HS using the GAMESS program.[28] In this calculation, the standard 6-31G** basis set with extended Rydberg functions is used to properly describe the excited states of HS. The MCSCF calculations predict that the vertical transition energies for HS(X) to HS(A), HS($^2\Sigma^-$), and HS($^2\Delta$) are 4.17, 5.99, and 7.05 eV, in good agreement with the values of 4.05, 6.19, and 7.05 eV, respectively, obtained by Bruna and Hirsch. The corresponding oscillator strengths for these transitions are predicted by the MCSCF calculations to be 0.0025, 0.0496, and 0.0167.

The branching ratio S(^{3}P) : S(^{1}D) = 0.87 : 0.13 determined here for process (2) is in qualitative agreement with the value of 3 : 1 deduced from the H-atom TOF mass spectrometric study.[5] If the 193nm photodissociation of HS(X,v) is direct via the repulsive HS($^2\Sigma^-$,$^2\Delta$) states, as suggested in Ref. 5,[5] the branching ratio S(^{3}P) : S(^{1}D) for process (2) should reflect the relative vibrational population of HS($X^2\Pi$) initially formed by process (1). The literature values for the relative vibrational populations for HS(X,v) formed in

Figure 3. *Ab initio* potential energy curves for HS plotted as a function of the H-S bond distance [r(H-S)] in atomic units (Bohr radius = a_o). Taken from Ref. 17.

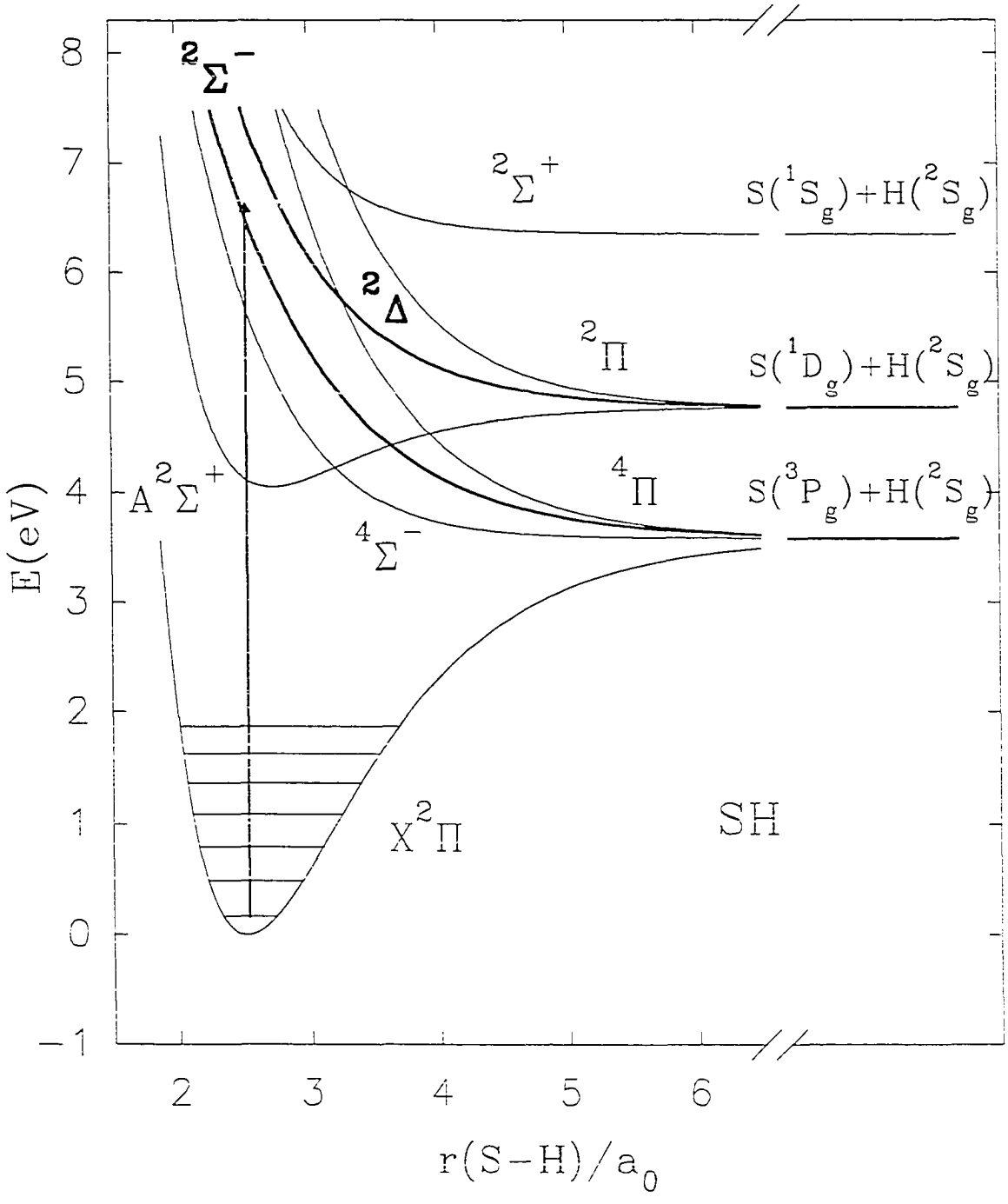
$^2\Sigma^-$
$^2\Sigma^+$
$S(^1S_g)+H(^2S_g)$
$^2\Delta$
$^2\Pi$
$S(^1D_g)+H(^2S_g)$
$A^2\Sigma^+$
$^4\Pi$
$S(^3P_g)+H(^2S_g)$
$^4\Sigma^-$
$X^2\Pi$
SH
E(eV)
$r(S-H)/a_0$
8
7
6
5
4
3
2
1
0
−1
2
3
4
5
6

process (1) have been examined and compared by Continetti et al.[5] They find that the H-TOF mass spectrometric results[2,5] agree within experimental uncertainties. Since the H-TOF[4] and the velocity-aligned Doppler shift[3] experiments are possibly complicated by a slow H signal, we quote here the relative populations, (v=0) : (v=1) : (v=2) : (v=3) : (v=4) : (v=5) : (v=6) = 0.728 : 0.056 : 0.051 : 0.037 : 0.040 : 0.018 : 0.001 determined by the H-TOF mass spectrometric experiment of Continetti et al.[5] According to the potential energy surfaces shown in Fig. 3, HS(X,v=0) can only be excited to HS($^2\Sigma^-$) by the absorption of a 193nm photon, the dissociation of which leads to the formation of S(^{3}P). The 193nm photoexcitation of HS(X,v≥1) can populate both the HS($^2\Sigma^-$) and HS($^2\Delta$) states. However, because of the favorable oscillator strength for the HS(X) → HS($^2\Sigma^-$) transition, the population of HS($^2\Sigma^-$) from HS(X,v≥1) by 193nm photoexcitation should also be significant, favoring the formation of S(^{3}P). Therefore, the high S(^{3}P)/S(^{1}D) ratio observed for process (2) can be attributed to the vibrational distribution of HS(X) formed in process (1) and the favorable oscillator strength for the HS(X) → HS($^2\Sigma^-$) transition.

Based on the energetic consideration, HS(X,v≥2) can be excited by the absorption of a 193nm photon to the repulsive HS($^2\Sigma^+$) state, which asymptotically correlates with S(^{1}S) + H(^{2}S). We have searched for S(^{1}S) using the REMPI detection scheme. The S^+ signal due to S(^{1}S) is not found, within the sensitivity of our experiment, indicating that a negligible intensity of S(^{1}S) atoms is formed by process (2). The excitation from HS(X,v) to HS(A) should be negligible except at v≥4.

The fine-structure distribution S($^3P_2$) : S($^3P_1$) : S($^3P_0$) = 0.68±0.03 : 0.24±0.03

: 0.08 ± 0.03 measured for process (2) is colder than the statistical distribution of 0.56 : 0.33 : 0.11. The experimental distribution may have a finite contribution from process (3). However, since the distribution is measured at a high F value, at which process (2) dominates, we may conclude that the experimental distribution represents mostly the fine-structure distribution for process (2). In a theoretical photodissociation study, Freed and co-workers show that photodissociation may proceed in two limiting cases,[30] depending on the relative available kinetic energy of the dissociation process. At low recoil energies, the fine-structure distribution is governed by the adiabatic potential surfaces and by the symmetry correlation. At the high energy limit, it is shown that a frame transformation will result in a statistical fine-structure distribution. According to the diagram[31,32] correlating the projections Ω of the total electronic angular momentum vectors of the separated atoms along the internuclear axis with the corresponding Ω values for the electronic states of the molecule, the $HS(^2\Sigma)$ state adiabatically correlates to $S(^3P_1)$ + $H(^2S)$. Since the major product observed is $S(^3P_2)$, we may conclude that the photodissociation process (2) is not a case of the low recoil energy which is governed by the adiabatic correlation.

The available recoil kinetic energy of 22,585 cm^{-1} for the formation of $S(^3P)$ from process (2) is much higher than the spin-orbit splitting $\Delta E_{so}(^3P_2 - {}^3P_1) = 396.93\ cm^{-1}$.[21,22] The translational adiabaticity parameter for spin-orbit transition is given as: $\zeta_t = \alpha \Delta E_{so}/\hbar v$, where α is the "range" of interatomic force and v is the recoil velocity. For $\zeta_t \leq 1$, the spin-orbit transition becomes efficient. For the recoil velocity corresponding to the available kinetic energy and the typical range parameter[31,33] $\alpha \approx$ 1-2 Å, ζ_t for this system

is significantly less than one. Therefore, we expect that nonadiabatic transitions between spin-orbit levels of $S(^3P_J)$ are efficient during the dissociation via the $HS(^2\Sigma^-)$ state. The fine structure distribution for $S(^3P_J)$ observed for process (2), although not statistical, may be close to the case of the high energy limit.

Process (3) was not observed in the H-atom TOF experiments of van Veen et al.[2] and Continetti et al.[6] In order to observe the secondary dissociation process (2), a high photodissociation laser power of 250 mJ/pulse was used in the experiment of Continetti et al. This, together with the small cross section for process (3) (0.3×10^{-18} cm^2) compared to that for process (1) (6.5×10^{-18} cm^2), may hinder the observation of process (3).

Due to the uncertainties involved in the calibration of the S^+ signals from CS_2 and H_2S, the absolute cross section $\sigma_2 = 1.1\times10^{-18}$ cm^2 obtained here is considered a rough estimate.

CONCLUSION

Using 2+1 REMPI detection schemes for $S(^3P_{2,1,0}; {}^1D_2)$, we have examined the 193nm photodissociation of HS(X,v) prepared by process (1). The branching ratio $S(^3P)$: $S(^1D)$ measured for process (2) is consistent with the direct photodissociation mechanism for HS(X,v) via the excited repulsive $HS(^2\Sigma)$ and $HS(^2\Delta)$ surfaces, as proposed by Continetti et al.[5] This experiment has identified the formation of $S(^3P_J, {}^1D_2)$ by the one-photon process (3). Process (3) is shown to be a minor channel compared to process (1). By calibrating the formation of $S(^3P_J; {}^1D_2)$ atoms from H_2S to those from CS_2, we have obtained estimates for the photodissociation cross sections of processes (2) and (3).

ACKNOWLEDGEMENT

A Research Opportunity Award from NSF, which provided partial support for P.J.H.T. during his stay in Ames, is gratefully acknowledged.

REFERENCES

(1) W. G. Hawkins and P. L. Houston, J. Phys. Chem. 73, 297 (1980).

(2) G. N. A. van Veen, K. A. Mohamed, T. Baller, and A. E. de Vries, Chem. Phys. 74, 261 (1983).

(3) Z. Xu, B. Koplitz, and C. Wittig, J. Chem. Phys. 87, 1062 (1987).

(4) X. Xie, L. Schnieder, H. Wallmeier, R. Boettner, K. H. Welge, and M. N. R. Ashfold, J. Chem. Phys. 92, 1608 (1990).

(5) R. E. Continetti, B. A. Balko, and Y. T. Lee, Chem. Phys. Lett. 185, 400 (1991).

(6) L. C. Lee, X. Wang, and M. Suto, J. Chem. Phys. 86, 4353 (1987).

(7) M. D. Person, K. Q. Lao, B. J. Eckholm, and L. J. Butler, 91, 812 (1989).

(8) B. R. Weiner, H. B. Levene, J. J. Valentini, and A. P. Baronavski, J. Chem. Phys. 90, 1403 (1989).

(9) R. J. Brudzynski, R. J. Sension, and B. Hudson, Chem. Phys. Lett. 165, 487 (1990).

(10) J. Steadman and T. Baer, J. Chem. Phys. 89, 5507 (1988),

(11) J. Steadman and T. Baer, J. Chem. Phys. 91, 6113 (1989).

(12) K. Kleinermanns, E. Linnebach, and R. Suntz, J. Phys. chem. 91, 5543 (1987).

(13) B. Heumann, R. Duren, and R. Schinke, Chem. Phys. Lett. 180, 583 (1991).

(14) S.-K. Shih, S. D. Peyerimhoff, and R. J. Buenker, Chem. Phys. 17, 391 (1976).

(15) K. C. Kulander, Chem. Phys. Lett. 103, 373 (1984).

(16) K. Weide, V. Staemmler, and R. Schinke, J. Chem. Phys. 93, 861 (1990).

(17) P. J. Bruna and G. Hirsch, Mol. Phys. 61, 1359 (1987).

(18) R. Roberge and O. R. Salahub, J. Chem. Phys. 70, 1177 (1979).

(19) S. Nourbakhsh, K. Norwood, H.-M. Yin, C.-L. Liao, and C. Y. Ng, J. Chem. Phys. 95, 946 (1991).

(20) J. G. Calvert and J. N. Pitts, Jr., *Photochemistry* (Wiley, New York, 1966).

(21) P. Brewer, van Veen, and R. Bershon, Chem. Phys. Lett. 91, 126 (1982); G. Black and Jusinski, J. Chem. Phys. 82, 789 (1985).

(22) C.-W. Hsu, C.-L. Liao, Z.-X. Ma, P. J. H. Tjossem, and C. Y. Ng, J. Chem. Phys., submitted.

(23) C.-W. Hsu, C.-L. Liao, and C. Y. Ng, SPIE Conference Proceedings, *Optical Methods for Time- and State-Resolved Selective Chemistry*, edited by C. Y. Ng, Vol. 1638 (1922), in press.

(24) V. R. McCrary, R. Lu, D. Zakheim, J. A. Russell, J. B. Halpern, and W. M. Jackson, J. Chem. Phys. 83, 3481 (1985); J. W. Rabalais, J. M. McDonald, V. Scherr, and S. P. McGlynn, Chem. Rev. 71, 73 (1971).

(25) I. M. Waller and W. J. Hepburn, J. Chem. Phys. 87, 3261 (1987).

(26) W.-B. Tzeng, H.-M. Yin, W.-Y. Leung, J.-Y. Luo, S. Nourbakhsh, G. D. Flesch, and C. Y. Ng, J. Chem. Phys. 88, 1658 (1988).

(27) D. J. Bamford, M. J. Dyer, and W. K. Bishel, Phys. Rev. A 36, 3497 (1987).

(28) A. Yariv, *Quantum Electronics* (Wiley, New York, 1975).

(29) M. W. Schmidt, K. K. Baldridge, J. A. Boatz, J. H. Jensen, S. Koseki, M. S. Gordon, K. A. Nguyen, T. L. Windus, and S. T. Elbert, QCPE Bulletin, 10, 52

(1990).

(30) S. J. Singer, K. F. Freed, and Y. B. Band, J. Chem. Phys. 79, 6060 (1983).

(31) Y. L. Huang and R. J. Gordon, J. Chem. Phys. 94, 2640 (1991).

(32) G. Herzberg, *Spectra of Diatomic Molecules* (van Nostrand Reinhold, New York, 1950).

(33) M. M. Graff and A. F. Wagner, J. Chem. Phys. 92, 2423 (1990).

PAPER 3.

A STUDY OF $S(^3P_{2,1,0}; {}^1D_2; {}^1S_0)$ PRODUCTION IN THE 193 nm PHOTODISSOCIATION OF CH_3SH

ABSTRACT

The dynamics of $S(^3P_{2,1,0}; {}^1D_2; {}^1S_0)$ production from the 193 nm photodissociation of CH_3SH has been examined by 2+1 resonance-enhanced-multiphoton-ionization (REMPI) techniques. Using the rate equation scheme, we have rationalized the intensities of $S(^3P_{2,1,0}; {}^1D_2; {}^1S_0)$ observed according to the sequential two-photon dissociative pathways, (A): $CH_3SH + h\nu$ (193nm) $\rightarrow CH_3S + h\nu$ (193 nm) $\rightarrow$ S and (B): $CH_3SH + h\nu$ (193 nm) $\rightarrow$ HS $+ h\nu$ (193 nm) $\rightarrow$ S, as the major mechanisms for S production. We have satisfactorily fitted the photodissociation laser power dependencies for $S(^3P)$ and $S(^1D)$ produced from CH_3SH by invoking photodissociation cross sections and branching ratios $S(^3P)/S(^1D)$ for CH_3S and HS similar to those determined previously in the 193 nm photodissociation of CH_3SCH_3 and H_2S. This observation supports that the 193 nm photodissociation of CH_3S and HS prepared from CH_3SH yield predominantly $S(^1D)$ and $S(^3P)$, similar to the cases for CH_3S prepared from CH_3SCH_3 and for HS prepared from H_2S, respectively. A small amount of $S(^1S_0)$ observed from the 193 nm photodissociation of CH_3SH is attributed to pathway (B).

INTRODUCTION

Knowledge about the formation of radical species from solar ultraviolet (UV) and vacuum ultraviolet (VUV) photolysis of organosulfur compounds, and about the subsequent photochemistry involving these radical species, is relevant to the modeling of atmospheric sulfur chemistry.[1] The previous experimental and theoretical studies of the UV and VUV photochemistry of CH_3SH have focussed on the primary photodissociation of CH_3SH according to the single-photon processes (1) and (2).[2-9]

$$CH_3SH + h\nu \xrightarrow{\sigma_1} CH_3S + H \quad (1)$$

$$CH_3SH + h\nu \xrightarrow{\sigma_2} HS + CH_3 \quad (2)$$

Detailed examination has not been made on the subsequent photodissociation of product CH_3S and HS [processes (3) and (4)] initially formed by processes (1) and (2), respectively.

$$CH_3S + h\nu \xrightarrow{\sigma_3} CH_3 + S \quad (3)$$

$$SH + h\nu \xrightarrow{\sigma_4} H + S \quad (4)$$

The dominance of process (1) over process (2) has been suggested in the UV and VUV flash photolysis of CH_3SH. The relative degree of S-H to C-S bond cleavage in the photodissociation of CH_3SH has been estimated to be 3:1 at 214 nm,[3] 0.63:0.37 at 195

nm,[2] and 0.79:0.21 at 185 nm.[4]. At 193 nm, the exothermicity at 0 K for processes (1) is -62 kcal/mol, while that for process (2) is -75.4 kcal/mol.[9] Based on the kinetic energy release measurement in the 193 nm photodissociation of CH_3SH,[7,8] the most probable internal energy for photo-fragments of process (2) corresponds to $\approx$30% of the available energy. According to the time-of-flight (TOF) spectrum of CH_3S measured by Kelly et al.,[8] the kinetic energy release for process (1) is peaked at $\approx$56 kcal/mol, indicating that the most probable internal excitation of CH_3S is $\approx$6 kcal/mol, about 10% of the available energy. This observation is consistent with the conclusion that the formation of CH_3S and H by process (1) at 193 nm involves the direct recoil of fragments on a repulsive energy surface. The recent *ab initio* calculation of the adiabatic electronic states by Mauflih et al.[6] has shown that the $CH_3SH(2^1A")$ potential energy surface accessed by a 193 nm excitation is bound in the S-H coordinate. Nevertheless, the observation of efficient S-H bond cleavage may be attributed to a strong coupling between the bound $CH_3SH(2^1A")$ state and the dissociative $CH_3SH(1^1A")$ state.[8]

The kinetic energy distribution observed for S in the 193 nm photodissociation TOF mass spectrometric study of CH_3SH by Nourbakhsh et al.[7] suggests that HS initially formed by process (2) may further dissociate by absorbing a second 193 nm photon according to process (4). The further photodissociation of HS has also been observed in the 193 nm photodissociation TOF mass spectrometric studies of H_2S. The results of these studies suggest that S atoms produced by process (4) are predominantly in the $S(^3P)$ ground state.[7,11] Similarly, 193 nm photodissociation studies of CH_3SCH_3 (Ref. 12) and

CH_3SSCH_3 (Ref. 13) reveal that the primary SCH_3 fragments may dissociate by the absorption of a second photon to produce S predominantly in the excited $S(^1D)$ state.

Direct measurements of the nascent electronic state distribution of $S(^3P_{2,1,0};\ ^1D_2)$ resulting from the 193 nm photodissociation of CH_3SCH_3 and H_2S have been made recently in our laboratory using 2 + 1 resonance-enhanced-multiphoton-ionization (REMPI) detection techniques.[10,14] By calibrating the S^+ intensities due to $S(^3P_{2,1,0};\ ^1D_2)$ formed from CH_3SCH_3 and H_2S at 193 nm to those from CS_2 [process (5)], we obtain estimates of $\approx 1.0\times10^{-18}$ cm^2 and 1.1×10^{-18} cm^2 for the absolute photodissociation cross sections for processes (3) and (4) at 193 nm, respectively.

$$CS_2 + h\nu\ (193\ nm) \rightarrow CS + S(^3P_{2,1,0};^1D_2) \qquad (5)$$

The absolute cross section for process (5) is known; and the branching ratio for $S(^3P)/S(^1D)$ (=2.78) and the fine structure distribution of $S(^3P_{2,1,0})$ formed by process (5) has been measured in detail by VUV laser-induced fluorescence[15] and TOF mass spectrometric methods.[16] The branching ratio $S(^3P)/S(^1D)$ determined for process (3) is 0.15/0.85, while that for process (4) is 0.87/0.13. We note that the detailed photodissociation dynamics of CH_3S and HS depend on their internal excitations and thus these cross sections and branching ratios are characteristic of CH_3S and HS prepared in the 193 nm photodissociation of CH_3SCH_3 and H_2S.

We have extended our investigation of the $S(^3P_{2,1,0};\ ^1D_2;\ ^1S_0)$ production from the 193 nm photodissociation of CH_3SH using the 2 + 1 REMPI detection method. In this

article, we analyze the production of S atoms from the photodissociation of CH_3SH at 193 nm according to the stepwise two-photon pathways, (A): $CH_3SH + h\nu$ (193nm) → $CH_3S + h\nu$ (193 nm) → S and (B): $CH_3SH + h\nu$ (193 nm) → HS + $h\nu$ (193 nm) → S, which are comprised of processes (1) and (3) and processes (2) and (4), respectively. Considering that the energetics for the formation of CH_3S and HS from the 193 nm photodissociation of CH_3SH are similar to the formation of CH_3S from CH_3SCH_3 and the formation of HS from H_2S, respectively,[9,17] we expect that the knowledge gained in previous studies about the photodissociation dynamics of CH_3S prepared from CH_3SCH_3 and of HS prepared from H_2S is useful for the data analysis of the $S(^3P_{2,1,0}; {}^1D_2)$ production in the photodissociation of CH_3SH.

Based on the measurement of the photodissociation laser power dependence for the $S(^3P)/S(^1D)$ branching ratio, we have also considered the single-photon photodissociation process (6) as a possible channel for the S production from CH_3SH.

$$CH_3SH + h\nu(193\ nm) \xrightarrow{\sigma_5} CH_4 + S \qquad (6)$$

EXPERIMENTAL

The experimental setup and procedures have been described in detail.[10,14] A home-built TOF spectrometer of the two-stage Wiley-McLaren design is used to detect S^+ ions. Briefly, a pulsed molecular beam of neat CH_3SH is produced by supersonic expansion through a pulsed valve (nozzle diameter = 0.5 mm, temperature $\approx$ 298° K, stagnation pressure = 120 torr). The molecular beam is skimmed by a conical skimmer before intersecting with both the photodissociation and ionization lasers 8.3 cm downstream from the skimmer. The molecular beam source chamber and the photodissociation chamber are differentially pumped by a diffusion pump and a turbomolecular pump, respectively. For the pulse valve operating at a repetition rate of 17 Hz, the beam source chamber and the photodissociation chamber are maintained at pressures of $\approx$ 1 x 10^{-4} and 2 x 10^{-6} Torr, respectively.

The ArF photodissociation laser (Questek 2460) is operated in a constant pulse energy mode. The laser beam is attenuated by layers of stainless steel wire mesh and is spatially filtered by two irises before being focused by a fused-silica lens (200 mm f.l.) to a spot of $\approx$ 2x2 mm^2 in the interaction region. The ArF laser energies used are in the range of 100-1000 μJ/pulse.

The ionization of $S(^3P_{2,1,0}; {}^1D_2; {}^1S_0)$ is accomplished with an excimer laser (Lambda Physik EMG 201 MSC) pumped dye laser (Lambda Physik FL3002) system. The pulse energy, typically $\approx$ 200 μJ/pulse, is monitored with a pyroelectric detector (Molectron J3-

05). The dye laser beam propagates coaxially with the ArF laser beam into the reaction chamber and intersects with the molecular beam at 90°.

The firing of the photodissociation laser is delayed by 640 μs with respect to the trigger pulse for opening the pulsed valve. A delay of 50 ns between the photodissociation and ionization lasers is set throughout all the experiments. The firing sequence of the pulsed valve and the two lasers is controlled by two digital delay units (Stanford Research, DG 535). The ion signal from the microchannel plate detector and the dye laser signal from the pyroelectric detector are fed into two identical boxcar integrators (Stanford Research, SR250), which are interfaced to an IBM AT computer.

The CS_2 sample (Aldrich, 99% purity) is degassed by a series of freeze-pump-thaw cycles. The CH_3SH (Matheson, 99% purity) is used without further purification.

A. Detection of $S(^3P_{2,1,0})$, $S(^1D_2)$, and $S(^1S_0)$

Probing of $S(3^3P_J)$, $S(3^1D_2)$ and $S(3^1S_0)$ atomic states is accomplished by two-photon absorption $S(3^3P_J) \rightarrow S(4^3P_J)$, $S(3^1D_2) \rightarrow S(4^1F_3)$, and $S(3^1S_0) \rightarrow S(4^1D_2)$, followed by absorption of a third photon to produce S^+ ion in the $^4S^0$, $^2D^0$, and $^2P^0$ states, respectively.[10,14,18-21] The S^+ peaks corresponding to the ionization of $S(^3P_{2,1,0})$, $S(^1D_2)$, and $S(^1S_0)$ appear at the respective wavelength regions of 308-311, 288.19, and 299.575 nm.[21]

The fine-structure distribution of $S(3^3P_{2,1,0})$ is measured by summation over the peak intensities corresponding to transitions to the upper $S(4^3P_{2,1,0})$ fine-structure levels.[22] The fine-structure distribution for $S(^3P_{2,1,0})$ formed in the 193 nm photodissociation of CS_2 is determined here using 2+1 REMPI detection schemes and is in excellent agreement with that obtained using the VUV laser-induced fluorescence technique.[15]

B. $S(^3P)/S(^1D)$ branching ratio and absolute cross section for processes (1)-(4) and (6)

The rate equations applicable to CH_3SH, CH_3S, HS, and S according to processes (1)-(4) and (6) are:

$$d[CH_3SH]/dt = - I\sigma_t[CH_3SH], \quad (7)$$

$$d[CH_3S]/dt = I\sigma_1[CH_3SH] - I\sigma_3[CH_3S], \quad (8)$$

$$d[HS]/dt = I\sigma_2[CH_3SH] - I\sigma_4[HS], \quad (9)$$

$$d[S(3)]/dt = I\sigma_3[CH_3S], \quad (10)$$

$$d[S(4)]/dt = I\sigma_4[HS], \quad (11)$$

$$d[S(6)]/dt = I\sigma_6[CH_3SH]. \quad (12)$$

Here, I is the ArF laser photon flux [# of photons/(cm^2.sec)] and σ_1, σ_2, σ_3, σ_4, σ_6, and σ_t represent the absolute cross sections for process (1), (2), (3), (4), (6), and the total absorption cross section of CH_3SH, respectively. For each laser pulse the number densities for CH_3SH([CH_3SH)], CH_3S([CH_3S]), HS ([HS]), and S([S(3)], [S(4)], and [S(6)] from processes (3), (4), and (6), respectively), are related to σ_1, σ_2, σ_3, σ_4, σ_6, σ_t, the laser fluence (F) (# of photons/cm^2) and the initial number density of CH_3SH ($[CH_3SH]_0$) by the relations:

$$[CH_3SH] = [CH_3SH]_0 \exp[-\sigma_t F], \quad (13)$$

$$[CH_3S] = [CH_3SH]_0 [\sigma_1/(\sigma_t - \sigma_3)] [\exp(-\sigma_3 F) - \exp(-\sigma_t F)], \quad (14)$$

$$[HS] = [CH_3SH]_0 [\sigma_2/(\sigma_t - \sigma_4)] [\exp(-\sigma_4 F) - \exp(-\sigma_t F)], \quad (15)$$

$$[S(3)] = [CH_3SH]_0 [\sigma_3\sigma_1/(\sigma_3 - \sigma_t)] [-\exp(-\sigma_tF)/\sigma_t + \exp(-\sigma_3F)/\sigma_3 + 1/\sigma_t - 1/\sigma_3], \quad (16)$$

$$[S(4)] = [CH_3SH]_0 [\sigma_4\sigma_2/(\sigma_4 - \sigma_t)] [-\exp(-\sigma_tF)/\sigma_t + \exp(-\sigma_4F)/\sigma_4 + 1/\sigma_t - 1/\sigma_4], \quad (17)$$

$$[S(6)] = [CH_3SH]_0 (\sigma_6/\sigma_t) [1 - \exp(-\sigma_tF)]. \quad (18)$$

The intensity of S^+ resulting from the 2 + 1 REMPI is directly proportional to the number density of S. In order to determine the $S(^3P)/S(^1D)$ branching ratio for $S(^3P_{2,1,0})$ formed from CH_3SH, calibrations are made between the S^+ signals due to the formation of $S(^3P_{2,1,0}; {}^1D_2)$ from CH_3SH and those from CS_2. Detailed calibration procedures have been described previously.[14]

The absolute total cross section σ_t is known to be 5.6×10^{-18} cm^2,[23]. Averaging the results of the previous UV photolysis studies,[1-3] we obtain an estimate of about 3/1 for the ratio σ_1/σ_2. In the data analysis, we assume that the branching ratios $S(^3P)/S(^1S)$ and absolute cross sections for the 193 nm photodissociation of HS and CH_3S prepared by processes (1) and (2) are similar to those formed from the 193 nm photodissociation of H_2S and CH_3SCH_3, respectively. That is, we fit the observed intensities for $S(^3P)$ and $S(^1D)$ from the 193 nm photodissociation of CH_3SH by using $\sigma_3 \approx 1.0 \times 10^{-18}$ cm^2, $\sigma_4 \approx 1.1 \times 10^{-18}$ cm^2, $S(^3P)/S(^1D) \approx 0.15/0.85$ for process (3), and $S(^3P)/S(^1D) \approx 0.87/0.13$ for process (4). The values for σ_1, σ_2, and σ_6 are also varied to fit the photodissociation laser power dependencies of the $S(^3P)$ and $S(^1D)$ intensities under the constraints that $\sigma_t \geq \sigma_1 + \sigma_2 + \sigma_6$ and $\sigma_1/\sigma_3 \approx 1/3$.

RESULTS AND DISCUSSION

The S^+ intensities observed in the 2 + 1 REMPI of $S(^3P)$ and $S(^1D)$ are plotted as a function of 193 nm photodissociation laser photon fluence in Figs. 1(a) and 1(b), respectively. The branching ratio $S(^3P)/S(^1D)$ from CH_3SH is found to change from 0.59/0.41 at F = $1x10^{16}$ photons/cm^2 to 0.43/0.57 at F = $8x10^{16}$ photons/cm^2. This observation, together with the relatively slow change for the slope of the S^+ intensity, especially the S^+ intensity due to $S(^3P)$ at low photon fluxes, supports that $S(^3P)$ and $S(^1D)$ atoms may also be produced by the single-photon process (6). For $h\nu$ = 147.9 kcal/mol (193 nm), process (6) is highly exothermic (ΔH_{f0} = -95.4 kcal/mol).[17] However, the potential barrier for process (6) may be high.

The determination of the $S(^3P)/S(^1D)$ branching ratio from the $S(^3P_2)/S(^1D)$ ratio requires knowledge of the fine-structure distribution $S(^3P_2)$: $S(^3P_1)$: $S(^3P_0)$. At F = $8x10^{16}$ photons/cm^2, the fine-structure distribution for $S(^3P_j)$ from CH_3SH is determined to be $^3P_2 : {}^3P_1 : {}^3P_0 = 0.66 \pm 0.04 : 0.23 \pm 0.04 : 0.11 \pm 0.04$, which is slightly colder than that expected from a statistical distribution. This distribution is slightly colder than that observed from CH_3SCH_3, but slightly hotter than that from H_2S. The small S^+ signal due to $S(^3P_0)$ prevents us from accurately determining the population of $S(^3P_0)$ relative to that of $S(^3P_2)$ at lower photon fluxes. Here, we assume that the fine-structure distribution measured at F = $8x10^{16}$ photons/cm^2 remains the same throughout the entire range of photon flux. Because the population of $S(^3P_2)$ is dominant in the production of

Figure 1. Photodissociation laser fluence (# photons/cm^2) dependence of S^+ signal due to the ionization of (a) $S(^1D)$ and (b) $S(^3P)$ formed by process (3) (▼), process(4) (△), and process (6) (□), (○) Experimental data; (●) best fits using Eqs. (16)-(18). The fitting requires that $\sigma_t = 5.6\text{x}10^{-18}$ cm^2, $\sigma_1/\sigma_2 = 3/1$, $\sigma_3 = 1.0\text{x}10^{-18}$ cm^2, and $\sigma_4 = 1.1\text{x}10^{-18}$ cm^2.

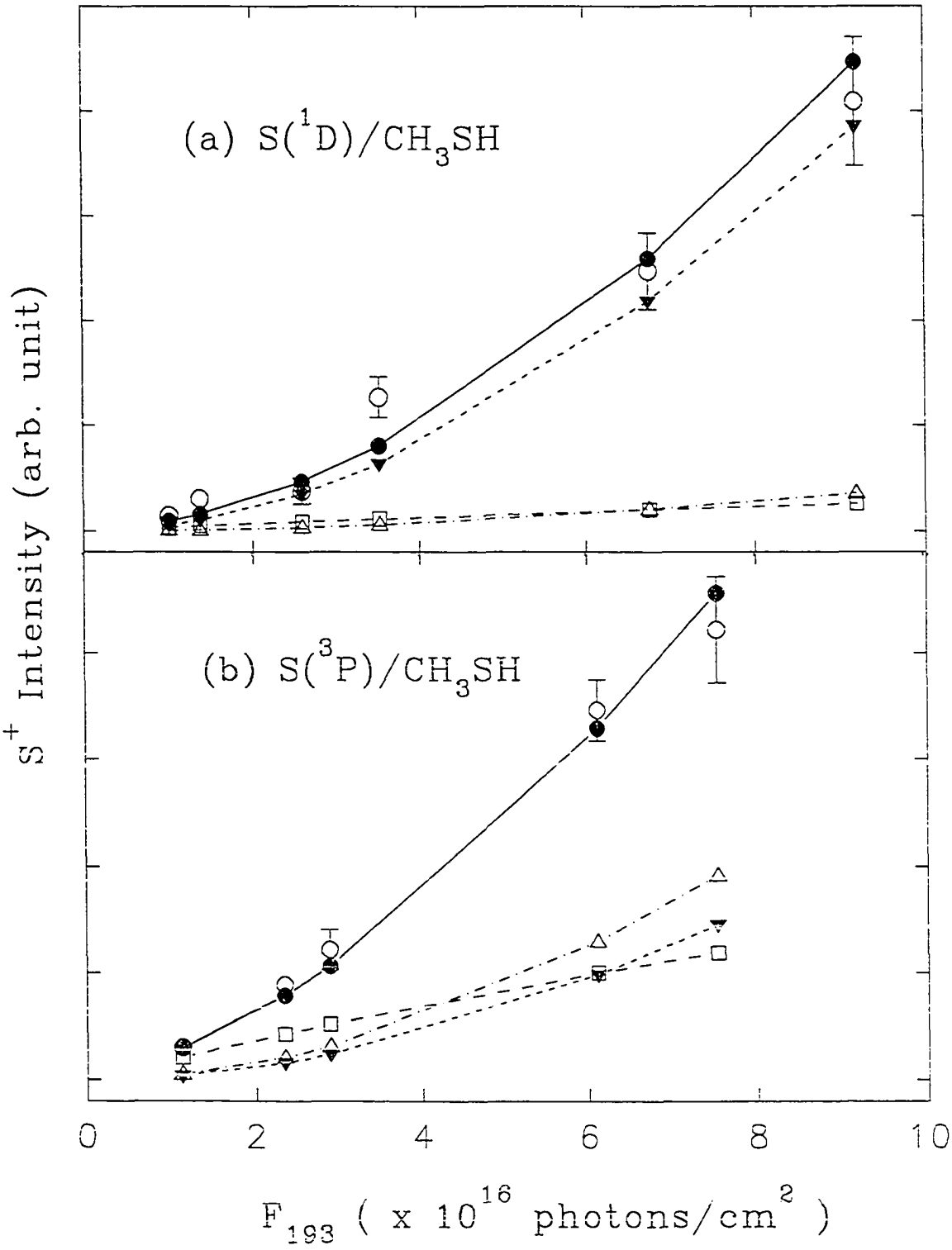
(a) S(1D)/CH3SH
(b) S(3P)/CH3SH
S+ Intensity (arb. unit)
0
2
4
6
8
10
F193 (x 10^16 photons/cm^2)

$S(^3P)$, the fine-structure distribution used should have a minor effect on the values reported for the branching ratios $S(^3P)/S(^1D)$ and for the photodissociation cross sections.

A typical simulation for the S^+ intensity due to the ionization of $S(^3P)$ and $S(^1D)$ formed in processes (1)-(4) and (6) using Eqs.(13)-(18) are also shown in Figs. 1(a) and 1(b) [▼ for process (3), ▲ for process (4), and □ for process (6)]. The solid circles represent the sum of best fitted values due to processes (3), (4), and (6). In this simulation, we assume that $\sigma_t = 5.6\text{x}10^{-18}$ cm^2, $\sigma_1/\sigma_2 = 3/1$, $\sigma_3 = 1.0\text{x}10^{-18}$ cm^2, and $\sigma_4 = 1.1\text{x}10^{-18}$ cm^2. The cross sections corresponding to the best fit are: $\sigma_1 = 3.7\text{x}10^{-18}$ cm^2, $\sigma_2 = 1.2\text{x}10^{-18}$ cm^2, and $\sigma_6 = 3.5\text{x}10^{-20}$ cm^2. The branching ratio $S(^3P)/S(^1D)$ due to the secondary processes (3) and (4) are 0.22/0.78 and 0.8/0.2, respectively. As shown in the figures, the overwhelming intensity of $S(^1D)$ produced at high photodissociation laser fluxes is attributable to the photodissociation process $CH_3S + h\nu \rightarrow S(^1D) + CH_3$, while the dissociation process $HS + h\nu \rightarrow H + S(^3P)$ accounts for the major intensity of $S(^3P)$ produced at high photon fluxes. The higher σ_t value, compared to $4.94\text{x}10^{-18}$ cm^2 for the sum $\sigma_1 + \sigma_2 + \sigma_6$, may be interpreted that the absorption of a 193 nm photon also induces other processes, such as rearrangement and/or dissociation, which do not lead to the production of S atoms.

Since the previous experimental values for σ_1/σ_2 in the vicinity of 193 nm fall in the range from 1.7/1 to 4/1, it is desirable to examine the effect of σ_1/σ_2 by adjusting its value in our fittings. By varying the value for σ_1/σ_2 in the range from 1.7/1 to 4/1 and by setting $\sigma_3 = 1.0\text{x}10^{-18}$ cm^2 and $\sigma_4 = 1.1\text{x}10^{-18}$ cm^2 , we find that the best fitted value

for $S(^3P)/S(^1D)$ of process (3) varies from 0.14/0.86 to 0.25/0.75, while that for process (4) is in the range from 0.72/0.28 to 0.87/0.13.

Attempts have also been made to fit the observed the photodissociation laser power dependencies for $S(^3P)$ and $S(^1D_2)$ from CH_3SH by setting the branching ratios $S(^3P)/S(^1D)$ = 0.15/0.85 and 0.87/0.13 for processes (3) and (4) respectively. The best fitted values for σ_3 and σ_4 are found to fall in the respective ranges of 0.9-1.2x10^{-18} cm^2 and 0.9-1.6x10^{-18} cm^2 when σ_1/σ_2 is varied in the range from 1.7/1 to 4/1.

According to the fittings described above, we may conclude that the values for σ_3 and σ_4 are most likely in the respective range of 0.9-1.2x10^{-18} cm^2 and 0.9-1.6x10^{-18} cm^2. The branching ratio $S(^3P)/S(^1D)$ for process (3) may be in the range from 0.14/0.86 to 0.25/0.75 and that for process (4) from 0.72/0.28 to 0.87/0.13. Because σ_6 is very small compared to other cross sections, its value is not sensitive to the fittings. Process (6) is important only at low photodissociation laser power. Further experiments are required to confirm the involvement of this process.

Based on the *ab initio* multiconfiguration self-consistence-field (MCSCF) potential energy surfaces for CH_3S calculated along the CH_3-S distance, Hsu et al.[14] have pointed out that the formation of $S(^3P_J)$ proceeds most likely by predissociation of $CH_3S(\tilde{C}\ ^2A_2)$ via the repulsive $CH_3S(\tilde{B}\ ^2A_2)$ state, while the formation of $S(^1D_2)$ may result from predissociation of CH_3S $(\tilde{C}\ ^2A_2)$ via the $CH_3S(\tilde{E}\ ^2E)$ repulsive state. The dominant production of $S(^1D_2)$ observed from CH_3S initially formed in the 193 nm photodissociation of CH_3SCH_3 has been attributed to the more favorable couplings of $CH_3S(\tilde{E})$ and $CH_3S(\tilde{C})$ state. The previous 193 nm photofragmentation study of CH_3SCH_3[13] indicates

that about 45% of the available energy appears as the most probable internal energies for product $CH_3S(\tilde{X})$ + CH_3. The direct excitation to the $CH_3S(\tilde{E})$ state from rovibrationally excited $CH_3S(\tilde{X})$ state is possible. The direct formation of $CH_3S(\tilde{E})$ radicals is expected to favor the $S(^1D_2)$ + $CH_3(\tilde{X}\,^2A'')$ dissociation channel. Assuming that the internal energies are equally distributed to all internal degrees of freedom, the most probable internal excitation for CH_3S prepared in the 193 nm photodissociation of CH_3SCH_3 is about 18 kcal/mol. This compares to the most probable internal excitation of $\approx$6 kcal/mol for CH_3S formed by process (1) at 193 nm. The extent of excitation to the $CH_3S(\tilde{E})$ state at 193 nm for colder CH_3S radicals prepared from CH_3SH is expected to be less, which in turn should lower the relative production of $S(^1D)$ compared to that observed from CH_3SCH_3. That is, the branching ratio for $S(^3P)/S(^1D)$ of process (3) at 193nm is most likely more than 0.15/0.85.

The *ab initio* potential energy curves calculated by Bruna and Hirsch[24] show that the $HS(^2\Sigma^-)$ and $HS(^2\Delta)$ potential surfaces are repulsive and correlate asymptotically with the formation of $S(^3P)$ + $H(^2S)$ and $S(^1D)$ + $H(^2S)$, respectively. The direct dissociation mechanism for the 193 nm photodissociation of HS(X,v) has been suggested previously in the H-atom TOF mass spectrometric[11] and REMPI studies.[10] The HS(X,v) radicals formed in the 193 nm photodissociation of H_2S are found to be overwhelmingly in the v=0 state. The dominant formation of $S(^3P)$ from HS(X) thus formed may be accounted for by the excitation $HS(X,v=0) \rightarrow HS(^2\Sigma^-)$. Energetically, a 193 nm photon can excite $HS(X^2\Pi,v\geq 1)$ to the $HS(^2\Delta)$ state which is expected to lead to the formation of $S(^1D)$. The previous kinetic energy release study of H_2S[11] indicates that the most probable internal

excitation for HS corresponds to $\approx 5\%$ (about 3 kcal/mol) of the available energy. Assuming that internal excitations are distributed equally to all internal degrees of freedom, we estimated that the most probable vibrational energy for HS(X) from CH_3SH is ≈ 7.5 kcal/mol. A higher population of HS(X, $v \geq 1$) formed in the 193 nm photodissociation of CH_3SH should lead to a $S(^3P)/S(^1D_2)$ branching ratio lower than 0.87/0.13 for process (4) at 193 nm.

The formation of S atoms in the $^1S_0$ state is observed here at high photodissociation laser power. The S^+ peak due to ionization of $S(^1S)$ at 299.575 nm can only be observed at high photon fluxes and is estimated to be ≈ 12 times less than that for $S(^1D)$ at 288.19 nm. However, the intensity for $S(^1S_0)$ relative to those for $S(^3P_J; {}^1D)$ cannot be quantified because $S(^1S)$ atoms are not produced in the calibration reaction (5). The formation of $S(^1S)$ was not found in the 193 nm photodissociation of CH_3SCH_3 and H_2S. It is unlikely that $S(^1S)$ can be produced from the photodissociation of CH_3S radicals because the product internal energy for CH_3S prepared from CH_3SH is expected to be lower than that from CH_3SCH_3. According to the *ab initio* potential energy curves of HS,[17] the excited $HS(^2\Sigma^+)$ state is repulsive and correlate asymptotically with the dissociation channel $S(^1S_0) + H(^2S)$. Since the formation of the $HS(^2\Sigma^+)$ state due to 193 nm excitation is energetically feasible for $HS(X^2\Pi, v \geq 2)$, the formation of $S(^1S_0)$ may be attributed to $HS(X^2\Pi, v \geq 2)$ formed in process (2) at 193 nm. We note that the 193 nm photoexcitation of H_2S can populate HS(X, v) states up to $v = 6$. However, the fact that $S(^1S)$ is not found may result from the very low population of $HS(X, v \geq 2)$ from H_2S. The detection of $S(^1S)$ is consistent

with the conclusion that the population of HS(X, $v \geq 2$) radicals is increased in the 193 nm photodissociation of CH_3SH.

State-to-state photodissociation cross sections for molecules are expected to depend on their internal energy distributions. The photodissociation cross sections for CH_3S and HS, estimated in the photodissociation studies of H_2S, CH_3SH, and CH_3SCH_3, represent cross sections averaged over the internal state distributions of CH_3S and HS characteristic of the photodissociation processes. We note that the width of the internal energy distributions for CH_3S and HS formed in the photodissociation of CH_3SCH_3 and CH_3SH are quite broad ($\approx$20 kcal/mol). The relatively broad internal energy distributions might suppress the variation of photodissociation cross sections for CH_3S and HS prepared from different precursor molecules. The MCSCF calculation indicates that the 193 nm excitation of $CH_3S(\tilde{X}, v=0)$ to $CH_3S(\tilde{C})$ has overwhelmingly the highest oscillator strength. If the subsequent predissociation processes from $CH_3S(\tilde{C})$ dictate the relative populations of $S(^3P)$ and $S(^1D)$, the minor excitation from vibrationally excited $CH_3S(\tilde{X})$ to $CH_3S(\tilde{E})$ would only have a minor effect on the $S(^3P)/S(^1D)$ branching ratio. In the case of HS, the oscillator strength for the transition $HS(X) \rightarrow HS(^2\Sigma^-)$ is the highest, and thus the formation of $S(^3P)$ should dominate if the vibrational distributions of HS formed in the photodissociation of H_2S and CH_3SH do not differ significantly. The good fitting obtained for the 193 nm photon flux dependencies for the formation of $S(^3P)$ and $S(^1D)$ from CH_3SH, using the σ_3 and σ_4 values and the $S(^3P)/S(^1D)$ branching ratios determined from H_2S and CH_3SCH_3, can be taken as support of the conclusion that the internal energy distributions of CH_3S and HS prepared from CH_3SH are not significantly different from

those from CH_3SCH_3 and H_2S. The similar fine-structure distributions for $S(^3P_{2,1,0})$ observed from H_2S, CH_3SH, and CH_3SCH_3 support that the photodissociation dynamics of HS and CH_3S are mostly governed by repulsive excited states.

In order to further examine the dependencies of the branching ratios $S(^3P)/S(^1D)$ and the photodissociation cross sections on the internal energy distributions of CH_3S and HS, it would be interesting to compare the cross sections and branching ratios $S(^3P)/S(^1D)$ for processes (3) and (4) measured using supersonically cooled CH_3S and HS beams.

CONCLUSION

Using 2 + 1 REMPI detection schemes for $S(^3P_{2,1,0}; {}^1D_2; {}^1S_0)$, we have examined the 193 nm photodissociations of $CH_3S(\tilde{X})$ and HS(X, v) prepared by processes (1) and (2), respectively. Although the cross sections for processes (1)-(4) and (6) and the $S(^3P)/S(^1D)$ branching ratios for processes (3) and (4) at 193 nm cannot be uniquely determined in this experiment, we find that good fits for the photodissociation laser power dependencies for $S(^3P)$ and $S(^1D)$ can be obtained by using similar values of σ_3 and σ_4 and the $S(^3P)/S(^1D)$ branching ratios determined in the previous 193 nm photodissociation experiments of CH_3SCH_3 and H_2S. This observation can be taken as evidence that the cross sections, as well as the relative intensities, for $S(^3P_J; {}^1D_2)$ formed in the photodissociation of CH_3S and HS prepared in the photodissociation of CH_3SCH_3 and H_2S at 193 nm, respectively, are similar to those from CH_3SH. The $S(^1S)$ observed in this experiment is attributed to the higher population of $HS(X, v \geq 2)$ resulting from the photodissociation of CH_3SH compared to that from H_2S. The one-photon process (6) for the formation of $S(^3P_J, {}^1D)$ is also suggested in this experiment as a minor channel in the 193 nm photodissociation of CH_3SH.

REFERENCES

(1) B. J. Finlayson-Pitts and J. N. Pitts, Jr., "Atmospheric Chemistry" (Wiley, New York, 1986).

(2) A. B. Callear and D. R. Dickson, Trans. Faraday Soc. 66 1987 (1970).

(3) L. Bridges and J. M. White, J. Phys. Chem. 77, 295 (1973).

(4) D. Kamra and J. M. White, J. Photochem. 4, 361 (1975).

(5) I. Tokue, A. Hiraya and K. Shobatake, Chem. Phys. 116, 449 (1987).

(6) B. Mouflih, C. Larrieu and M. Chaillet, Chem. Phys. 119, 221 (1988).

(7) S. Nourbakhsh, K. Norwood, H.-M. Yin, C.-L. Liao and C. Y. Ng, J. Chem. Phys. 95, 946 (1991).

(8) J. S. Keller, P. W. Kash, E. Jensen and L. J. Butler, J. Chem. Phys. 96, 4324 (1992).

(9) S.-W. Chiu, W.-K. Li, W.-B. Tzeng, and C. Y. Ng, J. Chem. Phys. 97, 6557 (1992).

(10) C.-W. Hsu, C.-L. Liao, Z.-X. Ma, P. J. H. Tjossem, and C. Y. Ng, Chem. Phys. Lett. 199, 78 (1992).

(11) R. E. Continetti, B. A. Balko and Y. T. Lee, Chem. Phys. Lett., 185, 400 (1991).

(12) S. Nourbakhsh, C.-L. Liao and C. Y. Ng, J. Chem. Phys, 92, 6587 (1989).

(13) S. Nourbakhsh, K. Norwood, H.-M. Yin, C.-L. Liao and C. Y. Ng, J. Chem. Phys. 95, 5014 (1991).

(14) C.-W. Hsu, C.-L. Liao, Z.-X. Ma, P. J. H. Tjossem and C. Y. Ng, J. Chem. Phys., 97, 6283 (1992).

(15) I. M. Waller and W. J. Hepburn, J. Chem. Phys., 87, 3261 (1987).

(16) W.-B. Tzeng, H.-M. Yin, W.-Y. Leung, J.-Y. Luo, S. Nourbakhsh, G. J. Flesch, and C. Y. Ng, J. Chem. Phys. 88, 1658 (1988).

(17) S. G. Lias, J. E. Bartmess, J. F. Liebman, J. L. Holmes, R. D. Levin, and W. G. Mallard, J. Phys. Chem. Ref. Data 17, Suppl. No. 1 (1988).

(18) P. Brewer, N. van Veen, and R. Bershon, Chem. Phys. Lett. 91, 126 (1982).

(19) G. Black and L. E. Jusinski, J. Chem. Phys. 82, 789 (1985)

(20) G. Black and L. E. Jusinski, J. Chem. Soc. Faraday Trans. 2 82, 2143 (1986).

(21) T. V. Venkitachalam and A. S. Rao, Appl. Phys. B 52, 102 (1991).

(22) D. J. Bamford, M. J. Dyer and W. K. Bishel, Phys. Rev. A 36, 3497 (1987).

(23) J. G. Calvert and J. N. Pitts., Photochemistry (Wiley, New York, 1966).

(24) P. J. Bruna and G. Hirsch, Mol. Phys., 61, 1359 (1987).

PAPER 4

ROTATIONALLY RESOLVED NONRESONANT TWO-PHOTON IONIZATION OF SH

ABSTRACT

The threshold photoelectron (PE) spectrum for nascent SH formed in the ultraviolet photodissociation of H_2S has been measured using the nonresonant two-photon pulsed field ionization (N2P-PFI) technique. The rotationally-resolved N2P-PFI-PE spectrum of SH indicates that photoionization dynamics favors the rotational angular momentum change $\Delta N \leq 0$ with the ΔN values up to -3, an observation similar to that found in the PFI-PE spectra of OH (OD) and NO. The ionization energy for $SH(X^2\Pi_{3/2})$ is determined to be 84,057.5$\pm$3 cm^{-1} (10.4219$\pm$0.0004 eV). The spin-orbit splitting for $SH(X^2\Pi_{3/2,1/2})$ is 377$\pm$2 cm^{-1}, in agreement with the literature value. This study illustrates that the PFI-PE detection method can be a sensitive probe for the nascent internal energy distribution of photoproducts.

INTRODUCTION

The study of molecular photoionization by high resolution photoelectron (PE) spectroscopy has been most valuable for the understanding of detailed photoionization dynamics and for obtaining accurate spectroscopic and energetic information about neutral and ionic species.[1] However, the typical energy resolution of 5-25 meV attained by conventional PE spectroscopic techniques is generally insufficient for obtaining rovibronically-resolved PE spectra of polyatomic species. With the recent development of the laser pulsed field ionization (PFI)[2] method, a version of the zero-kinetic-energy (ZEKE) PE technique,[3,4] the energy resolution for PE spectroscopy has improved to sub-wavenumbers, approaching that achieved in optical spectroscopy. Rotationally and vibrationally resolved PFI-PE spectra have been reported for many diatomic molecules[5-15] and for polyatomic species.[16-29] Due to the simplicity and the high resolution achieved by the PFI method, its application is expected to expand rapidly, covering many more molecular species in the near future.

Most of previous PFI-PE studies applied the resonance-enhanced[23,25,28] two-color laser excitation, or the single vacuum ultraviolet (VUV)[5-9, 14-19,21] laser excitation schemes. Recently, Bondybey and co-workers have demonstrated that PFI-PE spectra for NO (Ref. 13), H_2S (Ref. 20), CH_3I (Ref. 24), CS_2 (Ref. 22), and $(NO)_2$ (Ref. 29) can be obtained with good sensitivity by using the one-color nonresonant two-photon (N2P) excitation. In many cases, the N2P-PFI-PE spectra are found to be surprisingly similar to those acquired by the single VUV photon ionization scheme.

Since the single VUV photon and two-photon excitation schemes are governed by different selection rules, we expect differences in the resulting PFI-PE spectra. When molecular species under investigation are excited directly from their molecular ground states in the N2P scheme, and the excitation process is mediated by an intermediate repulsive state, the PFI-PE spectra are free from modulated structures observed in a resonant experiment. The recent N2P-PFI study on CH_3I indicates that the involvement of a dissociative intermediate state along the C-I dissociation coordinate allows the observation of a longer C-I stretching vibrational progression of CH_3I^+ compared to that found in a HeI PE spectroscopic study.[24] The N2P-PFI scheme is very attractive because of its high sensitivity and the availability of commercial pulsed dye lasers with an output range of 200-400 nm, as required for the ionization of most polyatomic species at their thresholds.

An exciting development of PFI-PE spectroscopy is that it allows high resolution PE studies for not only stable molecules, but also transient radicals. Elegant PFI-PE experiments on radicals such as OH (OD) (Ref. 14) and CH_3 (Ref. 21) and $C_6H_5CH_2$ (benzyl radical)[28] have been made recently by the groups of White and Weisshaar, respectively. The PE studies of transient molecules and radicals is traditionally a difficult field, partly because of the difficulties involved in the preparation of specific transient species of interest. Transient species prepared by pyrolysis, discharge, and fast chemical reactions are often internally excited. This, coupled with the relatively poor energy resolution used in conventional PE spectroscopic studies, makes the assignment of the PE features and ionization threshold difficult.

It has been well-demonstrated that many rotationally and vibrationally cold radicals can be prepared with high purity and intensity using a pulsed laser photodissociation radicals source.[30,31] The ideal combination of the PFI-PE detection and pulsed radical beam source provides the sensitivity needed for high resolution PE studies of radicals. The application of high resolution PFI-PE spectroscopy to the study of transient species has just begun, and its impact on the energetic and spectroscopic measurements of transient radicals is expected to continue for many years to come.

As part of the effort in our laboratory to characterize the structure and energetics of combustion-related polyatomic molecules and radicals by photoionization and photodissociation methods,[30-37] we have undertaken N2P-PFI studies of selected organosulfur species. Here, we present the N2P-PFI-PE spectrum of SH and its assignment. In this experiment, a one-color three-photon process is involved. That is, the SH radicals are first prepared by the single-photon dissociation process,

$$H_2S + h\nu \rightarrow SH(X^2\Pi_{3/2,1/2}) + H. \qquad (1)$$

The subsequent ionization of SH is accomplished by N2P excitations of SH to high-n Rydberg states [$SH^*(n)$] followed by PFI of $SH^*(n)$.

$$SH(X^2\Pi_{3/2,1/2}) + 2h\nu \rightarrow SH^*(n) \rightarrow SH^+(X^3\Sigma^-) + e^- \qquad (2)$$

The two additional photons absorbed by SH in process (2) are furnished by the same laser pulse which induced the dissociation of H_2S in process (1).

EXPERIMENTAL

A schematic diagram of the experimental apparatus is shown in Fig. 1. The experimental apparatus is modified from the laser ionization time-of-flight (TOF) mass spectrometer used in previous photodissociation studies.[38,39] A two-stage microchannel plate detector and a set of simple aperture lenses have been added for PE detection below the photoionization region and opposite to the ion TOF tube.

For this experiment, H_2S (Union Carbide, 99% purity) is used without further purification. The H_2S sample (7%) seeded in Ar carrier gas (total stagnation pressure $\approx$ 2.5 bar) is introduced into the photoionization region by supersonic expansion through a pulsed valve with a nozzle diameter of 0.5 mm. The molecular beam is skimmed by a conical skimmer (1 mm in diameter, 3.8 cm from the nozzle) before intersecting with a tunable laser beam (90°, 8.3 cm downstream from the skimmer). Both the pulsed valve and the dye laser are operated at a repetition rate of 13 Hz.

The molecular beam source chamber is pumped by a freon-trapped, 6 in. diffusion pump (pumping speed $\approx$ 2,000 ℓ/s), while the photoionization chamber and the ion-TOF tube are evacuated by two 50 ℓ/s turbomolecular pumps. During the experiment, the beam source chamber and the photoionization chamber are maintained at pressures of about $1x10^{-4}$ and $2x10^{-6}$ Torr, respectively.

The second harmonic output of an excimer (Lambda Physik EMG 201 MSC) pumped-dye laser (Lambda Physik FL 3002) is focused into the photoionization region by a 200 mm focal length fused-silica lens. Coumarin 102 dye is used to produce the

Figure 1. Cross sectional view of the ion-TOF and PFI-PE apparatus: (1)photodissociation and photoionization chamber; (2) photodissociation and photoionization region; (3) beam source chamber; (4) pulsed valve; (5) skimmer; (6) ion TOF tube; (7) ion microchannel plate detector; and (8)electron microchannel plate detector.

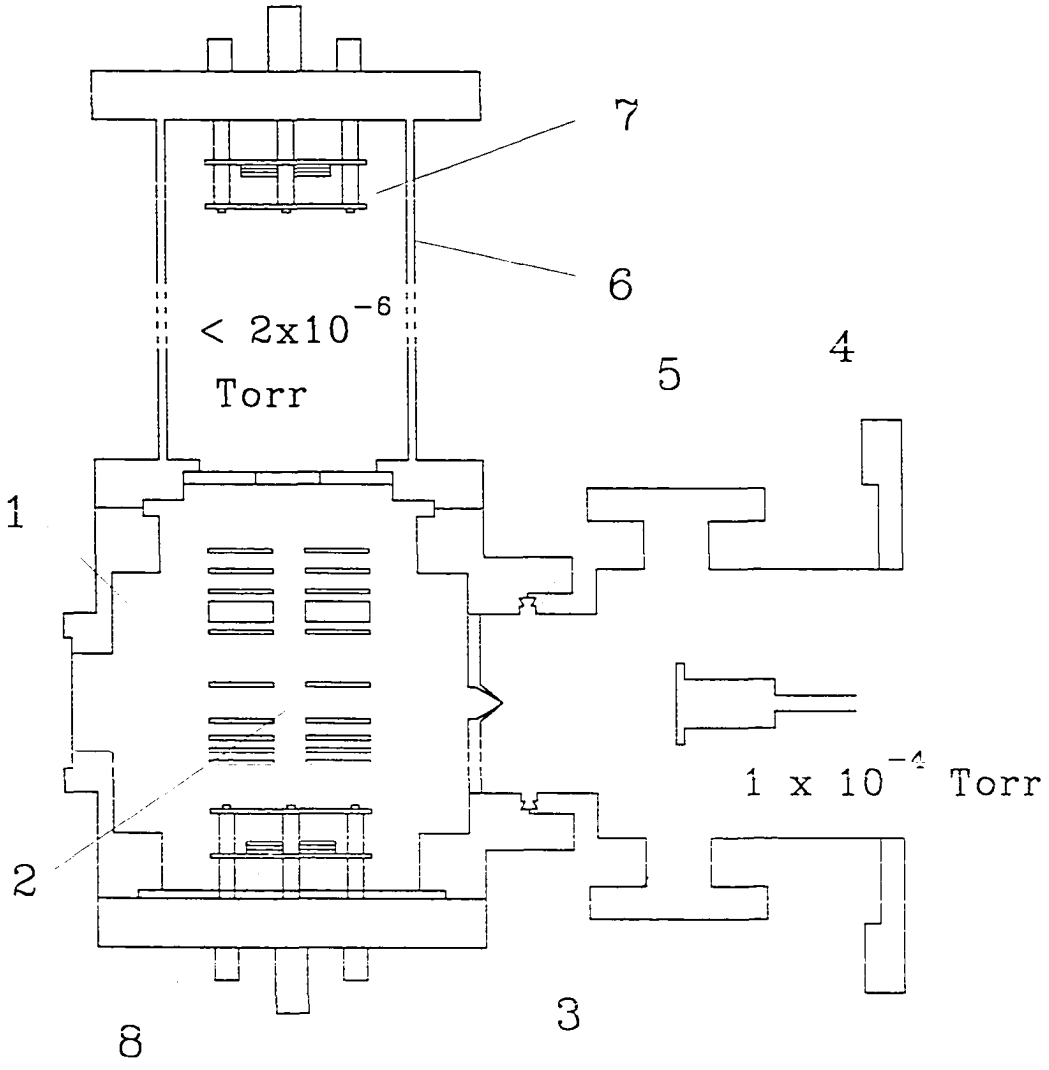
7
6
< 2x10^-6
Torr
5
4
1
1 x 10^-4 Torr
2
8
3

fundamental output in the 468-481 nm region. Typical laser pulse energies used in the second harmonic output range of 234-240 nm are 1.2 mJ, as monitored with a pyroelectric detector. The wavelength calibration is made using the known ZEKE spectrum of atomic sulfur,[40] which is produced by the multiphoton laser photodissociation of H_2S.

Ion detection using the ion TOF mass spectrometer has been described in detail previously.[38,39] Here, a constant electric field of 280 V/cm is used to extract the ions formed in the photoionization region. Since the N2P ionization processes compete with many multiphoton ionization and fragmentation channels, it is necessary to optimize the SH^+ ion signal by varying the dye laser power. As indicated above, the SH^+ formation is expected to be the result of a three-photon process. This expectation is confirmed by the observed laser power dependence of the SH^+ signal.

The ZEKE/PFI detection scheme relies on delayed PFI of long-lived high-n Rydberg states populated by laser excitation at a few wavenumbers below the ionization threshold. In this experiment, the firing of the photodissociation and excitation laser is delayed by 650 μs with respect to the triggering pulse for opening the pulsed valve. A pulsed field of 1.1 V/cm with a width of 1 μs is applied to the repeller plate 4.5 μs after firing the dye laser. The pulsed field serves to field-ionize the molecular species in high-n Rydberg states as well as to extract the electrons thus formed to the microchannel plate electron detector. The firing sequence of the pulsed valve, dye laser, and pulsed electric field is controlled by two digital delay units (Stanford Research DG535). The electron signal from the electron detector and the laser energy signal from the pyroelectric detector are fed into two identical boxcar integrators (Stanford Research SR250), which are

interfaced to an IBM/AT computer. The electron and laser energy signals are averaged for 30 shots at each laser wavelength.

The bandwidth of the dye laser is 0.2 cm^{-1} for the fundamental and $\approx$0.4 cm^{-1} for the second harmonic outputs. For a two-photon ionization process, the resolution due to the ionization laser is expected to be $\approx$0.8 cm^{-1}. In order to examine the PE energy resolution of this experiment, we have reproduced the N2P-PFI-PE spectrum for H_2S reported previously.[20] Figure 2 shows a section of the N2P-PFI-PE spectrum for H_2S, together with the assignment, in the region of 84,388-84,496 cm^{-1} (2x42,194-2x42,248 cm^{-1}) obtained using a pulsed field of 0.55 V/cm. In this experiment, the excitation laser is delayed by 450 μs[41] with respect to the triggering pulse for opening the pulsed valve. Since the spectrum of Fig. 2 is similar to that obtained by Bondybey and co-workers,[20] we conclude that the PE energy resolution achieved in this experiment is similar to that used in the previous experiment.

Figure 2. N2P-PFI-PE spectrum for H_2S in the region of 42,194-42,248 cm^{-1}, together with the rotational assignment (see Ref. 20), obtained using a pulsed field of 0.55 V/cm. The PE signals [$I(e^-)$] have not been normalized with the photoionization laser pulse energy.

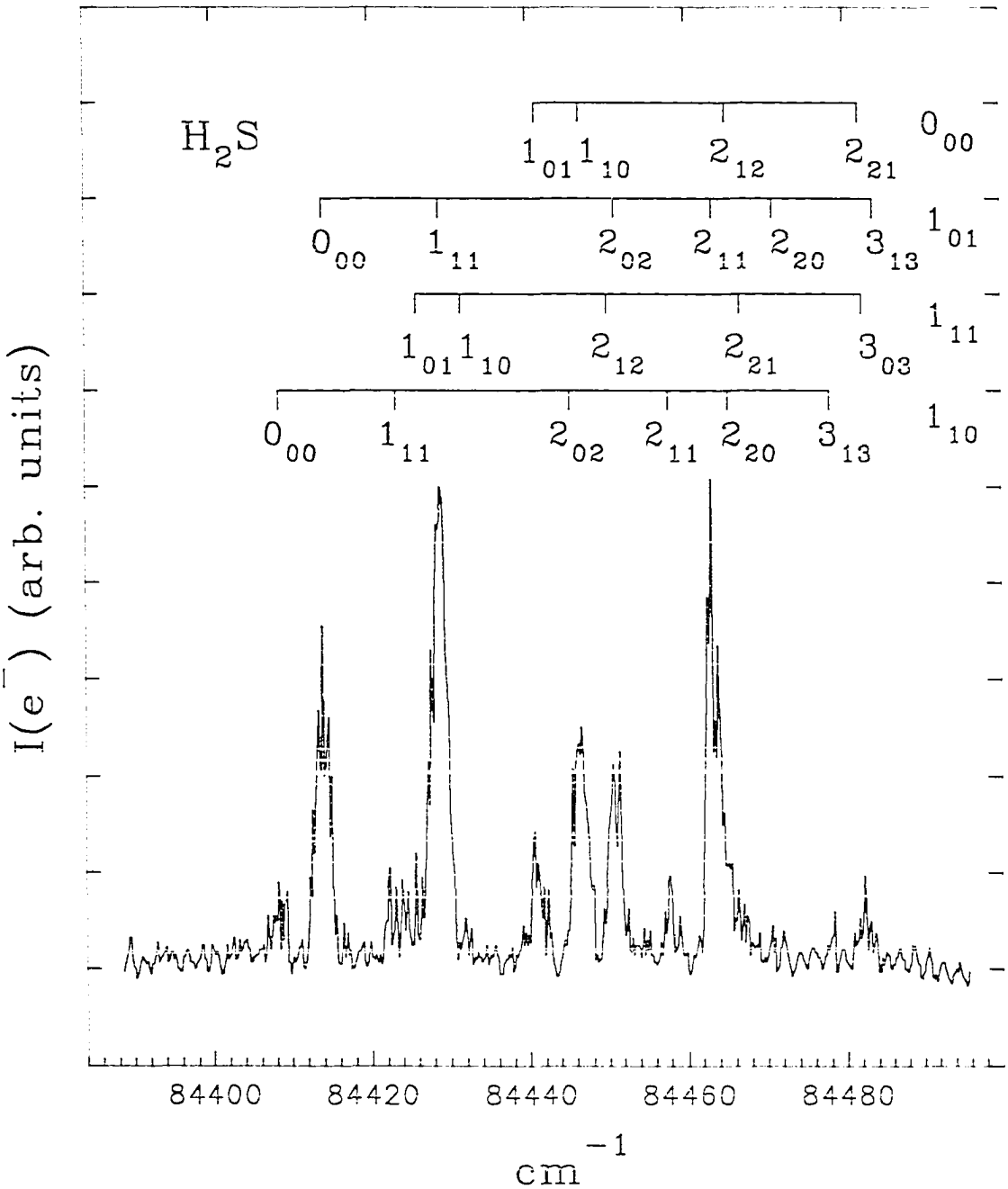
H2S
1 01 1 10
2 12
2 21
0 00
0 00
1 11
2 02
2 11
2 20
3 13
1 01
1 01 1 10
2 12
2 21
3 03
1 11
0 00
1 11
2 02
2 11
2 20
3 13
1 10
I(e⁻) (arb. units)
84400
84420
84440
84460
84480
cm⁻¹

RESULTS AND DISCUSSION

The photoionization efficiency (PIE) spectrum for SH^+ observed in the region 83,000-85,080 cm^{-1} (2x41,500-2x42,540 cm^{-1}) is depicted in Fig. 3. Here, we note that SH^+ ions are formed by N2P ionization instead of PFI. Since SH^+ is produced by a three-photon process, the SH^+ signals have been normalized by the cubic power of the laser energy. The N2P-PIE spectrum is roughly similar to the PIE spectrum for SH^+ measured in a VUV PIE experiment.[42]

The ionization energy (IE) for H_2S is 10.4683 ± 0.0002 Ev ($84,432\pm2$ cm^{-1})[20], which is higher than that for SH (10.43 ± 0.03 Ev)[43]. As shown in Fig. 3, the PIE for SH^+ rises above the background level at $\approx$83,320 cm^{-1} (2x41,660 cm^{-1}), an energy lower than the IE of SH. The gradual increase in the PIE for SH^+ is consistent with the interpretation that some of the SH radicals formed by process (1) in the energy range of 41,500-42,540 cm^{-1} are internally excited. The previous photodissociation study of H_2S by Weiner et al.[44] indicates that the excited $SH(^2\Pi_{1/2})$ spin-orbit state, which lies 376.96 cm^{-1} (Ref. 45) above the ground $SH(X^2\Pi_{3/2})$ state, is significantly populated. The population ratios $SH(X^2\Pi_{3/2})/SH(^2\Pi_{1/2})$ are measured to be 1.48 and 1.18 at the photolysis wavelengths of 222 and 248 nm, respectively. The same study also found that the rotational state distributions of SH formed by process (1) at 193, 222, and 248 nm are nearly identical and can be characterized by a rotational temperature of $\approx$300 K.[44] Although vibrationally excited SH radicals are also produced, it is well known from previous photodissociation experiments that $SH(X^2\Pi)$ radicals of process (1) at these

Figure 3. N2P-PIE spectrum for SH^+ in the region of 41,500-42,540 cm^{-1}. The SH^+ ion signals [$I(SH^+)$] have been normalized by the cubic power of the laser pulse energy.

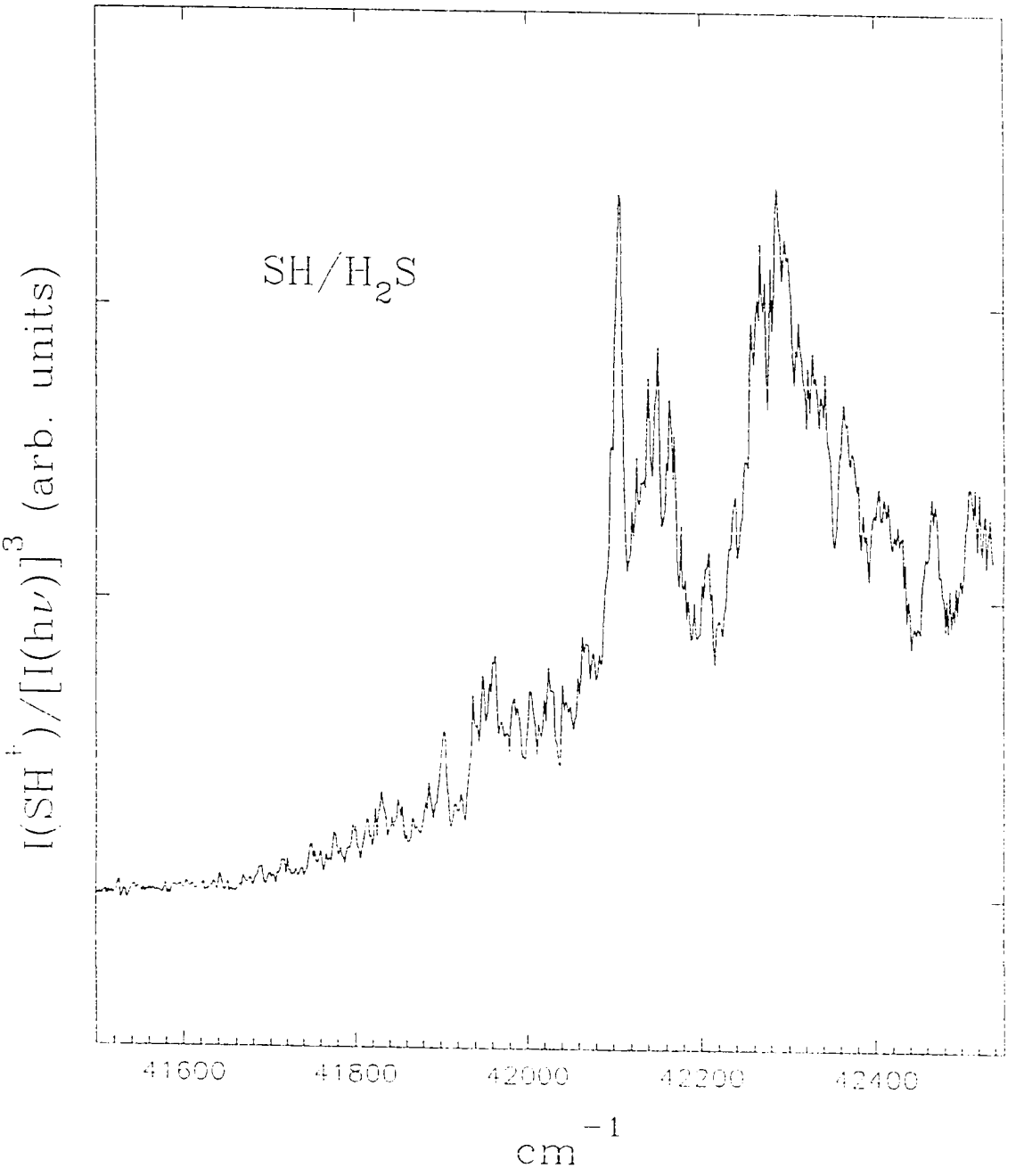
SH/H2S
I(SH+)/[I(hν)]3 (arb. units)
41600
41800
42000
42200
42400
cm−1

photolysis wavelengths are predominantly in the $v=0$ vibrational ground state.[46]

Figures 4(a) and 5(a) show the N2P-PFI-PE spectra for SH observed in the regions 83,100-83,800 and 83,800-84,500 cm^{-1}, respectively. The pulsed field of 1.1 V/cm used here corresponds to a Stark shift[47] of ≈ 3.1 cm^{-1} for a PFI-PE peak center. This shift has not been corrected for in the figures. The PE signals plotted in the figures have been normalized to the cubic power of the laser energy. We expect that the structures at energies below 84,432 cm^{-1}, the IE for H_2S, result predominantly from the N2P-PFI of SH formed in process (1). Two strong PE peaks at 41,579.7 cm^{-1} and 41,778.1 cm^{-1} [marked (▾) in Fig. 4(a)] are identified as the PFI-PE peaks for sulfur atom, corresponding to the ionization transitions $S^+(^4S^\circ_{3/2}) \leftarrow S(3p^4\ ^3P_1)$ and $S^+(^4S^\circ_{3/2}) \leftarrow S(3p^4\ ^3P_2)$, respectively.[40] The latter peak is found to overlap with PE peaks of SH.

Some features observed close to the IE of H_2S may be due to the hot band ionization of H_2S. Since H_2S^+ and SH^+ are formed by two-photon and three-photon processes, respectively, it is possible to examine the influence of H_2S ionization on the PFI-PE spectrum of SH by measuring the spectrum at different laser pulse energies. Figures 6(a) and 6(b) show the spectra taken at laser pulse energies of 1.2 and 0.7 mJ, respectively. As shown in these figures, the relative intensities for the PE peaks observed in the region of 41,600-42,100 cm^{-1} remain essentially unchanged, whereas the intensities for most of the PE features in the region greater than 42,100 cm^{-1} increase significantly with respect to those for PE peaks in the 41,600-42,100 cm^{-1} region as the laser energy is decreased. At the lower laser energy of 0.7 mJ, the PE band in the region greater than 42,100 cm^{-1} becomes dominant compared to those at lower energies. This observation

Figure 4. (a) N2P-PFI-PE spectrum for $SH(X^2\Pi_{3/2,1/2})$ in the region of 41,550-41,900 cm^{-1}. The PE signals [$I(e^-)$] have been normalized by the cubic power of the laser pulse energy. The two peaks marked by triangles at 41,579.7 cm^{-1} and 41,778.1 cm^{-1} are identified as the PFI-PE peaks for sulfur atom, corresponding to the ionization transitions $S^+(^4S^\circ_{3/2}) \leftarrow S(3p^4\ ^3P_1)$ and $S^+(^4S^\circ_{3/2}) \leftarrow S(3p^4\ ^3P_2)$, respectively.
(b) Simulated PE spectrum for $SH(X^2\Pi_{3/2,1/2})$ in the region of 41,550-41,900 cm^{-1}. The positions of the S_{i2} and T_{i2} ($i = F_1^+$, F_2^+, and F_3^+) rotational branches (dashed lines) are not included in the simulation.

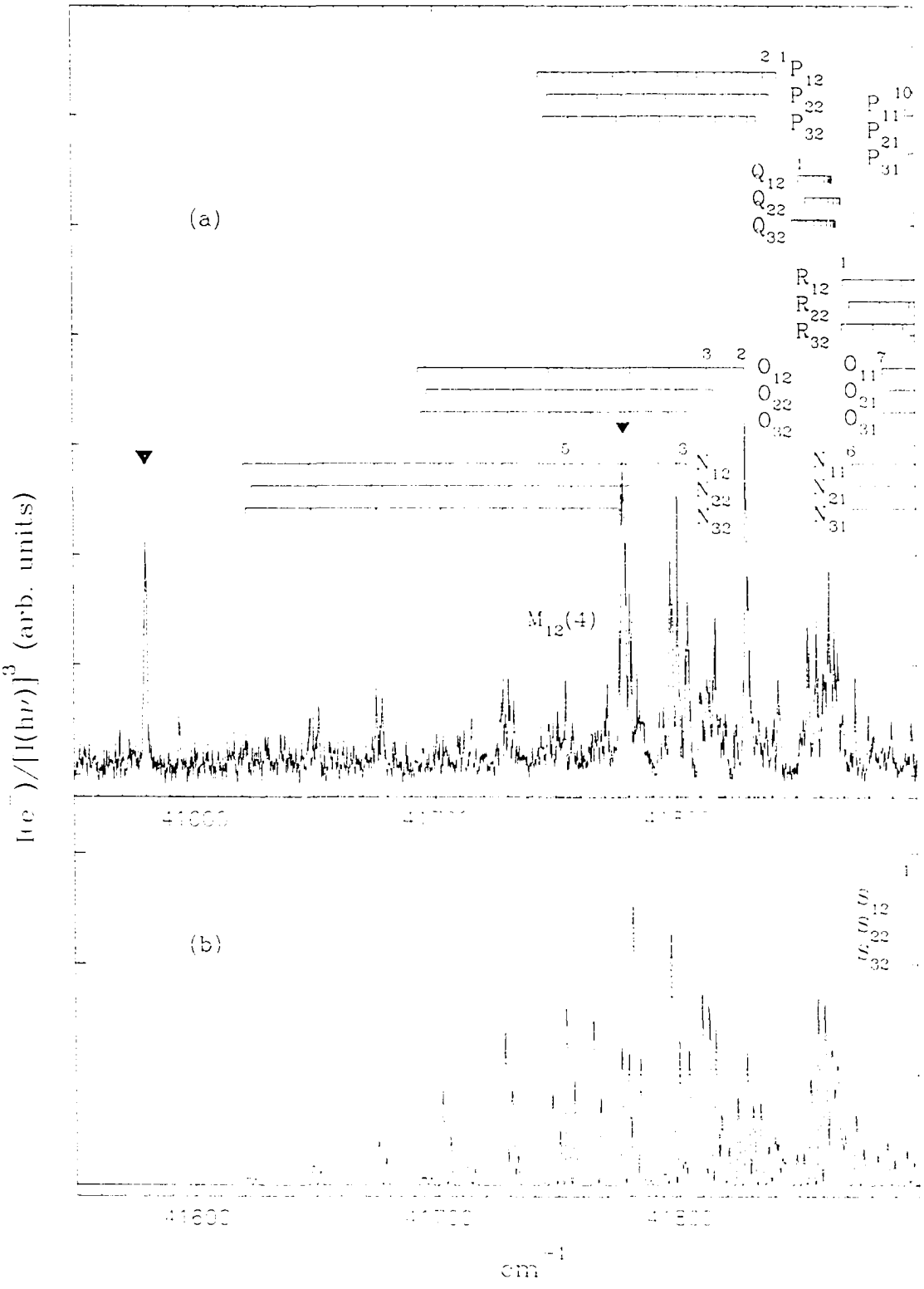
(a)
(b)
P_{12}
P_{22}
P_{32}
Q_{12}
Q_{22}
Q_{32}
R_{12}
R_{22}
R_{32}
O_{12}
O_{22}
O_{32}
N_{12}
N_{22}
N_{32}
$M_{12}(4)$
$[I(\tilde{\nu})/[I(h\nu)]^3$ (arb. units)
cm^{-1}

Figure 5. (a) N2P-PFI-PE spectrum for $SH(X^2\Pi_{3/2,1/2})$ in the region of 41,900-42,250 cm^{-1}. The PE signals [$I(e^-)$] have been normalized by the cubic power of the laser pulse energy. The PE peaks marked by asterisks are attributable to hot band ionization of H_2S.

(b) Simulated PE spectra for $SH(X^2\Pi_{3/2,1/2})$ in the region of 41,900-42,250 cm^{-1}. The position for the S_{i1}, T_{i1}, S_{i2}, and T_{i2} [i = 1 (F_1^+), 2 (F_2^+), and 3 (F_3^+)] rotational branches are shown by dashed lines. These branches are not included in the simulation.

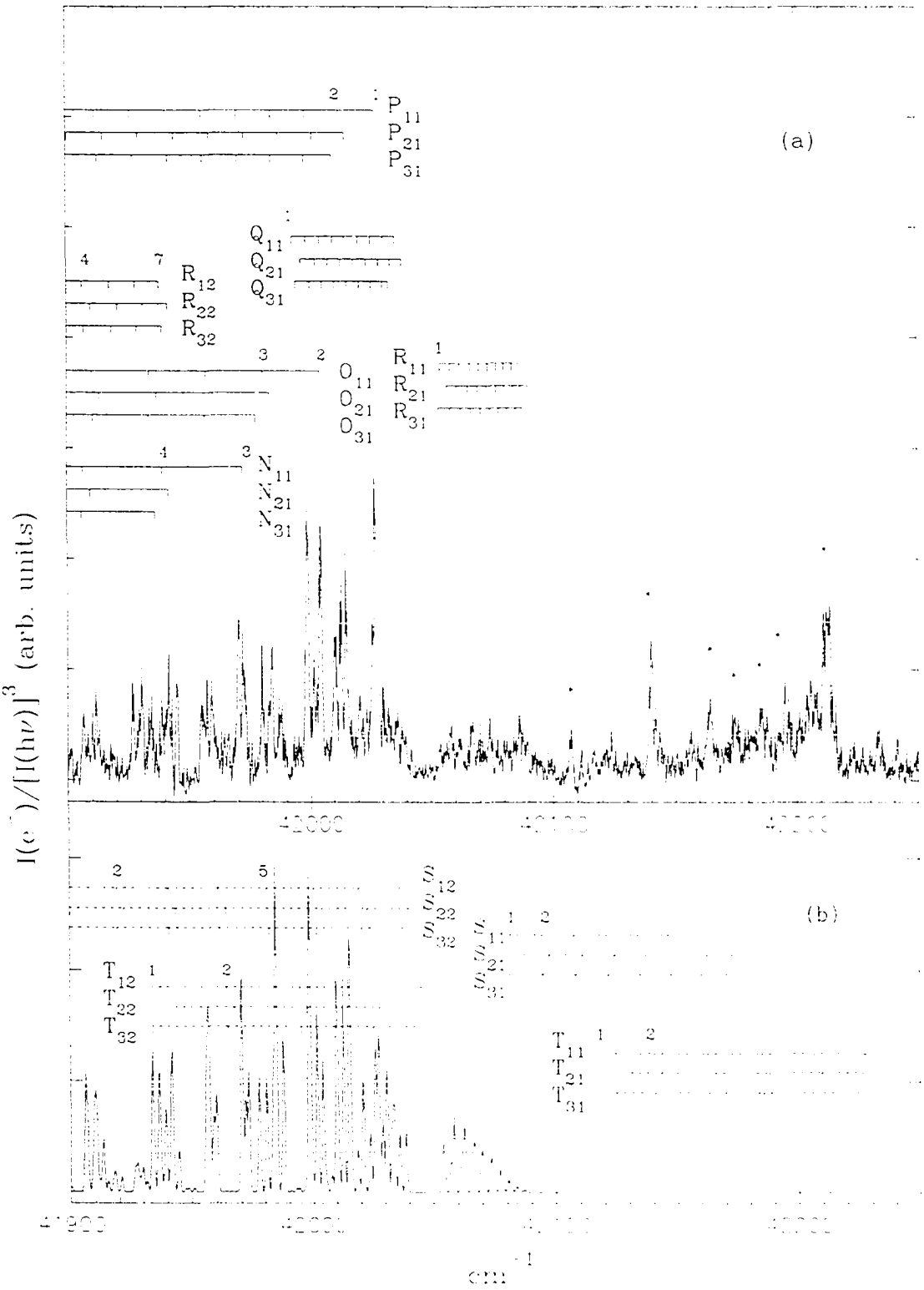
(a)
(b)
P_{11}
P_{21}
P_{31}
Q_{11}
Q_{21}
Q_{31}
R_{12}
R_{22}
R_{32}
O_{11}
O_{21}
O_{31}
R_{11}
R_{21}
R_{31}
N_{11}
N_{21}
N_{31}
S_{12}
S_{22}
S_{32}
T_{12}
T_{22}
T_{32}
T_{11}
T_{21}
T_{31}
$I(e^{-})/[I(h\nu)]^{3}$ (arb. units)
cm^{-1}

Figure 6. PFI-PE spectra in the region of 41,520-42,300 cm^{-1} obtained at a laser pulse energy (a) 1.2 mJ and (b) 0.7 mJ. The PE signals [$I(e^-)$] have not been normalized by the laser pulse energy.

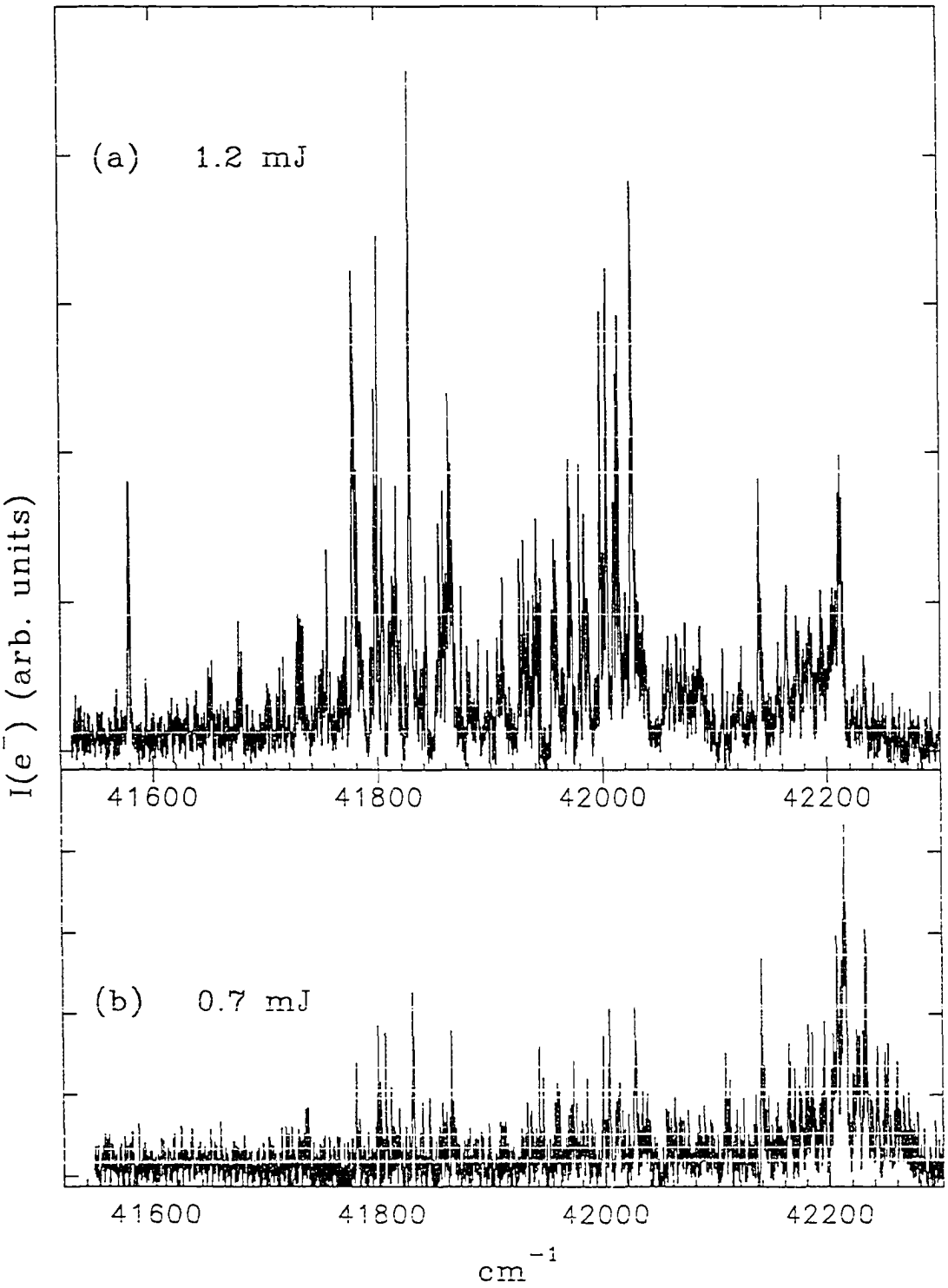
(a) 1.2 mJ
(b) 0.7 mJ
I(e⁻) (arb. units)
41600
41800
42000
42200
cm⁻¹

indicates that the prominent features in the region greater than $\approx$42,100 cm^{-1} are attributable to hot band ionization of H_2S.

The neutral SH($X^2\Pi$) ground state can be characterized by the Hund's case (a) coupling scheme.[45] This is justified because of the large spin-orbit splitting and the relatively low rotational state population (with the maximum rotational level $N'' \approx 10$) for SH($X^2\Pi$) formed in this experiment. The F_1 ($J'' = N'' + 1/2$) and F_2 ($J'' = N'' - 1/2$) levels refer to the $^2\Pi_{3/2}$ and $^2\Pi_{1/2}$ spin-orbit states of SH, respectively. The energy expression for the Hund's case (b) coupling is used to describe the $SH^+(X^3\Sigma^-)$ ionic ground state. The ionic rotational level labelled by N^+ represents the core angular momentum excluding electron spin. When the interaction with electron spin is taking into account, each rotational level splits into three spin-rotation fine structure components with the total angular momentum $J^+ = N^+ + 1$ (F_1^+ level), $J^+ = N^+$ (F_2^+ level), and $J^+ = N^+ - 1$ (F_3^+ level).

The π-valence molecular orbitals in the SH($X^2\Pi_i$) state are pure $3p_\pi$ atomic-like species.[48] The simultaneous absorption of two photons should favor the ejection of a p or an f electron within the sudden approximation. The electron angular momentum ℓ for an odd partial wave (p or f) has negative parity. Most of the peaks observed are assigned to the transitions with the angular momentum transfer $|\Delta J| \leq 7/2$ (see discussion below). Therefore, it is likely that the ionization process involves the emission of a p partial wave photoelectron. Nevertheless, this cannot exclude the possibility for the emission of an f partial wave photoelectron. McKoy and co-workers[49,50] have shown that the rescattering

of the photoelectron within the ion core is very important and can lead to a significant change in angular momentum of the final continuum channel. The rescattering could alter the primary odd ℓ electron into a partial wave channel of even ℓ.

Figure 7 shows a transition diagram for the N, O, P, Q, R, and S rotational branches from (N'', J'') levels of SH($X^2\Pi_{3/2}$). Each rotational level for SH($X^2\Pi_{3/2}$) is split into the positive parity (Π^+) and negative parity (Π^-) components. The average ratio Π^+/Π^- was found to be about one for SH formed at 193, 222, and 248 nm.[44] Based on this result, we estimated that the Π^+ and Π^- components of SH are produced with equal intensities by process (1) at 234-240 nm in this experiment. The small Λ-doubling cannot be resolved using our experimental energy resolution. The angular momentum selection rules for two-photon ionization of a diatomic molecule limit the allowed transitions to $\Delta J = J^+ - J'' = \ell + 5/2, \ldots, -\ell - 5/2$, where ℓ is the angular momentum for the photoelectron. If we assume that photoionization predominantly involves the ejection of an odd (p or f) ℓ partial wave photoelectron, we could associate the transition ending on $N^+ = 0, 2\ldots$ (even) states from the Π^+ state of SH and $N^+ = 1, 3\ldots$ (odd) from the Π^- state of SH.

The rotational branches (N, O, P, Q, R, S, and T) designate the changes in the core angular momentum apart from spin, $\Delta N (= N^+ - N'') = -3, -2, -1, 0, +1, +2$, and $+3$, respectively. The first and second subscripts attached to the rotational branches [see Figs. 4(a) and 5(a)] denote the F^+ (F_1^+, F_2^+, or F_3^+) levels for $SH^+(X^3\Sigma^-)$ and the F (F_1 or F_2) levels for SH($X^2\Pi_i$), respectively. For example, the $P_{21}(2)$ line represents the transition originating from the $N'' = 2$ and $J'' = 5/2$ (F_1 level) of the SH($X^2\Pi_{3/2}$) state and

Figure 7. Schematic diagram for the energy levels and symmetry labels for two-photon ionization transitions from the F_1 ($X^2\Pi_{3/2}$) manifold of SH to the F_1^+, F_2^+, and F_3^+ levels of $SH^+(X^3\Sigma^-)$. Typical transitions for the N, O, P, Q, R, and S branches are shown. The subscript i = 1 (F_1^+), 2 (F_2^+), and 3 (F_3^+).

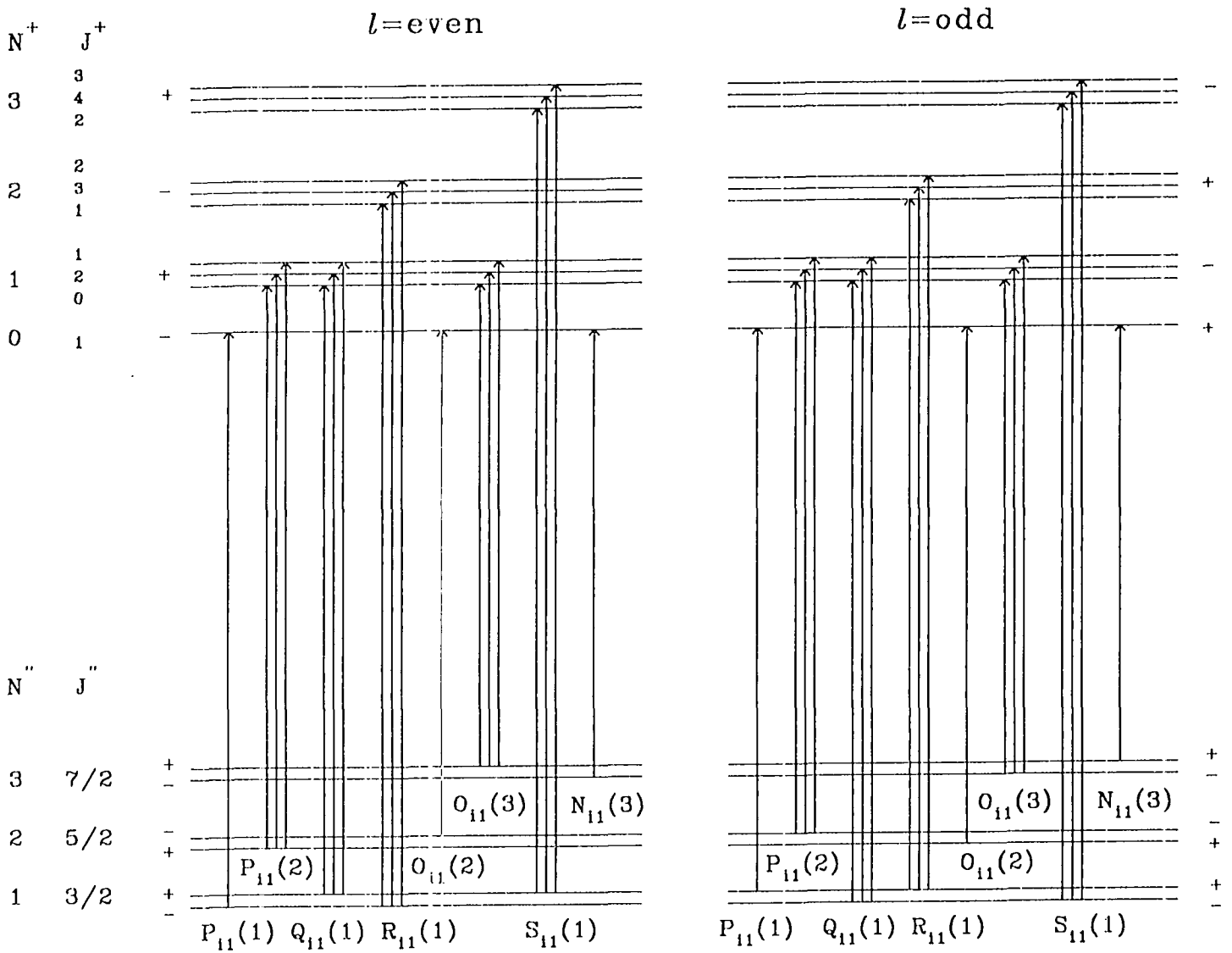
l=even
l=odd
N'
J'
3
7/2
2
5/2
1
3/2
N''
J''
3
4
2
2
3
1
1
2
0
1
0
P11(1)
Q11(1)
R11(1)
S11(1)
P11(2)
O11(2)
O11(3)
N11(3)

ending on the $N^+ = 1$ and $J^+ = 1$ (F_2^+ level) of the $SH^+(X^3\Sigma^-)$ state.

In order to understand the photoionization dynamics of SH, it is necessary to simulate the relative intensities for PE peaks observed in the spectra of Figs. 4(a) and 5(a). Xie and Zare[51] have derived electric-dipole-allowed photoionization selection rules for the interpretation of rotationally resolved PE spectra for diatomic molecules. However, the theoretical treatment for photoionization out of a valence $^2\Pi$ state [Hund's case (a)] has not yet been worked out in detail. We have attempted to simulate the experimental PE spectrum of SH semi-empirically by adjusting the relative intensities [r_B] for the rotational branches (B = N, O, P, Q, R, S, or T). For a given spin-orbit ($^2\Pi_{3/2}$ or $^2\Pi_{1/2}$) manifold, the relative PE peak intensities [$I_{PE}(B, J'')$] are calculated as,

$$I_{PE}(B, J'') = r_B [(2J'' + 1)/Q_{rot}] \exp(-\Delta E_{rot}/kT_r), \qquad (3)$$

where ΔE_{rot} is the rotational energy measured with respect to the energy for the lowest J'' level of the spin-orbit states [-170 cm^{-1} for $SH(X^2\Pi_{3/2})$ and +198 cm^{-1} for $SH(^2\Pi_{1/2})$] and Q_{rot} is the rotational partition function. We assume that the probabilities are identical for the ionization transitions from a specific Π^+ or Π^- state of SH to the F^+ (F_1^+, F_2^+, F_3^+) levels of a given N^+ ionic state. The probabilities for transitions from different J'' levels within a rotational branch are also assumed to be uniform. Based on the previous photodissociation study of Weiner et al.,[44] we have assumed that the rotational distribution for SH formed here by process (1) is characterized by a temperature of 300 K for both of the spin-orbit states. The calculated intensities are combined with a Gaussian line shape

with a full-width-at-half-maximum of 1 cm^{-1}. The rotational, fine structure, and centrifugal constants for SH^+ are taken from Horani et al.[52] (Ref. 53), and the rotational and centrifugal constants for SH are obtained from Ramsey[54] (Ref. 55). The transition frequencies calculated based on these constants agree with the experimental PE peak positions to within 2 cm^{-1}. Although the energy resolution is not sufficient to resolve the small Λ-doubling, many of the spin-rotation components for $SH^+(X^3\Sigma^-)$ are resolved in the spectra shown in Figs. 4(a) and 5(a). In the simulation, we found that the intensities for the S and T branches are small compared to the N, O, P, Q, and R branches. The simulated spectra shown in Figs. 4(b) and 5(b) are obtained using the relative rotational branch intensities, $r_N : r_O : r_P : r_Q : r_R$ = 0.19 : 0.23 : 0.37 : 0.14 : 0.07 and 0.32 : 0.36 : 0.11 : 0.16 : 0.05 for ionization from the $SH(X^2\Pi_{3/2})$ and $SH(^2\Pi_{1/2})$ states, respectively. The simulated spectra reproduce roughly the general profile of relative experimental peak intensities. The differences in detail between the simulated and experimental spectra can be attributed partly to local autoionization mechanisms. For example, the relative intensities of the two peaks observed at 84,057.5 cm^{-1} [$P_1(1)$] and 83,660.3 cm^{-1} [$O_{12}(2)$] are significantly stronger than those predicted by the simulated spectra. The strong intensities observed for the $P_1(1)$ and $O_{12}(2)$ lines may be due to near resonance autoionization processes. Furthermore, the characterization of the rotational distribution of SH produced by process (1) using an equilibrium rotational temperature is an crude assumption. The deviation of the actual rotational distribution of SH from the assumed equilibrium distribution will also limit the ability of Eq. (3) to reproduce the experimental PE spectrum of SH. We note that a PE peak at 41,770.6 cm^{-1} [Fig. 4(a)] coincides with

the expected $M_{12}(4)$ transition. Since no other structures can definitely be correlated with the M branch transitions, the existence of the M branch must be considered as uncertain.

Although the contributions for the S_{i2} and T_{i2} (i = 1-3) rotational branches are neglected in the simulation of the spectrum in the energy region lower than 42,100 cm^{-1}, we have marked (dashed lines) the positions of the these branches in Figs. 4(b) and 5(b) to illustrate the lack of correlations of the predicted and experimental PE peaks. The predicted positions of the S_{i1} and T_{i1} (i = 1-3) branches fall in the region greater than 42,080 cm^{-1} and are also marked (dashed lines) in Figs. 5(b). As pointed out above, the intensities of the major features [marked in asterisks in Fig. 5(a)], observed in this region increases significantly relative to PE peaks at lower energies as the laser pulsed energy is decreased, supporting the conclusion that these features are attributable to hot band ionization of H_2S. Due to the interference of these prominent PE features of H_2S, the analysis of the remaining minor PE features are difficult. It is possible that some of these weak PE structures are attributable to the S_{i1} and T_{i1} (i = 1-3) rotational branches. However, by comparing the intensities of PE peaks in this region and those in lower energies, we conclude that the S_{i1} and T_{i1} (i = 1-3) branches are weak with intensities lower than that of the R_{i1} (i = 1-3) branch. For this reason, we have not included the S_{i1} and T_{i1} (i = 1-3) branches in the simulation.

Based on the simulation shown in Figs. 4(b) and 5(b), we conclude that the intensities for the rotational branches with $\Delta N \leq 0$ are significantly stronger than those with $\Delta N > 0$. The rotational angular momentum transfer ΔN up to -3 is observed. Similar observations of enhanced intensities for $\Delta N \leq 0$ rotational branches have been

reported in the studies of NO (Refs. 11-13), OH (OD) (Ref. 14), N_2O (Ref. 16), and HCl (Refs. 15, 56). This phenomenon is rationalized by electric-field-induced rotational autoionization processes.[14] This propensity can be accounted for by the interaction of the high-n-Rydberg ($n > 150$) states close to a rotational ionization limit of the ion with the lower-n-Rydberg ($20 < n < 80$) states converging to a higher rotational ionization limit.[14] It is plausible that the application of the pulsed electric field ionizes the high-n-Rydberg molecules and simultaneously allows the isoenergetic low-n-Rydberg states to autoionize. Since the rotational spacing is smaller for lower N^+ levels than for higher N^+ levels, the density of available isoenergetic lower-n Rydberg states is greater for field-induced autoionization into lower N^+ levels. Furthermore, the optical excitation to lower-n Rydberg states converging to higher N^+ levels is limited by the relatively cold rotational distribution of SH. Because of the greater number of optically accessible lower-n Rydberg state converging to lower N^+ levels, field-induced rotational autoionization favors the $\Delta N \leq 0$ rotational branches.

Another possible mechanism involves a heterogeneous perturbation of the Rydberg state.[57] It is generally found that in heterogeneous interaction, the P branches for transitions to high-n-Rydberg states are enhanced and the corresponding R branches are weakened, while the opposite holds for transitions to the lower-n-Rydberg states. Since electrons are excited to the high-n-Rydberg states before the application of field ionization, the perturbation by the Rydberg state may favor the transition amplitude for the branches with $\Delta N \leq 0$ relative to those with $\Delta N > 0$.

After taking into account the Stark shift correction, the ionization energy IE for

$SH(X^2\Pi_{3/2})$ is 84,057.5±3 cm^{-1} (10.4219±0.0004 eV), as determined by the lowest possible ionization transition, i.e., the $P_1(1)$ line. This value favorably compares to a value of 10.43±0.03 eV obtained from the extrapolation of a short Rydberg series.[43]

Since the sampling of SH by PFI takes place in a collision free environment, knowing the photoionization oscillator strengths would have allowed the estimation of the nascent SH product state distribution. Although the oscillator strengths for photoionization transitions of interest to the present experiment are unknown, preventing a detailed simulation of the PE spectrum for SH, we may conclude from the semi-empirical analysis that SH radicals are produced in both the $X^2\Pi_{3/2}$ and $^2\Pi_{1/2}$ states by process (1), and that the rotational distributions of SH in these two spin-orbit states can be characterized by a rotational temperature of ≈300 K, in accordance with previous observations.

CONCLUSION

Using the N2P-PFI scheme, we have obtained the threshold PE spectra for SH at high resolution. The assignment of the rotationally-resolved N2P-PFI-PE spectrum allows highly accurate determination of the IE for SH. A propensity favoring the rotational branches with $\Delta N \leq 0$ is observed for SH. Pulsed field ionization PE detection can be a sensitive and quantitative means for probing the nascent state distribution of photoproducts when the oscillator strengths for photoionization are known. We hope that this study will stimulate a detailed theoretical interpretation of the observed PE spectrum for SH.

REFERENCES

(1) J. W. Rabalais, "Principles of Ultraviolet Photoelectron Spectroscopy" (Wiley, New York, 1977).

(2) G Reiser, W. Habenicht, K. Müller-Dethlefs, and E. W. Schlag, *Chem. Phys. Lett.* 152, 119 (1988).

(3) K. Müller-Dethlefs, M. Sander, and E. W. Schlag, Z. *Naturforsch.* A 39, 1089 (1984).

(4) K. Müller-Dethlefs and E. W. Schlag, *Annu. Rev, Phys. Chem.* 42, 109 (1991).

(5) R. G. Tonkyn, J. W. Winniczek, and M. G. White, *Chem. Phys. Lett.* 164, 137 (1989).

(6) M. Braunstein, V. McKoy, S. N. Dixit, R. G. Tonkyn, and M. G. White, *J. Chem. Phys.* 93, 5345 (1990).

(7) W. Kong, D. Rogers, and J. W. Hepburn, *Chem. Phys. Lett.* 203, 497 (1993).

(8) W. Kong, D. Rogers, J. W. Hepburn, K. Wang, and V. McKoy, *J. Chem. Phys.* 99, 3159 (1993).

(9) R. T. Wiedmann, M. G. White, K. Wang, and V. Mckoy, *J. Chem. Phys.* 98, 7673 (1993).

(10) K. Müller-Dethefs, M. Sander, and E. W. Schlag, *Chem Phys. Lett.* 112, 291 (1984).

(11) G. Reiser and K. Müller-Dethelefs, *J. Phys. Chem.* 96, 9 (1992).

(12) M. Sander, L. A. Chewter, K. Müller-Dethefs, and E. W. Schlag, *Phys. Rev.* A

36, 4543 (1987).

(13) A. Stribel, I. Fischer, J. Staecker, G. Niedner-Schatteburg, K. Müller-Dethlefs and C. E. Bondybey, *J. Chem. Phys.* 97, 2332 (1992).

(14) R. T. Wiedmann, R. G. Tonkyn, M. G. White, K. Wang, and V. McKoy, *J. Chem. Phys.* 97, 768 (1992).

(15) R. G. Tonkyn, R. T. Wiedmann, and M. G. White, *J. Chem. Phys.* 96, 3696 (1992).

(16) R. T. Wiedmann,E. R. Grant, R. G. Tonkyn, and M. G. White, *J. Chem. Phys.* 95, 746 (1991).

(17) R. G. Tonkyn, R. Wiedemann, E. R. Grant, and M. G. White, *J. Chem. Phys.* 95, 7033 (1991).

(18) M.-T. Lee, K. Wang, V. McKoy, R. G. Tonykn, R. T. Wiedmann, E. R. Grant, and M. G. White, *J. Chem. Phys.* 96, 7848 (1992).

(19) R. T. Wiedmann and M. G. White, "Optical Methods for Time- and State-Resolved Chemistry", C. Y. Ng, Ed., *SPIE Proc.* 1638 (1992), p. 273.

(20) I. Fischer, A. Lochschmidt, A. Strobel, G. Niedner-Schatteburg, K. Müller-Dethlefs, and V. E. Bondybey, *J. Chem. Phys.* 98, 3592 (1993).

(21) J. A. Blush, P. Chen, R. T. Wiedman, and M. G. White, *J. Chem. Phys.* 98, 3557 (1993).

(22) I. Fischer, A. Lochschmidt, A. Strobel, G. Niedner-Schatteburg, K. Müller-Dethelef, and V. E. Bondybey, *Chem. Phys. Lett.* 202, 542 (1993).

(23) S. T. Pratt, P. M. Dehmer, and J. L. Dehmer, *J. Chem. Phys.* 99, 6233 (1933).

(24) A, Strobel, A. Lochschmidt, I. Fisher, G. Niedner-Schatteburg, and V. E. Bondybey, *J. Chem. Phys.* 99, 733 (1993).

(25) W. Habenicht, G. Reiser, and K. Müller-Dethlefs, *J. Chem. Phys.* 95, 4809 (1991).

(26) G. Reiser, W. Habenicht, and K. Müller-Dethlefs, *J. Chem. Phys.* 98, 8462 (1993).

(27) L. A. Chewter, M. Sander, K. Müller-Dethefs, and E. W. Schlag, *J. Chem. Phys.* 86, 4737 (1987).

(28) G. C. Eiden, F. Weinhold, and J. C. Weisshaar, *J. Chem. Phys.* 95, 8665 (1991).

(29) I. Fischer, A. Strobel, J. Staecher, G. Niedner-Schatteburg, K. Müller-Dethlefs, and V. E. Bondybey, *J. Chem. Phys.* 96, 7171 (1992).

(30) K. Norwood, S Nourbakhsh, G.-Z. He, and C. Y. Ng, *Chem. Phys. Lett.* 184, 147 (1991).

(31) S. Nourbakhsh, K. Norwood, G.-Z. He, and C. Y. Ng, *J. Am. Chem. Phys.* 113, 6311 (1991).

(32) S. Nourbakhsh, K. Norwood, H-M. Yin, C.-L. Liao, and C. Y. Ng, *J. Chem. Phys.* 95, 946 (1991).

(33) S. Nourbakhsh, C.-L. Liao, and C. Y. Ng, *J. Chem. Phys.* 92, 6587-93 (1990).

(34) S. Nourbakhsh, K. Norwood, H.-M. Yin, C.-L. Liao, and C. Y. Ng, *J. Chem. Phys.* **95**, 5014-5023 (1991).

(35) Z.-X. Ma, C.-L. Liao, H.-M. Yin, C. Y. Ng, S.-W. Chiu, I. Ma, and W.-K. Li, . *Chem. Phys. Lett.* 213, 250 (1993).

(36) W.-K. Li, S.-W. Chiu, and C. Y. Ng, *J. Chem. Phys.* 99, 8440 (1993).

(37) N. L. Ma, W.-K. Li, and C. Y. Ng, *J. Chem. Phys.* 99, 6470 (1993).

(38) C.-W. Hsu, C.-L. Liao, Z.-X, Ma, P. J. H. Tjossem, and C. Y. Ng, *Chem. Phys. Lett.* 199, 78 (1992).

(39) C. W. Hsu, C.-L. Liao, Z.-X. Ma, P.J. H. Tjossem, and C. Y. Ng, *J. Chem. Phys.* 97, 6283 (1992).

(40) C. E. Moore, "Atomic Energy Levels", *Natl. Bur. Stand. (U.S.)* Circ. No. 467 (U.S. GPO, Washington, D.C. 1949), Vol. I.

(41) The N2P-PFI-PE signal for SH is found to be maximized at a delayed time of 650 μs. We found that the N2P-PFI-PE spectrum for H_2S obtained at a delay of 450 μs has the highest resolution and corresponds to the lowest H_2S rotational temperature.

(42) J. Berkowitz, private communication.

(43) B. A. Morrow, *J. Phys.* 44, 2447 (1966).

(44) B. R. Weiner, H. B. Levene, J. J. Valentini, and A. P. Baronavski, *J. Chem. Phys.* 90, 1403 (1989).

(45) G. Herzberg, "Molecular Spectra and Molecular Structure, Vol.1: Spectra of Diatomic Molecules" (van Nostrand Reinhold, New York, 1950).

(46) R. E. Continetti, B. A. Balko, and Y. T. Lee, *Chem. Phys. Lett.* 182, 400 (1991); and references therein.

(47) W. A. Chupka, *J. Chem. Phys.* 98, 4520 (1993).

(48) P. J. Bruna and G. Hirsch, *Mol. Phys.* 61, 1359 (1987).

(49) H. Rudolph, V. McKoy, and S. N. Dixit, *J. Chem. Phys.* 90, 2570 (1989).

(50) K. Wang and V. McKoy, *J. Chem. Phys.* 95, 8718 (1991).

(51) J.-C. Xie and R. N. Zare, *J. Chem. Phys.* 93, 3033 (1990).

(52) M. Horani, S. Leach, and J. Rostas, *J. Mol. Spect.* 23, 115 (1967).

(53) The rotational constant B = 9.134 cm^{-1}, the spin splitting constants λ = 5.71 cm^{-1} and γ = -0.165 cm^{-1}, and the centrifugal constant D = 0.000489 cm^{-1}. The energies for the F^+ levels are: $F_1^+(N^+) = BN^+(N^+ + 1) + (2N^+ + 3)B - \lambda - [(2N^+ + 3)^2B^2 + \lambda^2 - 2\lambda B]^{1/2} + \gamma(N^+ + 1) - D[N^+(N^+ + 1)]^2$; $F_2^+(N^+) = BN^+(N^+ + 1) - D[N^+(N^+ + 1)]^2$; and $F_3^+(N^+) = BN^+(N^+ + 1) - (2N^+ - 1)B - \lambda + [(2N^+ - 1)^2B^2 + \lambda^2 - 2\lambda B]^{1/2} - \gamma N^+ - D[N^+(N^+ + 1)]^2$. See Ref. 45.

(54) D. A. Ramsey, *J. Chem. Phys.* 20, 1920 (1952).

(55) The rotational constant B = 9.461 cm^{-1} and the centrifugal constant D = 0.00048 cm^{-1}. The energies for F (F_1 and F_2) levels are: $F_1(J'') = B\{(J'' + 1/2)^2 - \Lambda^2 - (1/2)[4(J'' + 1/2)^2 + Y(Y - 4)\Lambda^2]^{1/2}\} - DJ''^4$ and $F_2(J'') = B\{(J'' + 1/2)^2 - \Lambda^2 + (1/2)[4(J'' + 1/2)^2 + Y(Y - 4)\Lambda^2]^{1/2}\} - D(J'' + 1)^4$. Here, Λ = 1 for a Π state and Y = A_e/B, where A_e (-376.96 cm^{-1}) is the spin-orbit splitting. See Ref. 45.

(56) K. S. Haber, Y. Jiang, G. P. Bryant, E. R. Grant, and H. Lefebvre-Brion, *Phys. Rev.* A 44, 5331 (1991).

(57) C. Jungen, *J. Chem. Phys.* 53, 4168 (1970).

PAPER 5.

NONRESONANT TWO-PHOTON PULSED FIELD IONIZATION OF CH_3S FORMED IN PHOTODISSOCIATION OF CH_3SH AND CH_3SSCH_3

ABSTRACT

Threshold photoelectron (PE) spectra for CH_3S formed in the photodissociation of CH_3SH and CH_3SSCH_3 in the photon energy range of 36,850-38,150 cm^{-1} have been measured using the nonresonant two-photon pulsed field ionization (N2P-PFI) technique. Both spin-orbit states $CH_3S(\tilde{X}^2E_{3/2})$ and $CH_3S(^2E_{1/2})$ are observed from CH_3SH and CH_3SSCH_3 in this photodissociation energy range. However, negligible intensities of vibrationally excited CH_3S radicals are produced from CH_3SH. In the case of CH_3S from CH_3SSCH_3, the population ratio $CH_3S(\nu_3 = 1)/CH_3S(\nu_3 = 0)$ is estimated to be ≈ 0.18. The simulation of the N2P-PFI-PE spectra reveals that the rotational temperature for $CH_3S(\tilde{X}^2E_{3/2,1/2})$ formed by photodissociation of CH_3SH is $\approx$200-250 K and the branching ratio $CH_3S(^2E_{1/2})/CH_3S(\tilde{X}^2E_{3/2})$ is 0.5 $\pm$ 0.1. For $CH_3S(\tilde{X}^2E_{3/2,1/2})$ produced from CH_3SSCH_3, the rotational temperature for $CH_3S(\tilde{X}^2E_{3/2,1/2})$ is $\approx$800-900 K and the branching ratio $CH_3S(^2E_{1/2})/CH_3S(\tilde{X}^2E_{3/2})$ is 1.1 $\pm$ 0.2. This experiment demonstrates that the PFI-PE spectroscopic method can be a sensitive probe for nascent rovibronic state distributions of photoproducts. Furthermore, the simulation also shows that the photoionization dynamics of CH_3S may involve rotational angular momentum changes up to $\pm$ 4. The ionization energy and C-S stretching frequency for $CH_3S^+(\tilde{X}^3A_2)$ are determined to be 74,726 $\pm$ 8 cm^{-1} (9.2649 $\pm$ 0.0010 eV) and 733 $\pm$ 5 cm^{-1}, respectively. The spin-orbit splitting for $CH_3S(\tilde{X}^2E_{3/2,1/2})$ is 257 $\pm$ 5 cm^{-1}, in agreement with the literature values.

INTRODUCTION

Photoelectron (PE) spectroscopy performed at a sufficiently high resolution provides quantitative information of the rovibronic populations of the molecular species under investigation. With the recent development of the pulsed field ionization (PFI) technique,[1] a version of the zero-kinetic-energy (ZEKE) PE technique,[2,3] the attainable resolution of PE spectroscopy has approached that of optical spectroscopy. The possibility of PFI-PE as an alternative for the laser-induced fluorescence (LIF) technique to probe nascent product rovibronic state distributions has become a reality.[4]

In a series of recent investigations,[5-9] Bondybey and co-workers have demonstrated that PFI-PE spectra for molecular species can be obtained with good sensitivity by using the one-color nonresonant two-photon (N2P) excitation. In many cases, the N2P-PFI-PE spectra are surprisingly similar to those acquired by the single vacuum ultraviolet (VUV) photon ionization scheme.[6] The N2P-PFI scheme is very attractive because of its high sensitivity and the availability of commercial pulsed dye lasers with an output range of 200-400 nm, as required for the ionization of most polyatomic species at their thresholds.

We have recently succeeded in employing the N2P-PFI-PE technique for studying SH radicals produced in the photodissociation of H_2S.[4] The rotationally-resolved N2P-PFI-PE spectrum for SH provides estimates for the nascent rotational population of SH and the branching ratio for $SH(X^2\Pi_{3/2})/SH(^2\Pi_{1/2})$. Highly accurate ionization energies (IE) for $SH(X^2\Pi_{3/2,1/2})$ have been determined by simulation of the N2P-PFI-PE spectrum of SH. We have extended the one-color N2P-PFI-PE technique to include the investigation of

polyatomic radicals.[10]

Here we present the results and analysis of the N2P-PFI-PE spectra of CH_3S formed in the photodissociation of CH_3SH [process (1)] and CH_3SSCH_3 [process (2)]. In this experiment, a one-color three-photon process is involved. That is, the CH_3S radicals are first prepared by the single-photon dissociation process in the wavelength range of 262-271 nm.

$$CH_3SH + h\nu \rightarrow CH_3S(\tilde{X}^2E_{3/2,1/2}) + H \qquad (1)$$

$$CH_3SSCH_3 + h\nu \rightarrow 2\ CH_3S(\tilde{X}^2E_{3/2,1/2}) \qquad (2)$$

The subsequent ionization of CH_3S is accomplished by N2P excitations of CH_3S to high-n Rydberg states [$CH_3S^*(n)$], followed by PFI of $CH_3S^*(n)$.

$$CH_3S(\tilde{X}^2E_{3/2,1/2}) + 2h\nu \rightarrow CH_3S^*(n) \rightarrow CH_3S^+(\tilde{X}^3A_2) + e^- \qquad (3)$$

The two additional photons absorbed by CH_3S in process (3) are furnished by the same laser pulse which induced the dissociation of CH_3SH in process (1) or CH_3SSCH_3 in process (2). In addition to providing information on the spin-orbit and rovibronic state distributions of processes (1) and (2), the simulation of the observed N2P-PFI-PE spectra of $CH_3S(\tilde{X}^2E_{3/2,1/2})$ obtained in this experiment also yields a highly accurate value for the IE of $CH_3S(\tilde{X}^2E_{3/2})$ and the rotational constants for $CH_3S^+(\tilde{X}^3A_2)$.

The photodissociation of CH_3SH and CH_3SSCH_3 at higher photon energies (193 and 248 nm) have been the subject of several recent experimental[11-15] and theoretical[16-20] investigations. For CH_3SH, the experiments indicate that process (1) is favored at lower photon energies, whereas the cleavage of the H_3C-SH bond becomes more important at shorter wavelengths. The role of conical intersections in the photodissociation of CH_3SH has been the subject of a recent theoretical study by Yarkony.[20] The studies of CH_3SSCH_3 indicate that CH_3S is the predominant product at 248 nm,[15] whereas both CH_3SS and CH_3S are produced at 193nm, with CH_3SS being the predominant photoproduct.[12,15] Since the photodissociation wavelength range of interest here is 262-271 nm, processes (1) and (2) are expected to be the predominant channels for the respective photodissociations of CH_3SH and CH_3SSCH_3.

Two recent VUV photoionization mass spectrometric studies of CH_3S have been reported.[21,22] The IE values for $CH_3S(\tilde{X}^2E_{3/2,1/2})$ determined in this study are significantly more accurate than those obtained in the previous VUV photoionization mass spectrometric experiments. The present N2P-PFI-PE study also provides an accurate measure for the C-S stretching (ν_3^+) vibrational frequency for $CH_3S^+(\tilde{X}^3A_2)$.

EXPERIMENTAL

The experimental apparatus used in this study has been described in detail.[4] Briefly, it is modified from the laser ionization time-of-flight (TOF) mass spectrometer used in previous photodissociation studies.[23,24] A two-stage microchannel plate detector and a set of simple aperture lenses have been added for PE detection below the photoionization region and opposite to the ion TOF tube.

For this experiment, CH_3SH (99.5% pure) and CH_3SSCH_3 (99% pure) are obtained from Aldrich and are used without further purification. The CH_3SH (8%) or CH_3SSCH_3 (vapor pressure $\approx$ 40 Torr at 298 K) sample is seeded in Ar carrier gas to a total stagnation pressure of $\approx$ 2.5 bar or $\approx$1.3 bar, respectively. The gas mixture is introduced into the photoionization region by supersonic expansion through a pulsed valve with a nozzle diameter of 0.5 mm. The molecular beam is skimmed by a conical skimmer (1 mm in diameter, 3.8 cm from the nozzle) before intersecting with a tunable laser beam (90°, 8.3 cm down stream from the skimmer). Both the pulsed valve and the dye laser are operated at a repetition rate of 13 Hz.

The molecular beam source chamber is pumped by a freon-trapped, 6 in. diffusion pump (pumping speed $\approx$ 2,000 ℓ/s), while the photoionization chamber and the ion-TOF tube are evacuated by two 50 ℓ/s turbomolecular pumps. During the experiment, the beam source chamber and the photoionization chamber are maintained at pressures of about $1x10^{-4}$ and $2x10^{-6}$ Torr, respectively.

The second harmonic output of an excimer (Lambda Physik EMG 201 MSC)

pumped-dye laser (Lambda Physik FL 3002) is focused into the photoionization region by a 200 mm focal length fused-silica lens. Coumarin 153 dye is used to produce the fundamental output in the 524-542 nm region. Typical laser pulse energies used in the second harmonic output range of 262-271 nm are 1.2 mJ, as monitored with a pyroelectric detector. The wavelength calibration uses the known resonance-enhanced multiphoton ionization spectrum of atomic sulfur,[25] which is produced by the multiphoton laser photodissociation of CH_3SH and CH_3SSCH_3.

Ion detection using the ion TOF mass spectrometer has been described in detail previously.[23,24] Here, a constant electric field of 280 V/cm is used to extract the ions formed in the photoionization region. Since the N2P ionization processes compete with many multiphoton ionization and fragmentation channels, it is necessary to optimize the CH_3S^+ ion signal by varying the dye laser power.

The ZEKE/PFI detection scheme relies on delayed PFI of long-lived high-n Rydberg states populated by laser excitation at a few wavenumbers below the ionization threshold. In this experiment, the firing of the photodissociation and excitation laser is delayed by 750 μs with respect to the triggering pulse for opening the pulsed valve. A 1 μs pulsed field of 3.1 V/cm is applied to the repeller plate 3 μs after firing the dye laser. The pulsed field field-ionizes the molecular species in high-n Rydberg states as well as extracts the electrons thus formed to the microchannel plate electron detector. The firing sequence of the pulsed valve, dye laser, and pulsed electric field is controlled by two digital delay units (Stanford Research DG535). The electron signal from the electron detector and the laser energy signal from the pyroelectric detector are fed into two

identical boxcar integrators (Stanford Research SR250), which are interfaced to an IBM/AT computer. The electron and laser energy signals are averaged for 30 shots at each laser wavelength.

The bandwidth of the dye laser is 0.2 cm^{-1} for the fundamental and ≈ 0.4 cm^{-1} for the second harmonic outputs. For a two-photon ionization process, the resolution due to the ionization laser is expected to be ≈ 0.8 cm^{-1}. We have reproduced the N2P-PFI-PE spectrum for H_2S reported previously.[4,6] This spectrum suggests that the PE energy resolution achieved in this experiment is similar to that obtained by Bondybey and co-workers[6] using the same value of ionization pulsed field.

RESULTS

A. CH_3S from CH_3SH

Figure 1(a) shows the N2P-PFI-PE spectrum in the region of 36,850-38,060 cm^{-1} for nascent $CH_3S(\tilde{X}^2E_{3/2,1/2})$ radicals formed by process (1). This spectrum is the average of four independent and reproducible scans. The pulsed field of 3.1 V/cm used in this measurement corresponds to a Stark shift of 5.3 cm^{-1}. We note that PE signals at photon energies > 37,810 cm^{-1} are mostly due to the ionization of CH_3SH, the IE of which is 76,302 cm^{-1} (2x38,151 cm^{-1}).[10] The N2P ion spectrum for CH_3S measured in the region of 36,900-37,460 cm^{-1} is depicted in Fig. 1(b) for comparison with the PFI-PE spectrum. Since the ionization of CH_3S from CH_3SH is the result of a three photon process, the PE and CH_3S^+ ion signals of Figs. 1(a) and 1(b) have been normalized by the cube of the laser pulse energy.

B. CH_3S from CH_3SSCH_3

The N2P-PFI-PE spectrum in the region of 36,850-38,150 cm^{-1} for CH_3S formed by the photodissociation of CH_3SSCH_3 [process (2)] is shown in Fig 2(a). This PFI-PE spectrum of CH_3S is the average of three independent and reproducible scans. The corresponding N2P ion spectrum in the region of 36,900-37,520 cm^{-1} for CH_3S is depicted in Fig. 2(b). Similar to the spectra shown in Figs. 1(a) and 1(b), the PE and CH_3S^+ ion signals of Figs. 2(a) and 2(b) have been normalized by the cube of the laser pulse energy.

Figure 1 (a) The N2P-PFI-PE spectrum in the region of 36,850-38,150 cm^{-1} for nascent $CH_3S(\tilde{X}^2E_{3/2,1/2})$ radicals formed by process (1). This spectrum is the average of four independent scans. A pulsed field of 3.1 V/cm was used in this measurement. The PE signals [$I(e^-)$] have been normalized with the cube of the laser pulse energy. Note that the PFI-PE signals at photon energies > 37,810 cm^{-1} are due to ionization of CH_3SH. The dip marked by ▼ is caused by the resonance-enhanced multiphoton ionization of S atoms. See the text.

(b) The N2P ion spectrum for CH_3S^+ from CH_3SH in the region of 36,900-37,460 cm^{-1}. The CH_3S^+ ion signals have been normalized with the cube of the laser pulse energy.

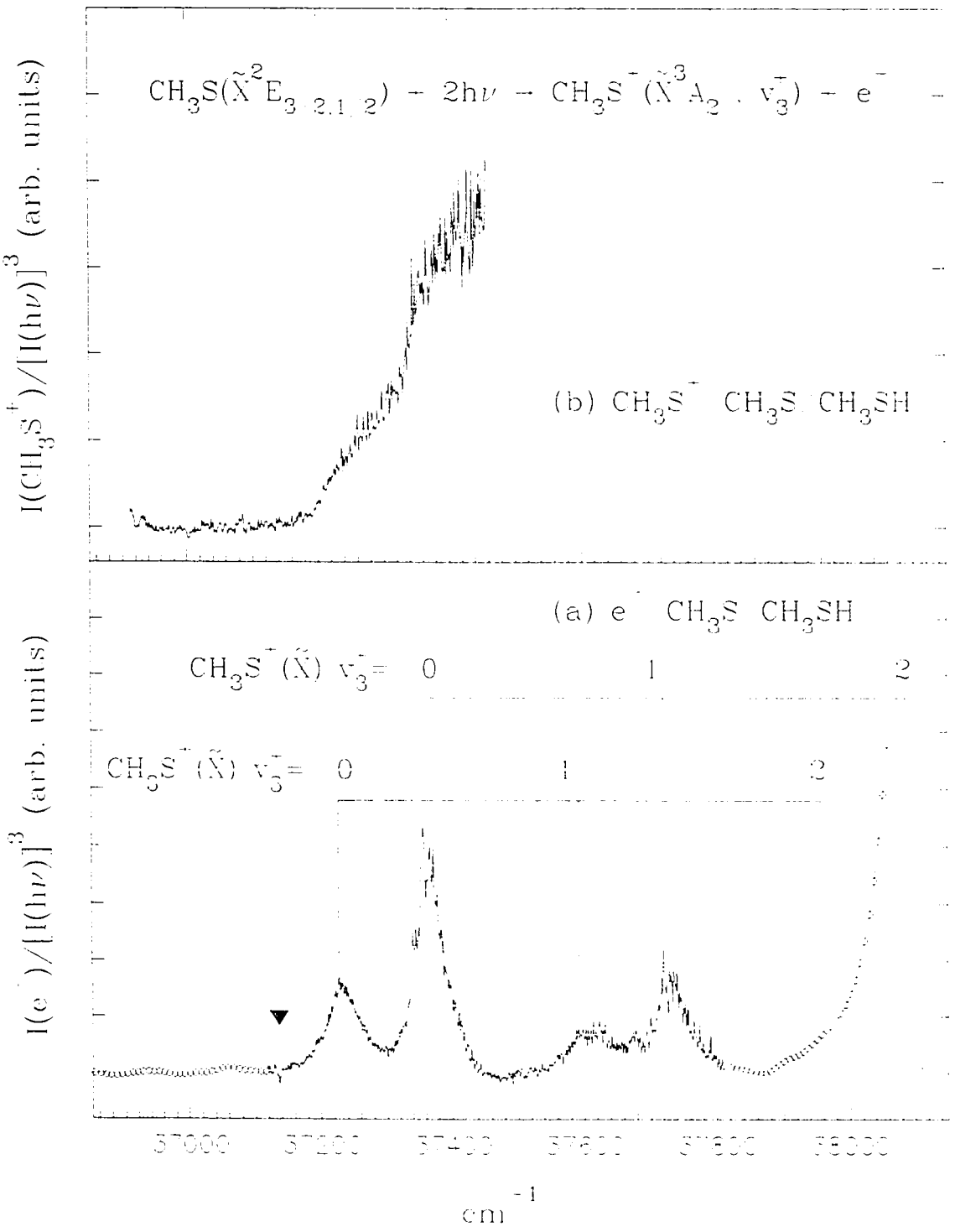
$CH_3S(\tilde{X}^2E_{3/2,1/2}) + 2h\nu \rightarrow CH_3S^+(\tilde{X}^3A_2, v_3^+) + e^-$
(b) CH_3S^+ CH_3S CH_3SH
(a) e^- CH_3S CH_3SH
$CH_3S^+(\tilde{X})$ v_3^+= 0 1 2
$CH_3S^+(\tilde{X})$ v_3^+= 0 1 2
$I(CH_3S^+)/[I(h\nu)]^3$ (arb. units)
$I(e^-)/[I(h\nu)]^3$ (arb. units)
37000 37200 37400 37600 37800 38000
cm^{-1}

Figure 2 (a) The N2P-PFI-PE spectrum in the region of 36,850-38,150 cm^{-1} for nascent $CH_3S(\tilde{X}^2E_{3/2,1/2})$ radicals formed by process (2). This spectrum is the average of three independent scans. A pulsed field of 3.1 V/cm was used in the measurement. The PE signals [$I(e^-)$] have been normalized with the cube of the laser pulse energy. The hot PE band attributable to the ionization of $CH_3S(\tilde{X}, \nu_3=1)$ is marked by an arrow.
(b) The N2P ion spectrum for CH_3S^+ from CH_3SSCH_3 in the region of 36,900-37,520 cm^{-1}. The CH_3S^+ ion signals have been normalized with the cube of the laser pulse energy. The dips marked by ▼ in Figs. 2(a) and 2(b) are caused by the resonance-enhanced multiphoton ionization of S atoms.

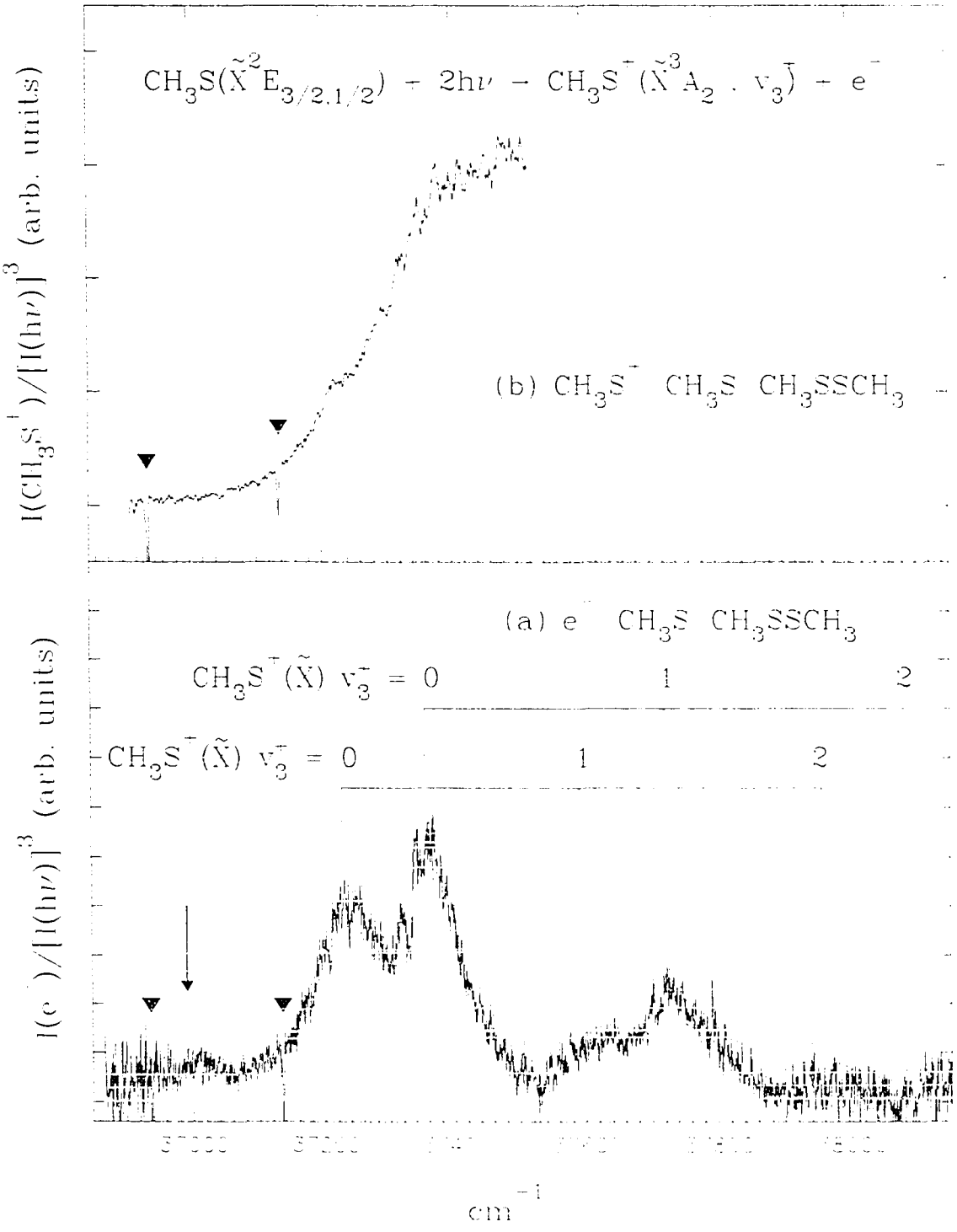
$CH_3S(\tilde{X}^2E_{3/2,1/2}) + 2h\nu \rightarrow CH_3S^+(\tilde{X}^3A_2, v_3^+) + e^-$
(b) CH_3S^+ CH_3S CH_3SSCH_3
$I(CH_3S^+)/[I(h\nu)]^3$ (arb. units)
(a) e^- CH_3S CH_3SSCH_3
$CH_3S^+(\tilde{X})$ $v_3^+ = 0$ 1 2
$CH_3S^+(\tilde{X})$ $v_3^+ = 0$ 1 2
$I(e^-)/[I(h\nu)]^3$ (arb. units)
cm^{-1}

DISCUSSION

Two resolved peaks centered at 74,459 and 74,716 cm^{-1} (2x37,229.5 and 2x37,358 cm^{-1}) are observed in the PFI-PE spectrum of Fig. 1(a). These structures correlate well with the two step-like features observed in the N2P CH_3S^+ ion spectrum shown in Fig. 1(b). The spacing between these two peaks is 257 ± 5 cm^{-1}, which is in excellent agreement with the spin-orbit splitting of 255.5 and 259.1 cm^{-1} determined in previous laser induced fluorescence studies.[26,27] Based on this observation, we assign the peaks centered at 74,459 and 74,716 cm^{-1} to ionization transitions, $CH_3S(^2E_{1/2}) \rightarrow CH_3S^+(\tilde{X}^3A_2, \nu_3^+=0)$ and $CH_3S(\tilde{X}^2E_{3/2}) \rightarrow CH_3S^+(\tilde{X}^3A_2, \nu_3^+=0)$, respectively. The widths for these PE bands are similar and have a value of ≈ 50 cm^{-1} for the full-width-at-half-maximum (FWHM). The profiles of these PE bands are mostly determined by the rotational populations of $CH_3S(\tilde{X}^2E_{3/2,1/2})$. The rotational populations of the precursor CH_3SH molecules may also have a finite contribution to the observed widths of these PE bands.

Two weaker PE bands observed at 75,189 and 75,446 cm^{-1} (2x37,594.5 and 2x37,723 cm^{-1}), have structures and relative intensities similar to the two strong PE bands at 74,459 and 74,716 cm^{-1}. The *ab initio* calculations[16] indicate that the equilibrium geometries for CH_3S and CH_3S^+ are similar. A noticeable difference is that the C-S bond distance in CH_3S^+ is shorter than that in CH_3S by 0.04 Å, suggesting that the ν_3^+ mode of CH_3S^+ may be excited in the ionization transition. For this reason, we assign the PE bands at 75,189 and 75,446 cm^{-1} to ionization transitions, $CH_3S(^2E_{1/2}) \rightarrow CH_3S^+(\tilde{X}^3A_2, \nu_3^+=1)$ and $CH_3S(\tilde{X}^2E_{3/2}) \rightarrow CH_3S^+(\tilde{X}^3A_2, \nu_3^+=1)$, respectively.

The bond dissociation energy for CH_3S-H is in the range of 86-90 kcal/mol^{-1}.[12,14,22] Thus, for a photodissociation energy of 37,300 cm^{-1} (107 kcal/mol), the available energy (E_{av}) for process (1) is $\approx$19 kcal/mol. Energetically, it is possible that the formation of CH_3S from CH_3SH results in the excited ν_3 mode of CH_3S, the vibrational quantum of which is 727$\pm$3 cm^{-1}.[27] As shown in the PFI-PE and N2P ion spectra of Figs. 1(a) and 1(b), negligible signals are found below 37,160 cm^{-1}, indicating that the formation of vibrationally excited CH_3S radicals is not important in this energy range. At higher photodissociation energies, previous experiments show that the formation of CH_3S in excited vibrational states by process (1) is possible.[12-14] The photodissociation study of CH_3SH at 248 nm (40,323 cm^{-1}) indicates that CH_3S radicals may be produced in vibrationally excited states with a C-S stretching vibrational progression that extends to ν_3 = 2, while ν_3 levels up to 17 are observed at 193 nm (51,813 cm^{-1}).[14]

Four PFI-PE bands in positions similar to those resolved in Fig. 1(a) are observed in the N2P-PFI-PE spectrum for CH_3S from CH_3SSCH_3 [Fig. 2(a)]. It is thus logical to conclude that $CH_3S(\tilde{X}^2E_{3/2,1/2})$ radicals are also produced by process (2), and that their ionization produces $CH_3S^+(\tilde{X}^3A_2,\ \nu_3^+=0,1)$. The broader PE bands observed for $CH_3S(\tilde{X}^2E_{3/2,1/2})$ from CH_3SSCH_3 are consistent with the conclusion that $CH_3S(\tilde{X}^2E_{3/2,1/2})$ radicals formed in process (2) are rotationally hotter than those produced in process (1). The CH_3S radicals produced from CH_3SSCH_3 are expected to be internally hotter than those produced from CH_3SH, partly because of the weaker S-S bond energy. That is, at the same photodissociation energy, process (2) is more exothermic than process (1). As described below, the simple impulsive dissociation model predicts that the CH_3S fragments

from CH_3SSCH_3 are rotationally excited to a greater extent than those from CH_3SH.

A careful examination of the PFI-PE spectrum of CH_3S from CH_3SSCH_3 reveals a small PE band at 73,987 cm^{-1} [marked by an arrow in Fig. 2(a)], which is about 729 cm^{-1} below the main PE bands observed at 74,716 cm^{-1}. Since the spacing between these bands is comparable to the literature value[27] of 727 $\pm$ 3 cm^{-1} for the ν_3 mode of $CH_3S(\tilde{X}^2E_{3/2})$, we assign the small peak at 73,987 to be a hot PE band due to ionization of $CH_3S(\tilde{X}^2E_{3/2}, \nu_3=1)$. Comparing the intensities of these bands, we estimate that the population ratio $CH_3S(\tilde{X}^2E_{3/2}, \nu_3=1)/CH_3S(\tilde{X}^2E_{3/2}, \nu_3=0)$ is about 0.18.

The more gradual rise at the ionization threshold of the CH_3S^+ ion spectrum of Fig. 2(b) compared to that depicted in Fig. 1(b) is also consistent with the higher rotational temperature (T_r)[28] for CH_3S and the formation of $CH_3S(\tilde{X}, \nu_3=1)$ from process (2). Because of the higher T_r for CH_3S from CH_3SSCH_3, the step-like feature corresponding to the onset for the ionization transition $CH_3S(^2E_{1/2}) \rightarrow CH_3S^+(\tilde{X}^3A_2)$, which is resolved in the spectrum of Fig. 1(b), is not discernible in Fig. 2(b).

In order to gain insight into the photoionization dynamics, and to determine the IE and spectroscopic constants for $CH_3S^+(\tilde{X}^3A_2)$, it is necessary to simulate the observed N2P-PFI-PE spectra for $CH_3S(\tilde{X}^2E_{3/2,1/2})$. Since the equilibrium geometry for CH_3S in its ground state is predicted to be distorted only slightly from the C_{3v} symmetry by the Jahn-Teller effect.[16] we assume C_{3v} structures for both $CH_3S(\tilde{X}^2E_{3/2,1/2})$ and $CH_3S^+(\tilde{X}^3A_2)$. That is, the rotational spectrum for CH_3S is treated as a symmetric top case in the simulation. The nuclear spin statistical weights for the *a* and *e* rovibronic levels of $CH_3S(\tilde{X}^2E_{3/2,1/2})$ are 2 and 1, respectively.[29] Rotational branches labelled as B = M, N, O, P, Q, R, S, T, and

U corresponding to rotational angular momentum changes of $\Delta N = N^+ - N'' = -4, -3, -2, -1, 0, 1, 2, 3,$ and 4, respectively, for $\Delta K = \pm 1$; and *P*, *Q*, and *R* corresponding to $\Delta N = -1, 0,$ and 1, respectively, for $\Delta K = \pm 2$, are assumed to be the probable ionization transitions. The transition probabilities for all these branches are assumed to be equal. The probabilities for transitions from different J'' levels within each branch are also assumed to be identical. For a given spin-orbit manifold ($^2E_{3/2}$ or $^2E_{1/2}$), we assume that the relative PE peak intensities [$I(B, J'')$] are calculated as

$$I(B, J'') = [(2J'' + 1)/Q_{rot}] \exp(-\Delta E_{rot}/kT_r), \quad (4)$$

where ΔE_{rot} is the rotational energy measured with respect to the lowest J'' level of the spin-orbit states [-127.15 cm^{-1} for $CH_3S(\tilde{X}^2E_{3/2})$ and +127.86 cm^{-1} for $CH_3S(^2E_{1/2})$] and Q_{rot} is the rotational partition function.

The energy expressions used are from Endo et al.[30] and ignore the Jahn-Teller effect. Taking into account the laser line width and the PFI effect on the width, the calculated line intensities are combined using a Gaussian lineshape with a FWHM of 4 cm^{-1}. Pertinent parameters used in the simulation of the spectra of Figs. 1(a) and 2(a) are summarized in Table I. The uncertainties for these parameters are determined by careful comparisons of the experimental and simulated PE spectra. When a given parameter used is within the range of the indicated uncertainties, the resulting simulated spectrum is indistinguishable from the best fit to the experimental spectrum.

The rotational constants, A = 5.68 cm^{-1} and B = 0.45 cm^{-1}, for CH_3S in its ground

Table I Parameters for CH_3S and CH_3S^+ used in the simulation of the N2P-PFI-PE spectra of $CH_3S(\tilde{X}^2E_{3/2,1/2})$ formed in the photodissociation of CH_3SH and CH_3SSCH_3.[a]

	$CH_3S(\tilde{X}^2E_{3/2,1/2})$					$CH_3S^+(\tilde{X}^3A_2)$	
	$A(cm^{-1})$[b]	$B(cm^{-1})$[b]	$^2E_{1/2}/^2E_{3/2}$	$T_r(^2E_{3/2})(K)$	$T_r(^2E_{1/2})(K)$	$A^+(cm^{-1})$	$B^+(cm^{-1})$
CH_3SH	5.68	0.45	0.5±0.1	200±100	250±100	5.578±0.10[c]	0.478±0.005[c]
						5.547±0.10[d]	0.470±0.010[d]
CH_3SSCH_3	5.68	0.45	1.1±0.2	800±200	900±200	5.578±0.10[c]	0.478±0.005[c]
						5.547±0.10[d]	0.470±0.010[d]

a) Other parameters used include IE[$CH_3S(\tilde{X}^2E_{3/2})$] = 74,726 ± 8 cm^{-1} (9.2649 ± 0.0010 eV), the spin-orbit splitting for $CH_3S(\tilde{X}^2E_{3/2,1/2})$ = 255.5 cm^{-1} (Ref. 26), and the relative Franck-Condon factors for ionization transitions, $CH_3S(\tilde{X},\nu_3=0) \rightarrow CH_3S^+(\tilde{X},\nu_3^+=0) : CH_3S(\tilde{X},\nu_3=0) \rightarrow CH_3S^+(\tilde{X},\nu_3^+=1) = 1.00 : 0.46$.

b) Values determined in a LIF study (Ref. 26).

c) Values for $CH_3S^+(\tilde{X}^3A_2, \nu_3^+ = 0)$.

d) Values for $CH_3S^+(\tilde{X}^3A_2, \nu_3^+ = 1)$.

state are obtained from Miller and co-workers.[26] The rotational constants A^+ and B^+ for $CH_3S^+(\tilde{X}^3A_2)$ are unknown. Based on the *ab initio* geometries for $CH_3S(\tilde{X})$ and $CH_3S^+(\tilde{X})$ obtained by the second order Møller Plesset (MP2) perturbation calculations using the 6-31G(d) basis set,[16] values for the rotational constants of $CH_3S(\tilde{X})$ and $CH_3S^+(\tilde{X})$ are found to be (A = 5.305 cm^{-1}, B = 0.445 cm^{-1}) and (A^+ = 5.181 cm^{-1}, B^+ = 0.466 cm^{-1}), respectively. Since the experimental and theoretical values for the rotational constants A and B are very close, we assume that the theoretical predictions for A^+ and B^+ have uncertainties similar to those observed experimentally. We find that the best fit for the PE bands centered at 74,459 and 74,716 cm^{-1} is observed for rotational constants A^+ = 5.55 ± 0.20 cm^{-1} and B^+ = 0.478 ± 0.005 cm^{-1} for $CH_3S^+(\tilde{X}^3A_2, \nu_3^+=0)$, which are obtained essentially by scaling the theoretical A^+ and B^+ values by factors of 1.071 and 1.026, respectively. Note that the latter factors are comparable to the ratios of 1.071 and 1.011 observed for the experimental to theoretical values of A and B, respectively. For $CH_3S^+(\tilde{X}^3A_2, \nu_3^+=1)$, the rotational constants used are A^+ = 5.55 ± 0.20 cm^{-1} and B^+ = 0.470 ± 0.010 cm^{-1}. The widths of the $CH_3S(\tilde{X}^2E_{3/2})$ and $CH_3(^2E_{1/2})$ PE bands resolved in Fig. 1(a) are found to be well-characterized by T_r = 200 ± 100 and 250 ± 100 K, respectively.

A population ratio of 0.5 ± 0.1 for $CH_3S(^2E_{1/2})/CH_3S(\tilde{X}^2E_{3/2})$ yields the best fit for the PFI-PE spectrum of Fig. 1(a). The absorption cross section for CH_3SH at around 265 nm (i.e., the photon energies of interest here) is unstructured and nearly constant. As pointed out above, the formation of CH_3S + H from the photodissociation of CH_3SH in this photon energy region is the dominant product channel.[31] Assuming that the PFI

detection efficiencies are the same for $CH_3S(\tilde{X}^2E_{3/2})$ and $CH_3S(^2E_{1/2})$, we conclude that for process (1) the relative populations are $CH_3S(^2E_{1/2})$: $CH_3S(\tilde{X}^2E_{3/2})$ = 0.5 : 1.0.

The energy of 74,726 cm^{-1} used in the simulation for the lowest possible transition, $CH_3S(\tilde{X}^2E_{3/2}) \rightarrow CH_3S^+(\tilde{X}^3A_2)$, is taken to be the IE of $CH_3S(\tilde{X}^2E_{3/2})$. After taking into account the resolution of the ionization laser, the Stark shift effect, and the effects on the IE due to the uncertainties of A^+ ($\pm$ 0.2 cm^{-1}), B^+ ($\pm$ 0.005 cm^{-1}), and T_r ($\pm$ 100 K), we assign an uncertainty of $\pm$8 cm^{-1} for the IE's of CH_3S. Using the spin-orbit splitting of 255.5 cm^{-1}, we obtain IE[$CH_3S(\tilde{X}^2E_{3/2})$] = 74,726 $\pm$ 8 cm^{-1} (9.2649 $\pm$ 0.0010 eV) and IE[$CH_3S(^2E_{1/2})$] = 74,471 $\pm$ 8 cm^{-1} (9.2333 $\pm$ 0.0010 eV). The IE[$CH_3S(\tilde{X}^2E_{3/2})$] value is in excellent agreement with the value of 9.262 $\pm$ 0.005 eV obtained in a gas cell VUV photoionization mass spectrometric experiment in which the CH_3S radicals were prepared by the reaction of F with CH_3SH. The value of 9.225 $\pm$ 0.014 eV determined in the experiment of Nourbakhsh et al.[21], which used a laser photodissociation supersonic radical source, agrees with the value for IE[$CH_3S(^2E_{1/2})$]. In the latter experiment, CH_3S radicals were prepared by 193nm photodissociation of CH_3SCH_3 in the high pressure region of a free jet. The agreement of the IE value obtained by Nourbakhsh et al. with the IE[$CH_3S(^2E_{1/2})$] determined here indicates that spin-orbit excited $CH_3S(^2E_{1/2})$ radicals are formed by 193nm photodissociation of CH_3SCH_3, and that the relaxation of spin-orbit excited $CH_3S(^2E_{1/2})$ radicals is inefficient in a supersonic expansion. This conclusion is in accord with the observation of the previous LIF studies of CH_3S.[26,27]

The relative Franck-Condon factors for ionization transitions, $CH_3S(\tilde{X}, \nu_3=0) \rightarrow CH_3S^+(\tilde{X}, \nu_3^+=0)$: $CH_3S(\tilde{X}, \nu_3=0) \rightarrow CH_3S^+(\tilde{X}, \nu_3^+=1)$ is determined to be 1.00 : 0.46.

Using the IEs for the transitions from $CH_3S(\tilde{X}^2E_{3/2})$ to the $\nu_3^+ = 0, 1$ states of $CH_3S^+(\tilde{X}^3A_2)$, we obtain a value of 733 ± 5 cm^{-1} for the ν_3^+ vibrational spacing of $CH_3S^+(\tilde{X}^3A_2)$. The latter value is higher than the *ab initio* prediction of 698 cm^{-1}.[16]

The simulated PE spectrum for $CH_3S(\tilde{X}^2E_{3/2,1/2})$ from CH_3SH is shown in Fig. 3(b). The experimental PE bands [Fig. 3(a)] for the ionization transitions $CH_3S(\tilde{X}^2E_{3/2,1/2}) \rightarrow CH_3S^+(\tilde{X}^3A_2, \nu_3^+=0)$ are well reproduced by the theoretical fit. The experimental PE bands for the ionization transition $CH_3S(\tilde{X}^2E_{3/2,1/2}) \rightarrow CH_3S^+(X^3A_2, \nu_3^+=1)$ are also in good agreement with the theoretical fit, except for some minor details. Minor disagreements between the experimental and simulated spectra can be attributed to local perturbations of autoionization processes. The good fit observed between the experimental and simulated spectra suggests that the characterization of the rotational populations of nascent $CH_3S(\tilde{X}^2E_{3/2,1/2})$ radicals formed by process (1) by equilibrium T_r's is a good approximation and that the autoionization dynamics for CH_3S are not particularly sensitive to the rotational levels of CH_3S.

In order to shed light on the photoionization dynamics of $CH_3S(\tilde{X}^2E_{3/2,1/2})$, the simulated spectrum is decomposed into the five components shown as five curves in Fig. 3(b). Four components are due to $\Delta K = \pm 1$ with $|\Delta N| \leq 1$, $|\Delta N| = 2$, $|\Delta N| = 3$, and $|\Delta N| = 4$, respectively, and one component results from $\Delta K = \pm 2$ and $|\Delta N| \leq 1$. The PE band for $CH_3S(\tilde{X}^2E_{3/2})$ exhibits more structure than that for $CH_3S(^2E_{1/2})$, as confirmed by the simulated spectrum. The simulation suggests that the two strong peaks at 37,355 and 37,367 cm^{-1} in the $CH_3S(\tilde{X}^2E_{3/2})$ PE band are attributable to $\Delta N = -1$ and $\Delta N = 0, 1$, respectively, for $\Delta K = \pm 1$. The shoulders at 37,325; 37,334; 37,345; and

Figure 3 (a) Enlarged view of the N2P-PFI-PE spectrum in the region of 37,100-37,800cm^{-1} for nascent $CH_3S(\tilde{X}^2E_{3/2,1/2})$ radicals formed by the photodissociation of CH_3SH.
(b) The best simulated spectrum for Fig. 3(a). The parameters used in the simulation are summarized in Table I. The simulated spectrum is decomposed into five components as shown. Four components are due to $\Delta K = \pm 1$ with $|\Delta N| \leq 1$ [(1)], $|\Delta N| = 2$ [(2)], $|\Delta N| = 3$ [(3)], and $|\Delta N| = 4$ [(4)], respectively, and one component is from $\Delta K = \pm 2$ and $|\Delta N| \leq 1$ [(5)].

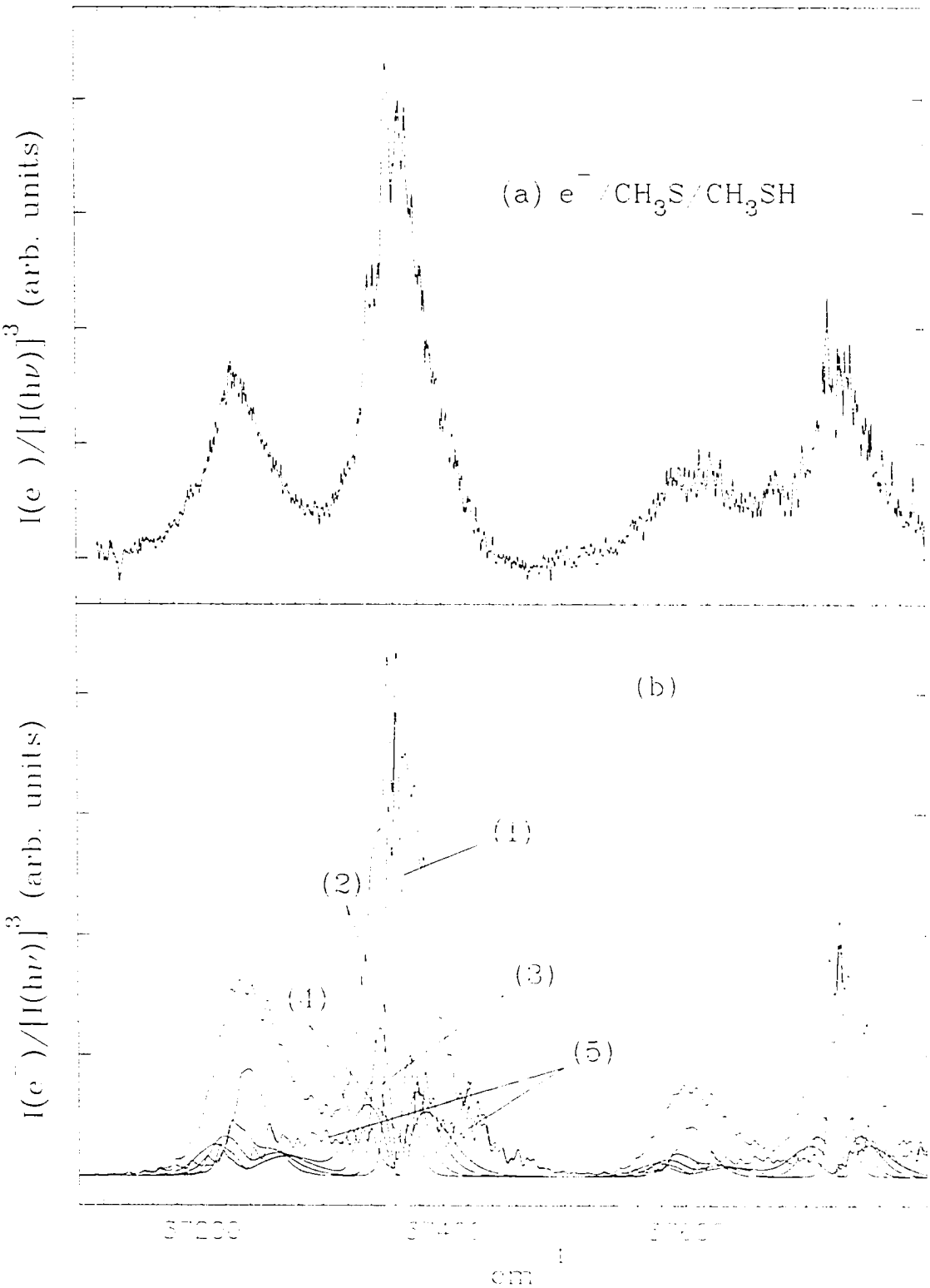
(a) e⁻/CH3S/CH3SH
I(e⁻)/[I(hν)]³ (arb. units)
(b)
(1)
(2)
(3)
(4)
(5)
I(e⁻)/[I(hν)]³ (arb. units)
cm⁻¹

37,372 cm^{-1} may be assigned to the respective transition of ΔN = -4, -3, -2, and +2, with $\Delta K = \pm 1$. The shoulders at 37,378 and 37,384 cm^{-1} resolved in the experimental band are also reproduced in the simulated spectrum, which suggests that these features may be due to the transitions ΔN = 3, 4 for $\Delta K = \pm 1$. In addition, note that two of the peaks from $|\Delta N| \leq 1$ with $\Delta K = \pm 2$ are predicted to appear at the same position and thus may also contribute to these observed features. The rotational branches $|\Delta N| > 1$ with $\Delta K = \pm 2$ contribute nearly constant intensities throughout the spectrum. For this reason, they are not included in the simulation.

The simulation is also performed for the N2P-PFI-PE spectrum of CH_3S produced from photodissociation of CH_3SSCH_3. The parameters used are the same as those for simulating the spectrum of Fig. 1(a), except for the T_r values and relative populations for the spin-orbit states $CH_3S(\tilde{X}^2E_{3/2})$ and $CH_3S(^2E_{1/2})$. We find that the widths of the $CH_3S(\tilde{X}^2E_{3/2})$ and $CH_3S(^2E_{1/2})$ PE bands observed in Fig. 1(a) correspond T_r = 800 ± 200 and 900 ± 200 K, respectively, while the relative intensities for the $CH_3S(\tilde{X}^2E_{3/2})$ and $CH_3S(^2E_{1/2})$ PE bands are consistent with a value of 1.1 ± 0.2 for the population ratio $CH_3S(^2E_{1/2})/CH_3S(\tilde{X}^2E_{3/2})$.

The simulated spectrum for $CH_3S(\tilde{X}^2E_{3/2,1/2})$ from CH_3SSCH_3 is shown in Fig. 4(b). The general profile of the experimental spectrum [Fig. 4(a)] is roughly reproduced by the simulated spectrum. Similar to the analysis of the N2P-PFI-PE spectrum for CH_3S from CH_3SH, the contributions to the simulated spectrum for CH_3S from CH_3SSCH_3 are also decomposed into the five components shown in Fig. 4(b). A noticeable peak at 37,316 cm^{-1} may be attributed to the rotational branch ΔN = -3 for $\Delta K = \pm 1$. This feature is

Figure 4 (a) Enlarged view of the N2P-PFI-PE spectrum in the region of 37,100-37,800cm^{-1} for nascent $CH_3S(\tilde{X}^2E_{3/2,1/2})$ radicals formed by the photodissociation of CH_3SSCH_3.
(b) The best simulated spectrum for Fig. 4(a). The parameters used in the simulation are summarized in Table I. The simulated spectrum is decomposed into five components as shown. Four components are due to $\Delta K = \pm 1$ with $|\Delta N| \leq 1$ [(1)], $|\Delta N| = 2$ [(2)], $|\Delta N| = 3$ [(3)], and $|\Delta N| = 4$ [(4)], respectively, and one component is from $\Delta K = \pm 2$ and $|\Delta N| \leq 1$ [(5)].

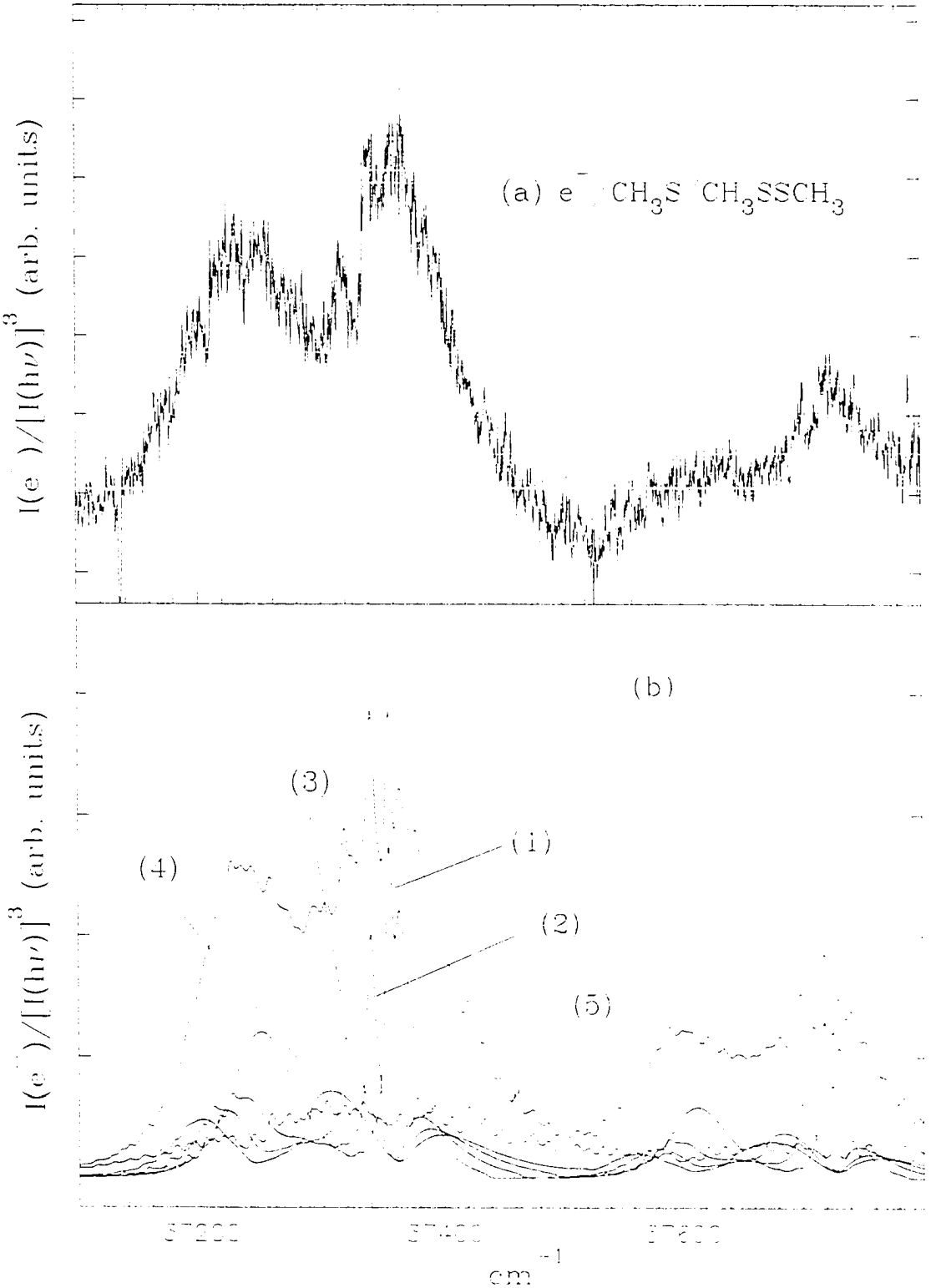
(a) e⁻ + CH3S + CH3SSCH3
I(e⁻)/[I(hν)]³ (arb. units)
(b)
(1)
(2)
(3)
(4)
(5)
37200
37400
37600
cm⁻¹

very sensitive to variations in A^+ and B^+. Contrary to the simulated spectrum which shows three resolved peaks in the region 37,340-37,380 cm^{-1}, the experimental spectrum exhibits only two partially resolved broad peaks. We find a similar observation when comparing the simulated and experimental PE band in the region of 37,710-37,750 cm^{-1}. The conclusion that the autoionization processes for CH_3S are relatively insensitive to the rotational levels obtained in the simulation of the PE spectrum of CH_3S from CH_3SH should also apply here. If this conclusion is valid, the difference between the experimental and simulated spectra is most likely due to the non-equilibrium rotational distributions for $CH_3S(\tilde{X}^2E_{3/2,1/2})$ from CH_3SSCH_3.

One of the conclusions obtained from the simulation of the N2P-PFI-PE spectra of CH_3S from processes (1) and (2) is that T_r for nascent $CH_3S(\tilde{X}^2E_{3/2,1/2})$ radicals formed from CH_3SH is significantly lower than for those formed from CH_3SSCH_3. The can be qualitatively explained using the impulsive model[32,33] of molecular dissociation. This model assumes that the molecule breaks apart due to vibrational motion without general equilibration of internal energies. For a triatomic molecule $\alpha\beta\gamma$ that dissociates into α + $\beta\gamma$, this model implies that the atoms of dissociating bond α-β recoil sharply before atom γ has time to respond. Thus, E_{av} is partitioned between the recoiling atoms α and β according to the conservation of linear momentum. The energy acquired by β manifests as translation (E_t), rotation (E_r), and vibration (E_v) of the $\beta\gamma$ fragment through the inelastic collision of β and γ.[34]

This model has been generalized to include dissociation of polyatomic molecules AB into fragments A and B, which may also be polyatomic species.[33] Assuming that AB

is bonded through atom α (in A) and atom β (in B), it can be shown that the energy partitioned into B [E_B] is[35]

$$E_B = (\mu/m_\beta)\, E_{av}, \tag{5}$$

where μ is the reduced mass of α and β and m_β is the mass of β. E_B is further partitioned into E_t, E_r, and E_v of B according to the equations:[35]

$$E_t(B) = (m_\beta/m_B)\, E_B \tag{6}$$

$$E_r(B) + E_v(B) = (1 - m_\beta/m_B)\, E_B \tag{7}$$

Considering further that B is a diatom β-γ, the internal energy can be separated into the rotational and vibrational components, as in the case of a triatomic molecule.

$$E_r(B) = (1 - m_\beta/m_B)\, E_B \sin^2\phi, \tag{8}$$

$$E_v(B) = (1 - m_\beta/m_B)\, E_B \cos^2\phi, \tag{9}$$

where ϕ is the A(α)-β-γ bond angle.

If we consider that the CH_3 group is a pseudo-atom of mass = 15 a.m.u., the rotational energies acquired by nascent CH_3S from CH_3SH and CH_3SSCH_3 can be

calculated using equation (8), provided that the geometries for the dissociating molecules are known. For the purpose of estimating the E_r value for CH_3S, we assume that the geometries for the dissociating CH_3SH and CH_3SSCH_3 are the same as those for their ground states. The ground state geometries for CH_3SH and CH_3SSCH_3 are obtained from *ab initio* calculations at the MP2/6-31G(d) level of theory.[20,36] In the case of CH_3SH, the theoretical and experimental structures are in good agreement.[37] Using the S-H bond energy of 86-90 kcal/mol[12,14,38] in CH_3SH, together with the *ab initio* geometry for $CH_3SH(\tilde{X}^1A')$, we obtain a value of ≈ 63 cm^{-1} for E_r of the CH_3S fragment at a photodissociation energy of 37,300 cm^{-1}. This E_r value of 63 cm^{-1} corresponds to $T_r \approx 63$ K, which is lower than the experimental T_r values of 200-250 K for $CH_3S(\tilde{X}^2E_{3/2,1/2})$ from CH_3SH. The cleavage of the S-S bond in CH_3SSCH_3 requires 74.8 kcal/mol.[11] Equation (7) predicts a value of ≈ 1709 cm^{-1} for E_r of CH_3S from CH_3SSCH_3, which translates into a $T_r \approx 1660$ K, significantly greater than the experimental T_r of 800-900 K for $CH_3S(\tilde{X}^2E_{3/2,1/2})$. The difference between experimental and predicted E_r's may be partly attributed to unrealistic assumption that the dissociation geometries for CH_3SH and CH_3SSCH_3 are the same as their equilibrium ground state structures. While the impulsive dissociation model gives predictions in qualitative agreement with experimental results, the model is not expected to yield accurate internal energy partitions because product electronic excitations have not been taken into account.

In IE measurements of polyatomic radicals, it is advantageous to prepare a cold radical beam. This experiment confirms the theoretical expectation that relatively cold polyatomic radicals can be prepared by photodissociation of molecular precursors when

the photodissociation involves the ejection of a light fragment, such as the hydrogen atom in process (1).

CONCLUSION

The N2P-PFI-PE spectra for CH_3S formed in the photodissociation of CH_3SH and CH_3SSCH_3 have been obtained near the ionization threshold of CH_3S. Both the $CH_3S(\tilde{X}^2E_{3/2})$ and $CH_3S(^2E_{1/2})$ spin-orbit states are formed in processes (1) and (2) with values of 0.5 $\pm$ 0.1 and 1.1 $\pm$ 0.2, respectively, for the ratio $CH_3S(^2E_{1/2})/CH_3S(\tilde{X}^2E_{3/2})$. From the simulation of the PFI-PE spectra for $CH_3S(\tilde{X}^2E_{3/2,1/2})$, we obtain estimates for the rovibronic state distributions of nascent $CH_3S(\tilde{X}^2E_{3/2,1/2})$ formed in the photodissociation wavelength range of 262-271 nm. As a good approximation, the rotational populations of CH_3S from CH_3SH and CH_3SSCH_3 can be characterized by T_r = 200-250 and 800-900 K, respectively. This experiment, together with the N2P-PFI-PE experiment of SH from H_2S, demonstrates that the PFI-PE technique can be used to probe the rovibronic state distribution of nascent photofragments.

The simulation also shows that the pulsed electric field induced autoionization processes for CH_3S are not very sensitive to the rotational level of $CH_3S(\tilde{X}^2E_{3/2,1/2})$. The IEs for $CH_3S(\tilde{X}^2E_{3/2})$ (74,726 $\pm$ 8 cm^{-1} or 9.2649 $\pm$ 0.0010 eV) and $CH_3S(^2E_{1/2})$ (74,471 $\pm$ 8 cm^{-1} or 9.2333 $\pm$ 0.0010 eV) and the C-S stretching frequency (733 $\pm$ 5 cm^{-1}) are determined with high accuracy.

ACKNOWLEDGEMENT

CYN acknowledge the Donors of the Petroleum Research Fund, administered by the American Chemical Society, for the partial support of this research. The authors are grateful to helpful discussions with Prof. T. A. Miller and Dr. M. G. White.

REFERENCES

(1) G. Reiser, W. Habenicht, K. Müller-Dethlefs, and E. W. Schlag, *Chem. Phys. Lett.* 152, 119 (1988).

(2) K. Müller-Dethefs, M. Sander, and E. W. Schlag, *Z. Naturforsch.* A 39, 1089 (1984); K. Müller-Dethefs and E. W. Schlag, *Annu. Rev, Phys. Chem.* 42, 109 (1991).

(3) I. Powis, T. Baer, and C. Y. Ng, Eds., "High Resolution Laser Photoionization and Photoelectron Studies" (Wiley, Chichester, 1994), in press.

(4) C.-W. Hsu, D. P. Baldwin, C.-L. Liao, and C. Y. Ng, *J. Chem. Phys.* 100, xxxx (1994).

(5) A. Stribel, I. Fischer, J. Staecker, G. Niedner-Schatteburg, K. Müller-Dethlefs and C. E. Bondybey, *J. Chem. Phys.* 97, 2332 (1992).

(6) I. Fischer, A. Lochschmidt, A. Strobel, G. Niedner-Schatteburg, K. Müller-Dethlefs, and V. E. Bondybey, *J. Chem. Phys.* 98, 3592 (1993).

(7) I. Fischer, A. Lochschmidt, A. Strobel, G. Niedner-Schatteburg, K. Müller-Dethelef, and V. E. Bondybey, *Chem. Phys. Lett.* 202, 542 (1993).

(8) A. Strobel, A. Lochschmidt, I. Fisher, G. Niedner-Schatteburg, and V. E. Bondybey, *J. Chem. Phys.* 99, 733 (1993).

(9) I. Fischer, A. Strobel, J. Staecher, G. Niedner-Schatteburg, K. Müller-Dethlefs, and V. E. Bondybey, *J. Chem. Phys.* 96, 7171 (1992).

(10) C.-W. Hsu, D. P. Baldwin, C.-L. Liao, and C. Y. Ng, "Laser Techniques for State-

Selected and State-to-State Chemistry II", J. W. Hepburn, ed., *SPIE Proc.* 2124 (1994), in press.

(11) S. Nourbakhsh, C.-L. Liao, and C. Y. Ng, *J. Chem. Phys.* 92, 6587 (1990).

(12) S. Nourbakhsh, K. Norwood, H.-M. Yin, C.-L. Liao, and C.Y. Ng, *J. Chem. Phys.* 95, 946 (1991).

(13) J. S. Keller, P. W. Kash, E. Jensen, and L. J. Butler, *J. Chem. Phys.* 96, 4324 (1992).

(14) J. Segall, Y. Wen, R. singer, M. Dulligan, and C. Wittig, *J. Chem. Phys.* 99, 6600 (1993).

(15) Y. R. Lee, C. L. Chiu, and S. M. Lin, *J. Chem. Phys.*, in press.

(16) S.-W. Chiu, W.-K. Li, W.-B. Tzeng, and C. Y. Ng, *J. Chem. Phys.* 97, 6557-6568 (1992).

(17) D. P. Chong and C. Y. Ng, *J. Chem. Phys.* 98, 759-760 (1993).

(18) L. A. Curtiss, R. H. Nobes, J. A. Pople, and L. Radom, *J. Chem. Phys.* 97, 6766 (1992).

(19) R. H. Nobes and L. Radom, *Chem. Phys. Lett.* 189, 554 (1992).

(20) D. R. Yarkony, *J. Chem. Phys.* 100, 3639 (1994) and references therein.

(21) S. Nourbakhsh, K. Norwood, G.-Z. He, and C. Y. Ng, *J. Am. Chem. Phys.* 113, 6311 (1991).

(22) B. Ruscic and J. Berkowitz, *J. Chem. Phys.* 97, 1818 (1992).

(23) C.-W. Hsu, C.-L. Liao, Z.-X. Ma, P. J. H. Tjossem, and C. Y. Ng, *Chem. Phys.*

Lett. 199, 78 (1992).

(24) C. W. Hsu, C.-L. Liao, Z.-X. Ma, P.J. H. Tjossem, and C. Y. Ng, *J. Chem. Phys.* 97, 6283 (1992).

(25) C. E. Moore, "Atomic Energy Levels", *Natl. Bur. Stand. (U.S.)* Circ. No. 467 (U.S. GPO, Washington, D.C. 1949), Vol. I.

(26) Y.-C. Hsu, X. Liu, and T. A. Miller, *J. Chem. Phys.* 90, 6852 (1989).

(27) S.-Y. Chiang and Y.-P. Lee, *J. Chem. Phys.* 95, 66 (1991).

(28) Using a rotational temperature (T_r) to characterize the rotational population of nascent CH_3S radicals is an approximation, in which equilibrium among the rotational levels is assumed.

(29) X.-M. Liu, C. P. Damo, T.-Y. Lin. S. C. Foster, P. Misra, L. Yu, and T. A. Miller, *J. Phys. Chem.* 93, 2266 (1989).

(30) Y. Endo, S. Saito, and E. Hirota, *J. Chem. Phys.* 81, 122 (1984).

(31) J. G. Calvert and J. N. Pitts, Jr., "Photochemistry" (Wiley, New York, 1966).

(32) G. E. Busch and K. R. Wilson, *J. Chem. Phys.* 56, 3626 (1972).

(33) K. A. Trentelman, S. H. Kable, D. B. Moss, and P. L. Houston, *J. Chem. Phys.* 91, 7498 (1989).

(34) Reference 32. The values for E_t, E_r, and E_v of fragment $\beta\gamma$ are calculated as: $E_t = (\mu_{\alpha\beta}/m_{\beta\gamma})\, E_{av}$, $E_r = (1 - \mu_{\alpha\beta}/\mu_f)\, E_{av} \sin^2\phi$, and $E_v = (1 - \mu_{\alpha\beta}/\mu_f)\, E_{av} \cos^2\phi$, where $\mu_{\alpha\beta}$ and μ_f are the reduced mass of atoms α and β and atom α and fragment $\beta\gamma$, respectively, and ϕ is the bond angle of α-β-γ.

(35) The expressions for the energies partitioned to A [E_A, $E_t(A)$, $E_r(A)$, and $E_v(A)$] are

similar to equations (5), (6) and (7).

(36) W.-K. Li, S.-W. Chiu, and Z.-X. Ma, and C. Y. Ng, *J. Chem. Phys.* 99, 8440 (1993).

(37) G. Herzberg, "Electronic Spectra and Electronic Structures of Polyatomic Molecules" (Van Nostrand Reinhold, New York, 1966).

(38) J. M. Nicovich, K. D. Kruetter, C. A. van Dijk, and P. H. Wine, *J. Phys. Chem.* 96, 2518 (1992).

GENERAL CONCLUSION

Using the 2+1 REMPI detection scheme for $S(^3P_{2,1,0};^1D_2)$, we have examined the 193 nm photodissociation of $CH_3S(\widetilde{X})$ and SH(X,v) prepared from processes (1) and (3), respectively.

$$CH_3SCH_3 + h\nu(193\ nm) \rightarrow CH_3S(\widetilde{X}) + CH_3, \quad (1)$$

$$CH_3S(\widetilde{X}) + h\nu(193\ nm) \rightarrow CH_3 + S(^3P_{2,1,0};^1D_2), \quad (2)$$

$$H_2S + h\nu(193\ nm) \rightarrow SH(X,v) + H, \quad (3)$$

$$SH(X,v) + h\nu(193\ nm) \rightarrow H(^2S) + S(^3P_{2,1,0};^1D_2). \quad (4)$$

The absolute photodissociation cross sections for CH_3S and SH at 193 nm are estimated to be 1×10^{-18} and 1.1×10^{-18} cm^2, respectively. The branching ratio $S(^3P):S(^1D)$ measured for process (2) is rationalized based on the potential energy curves along the CH_3-S dissociation coordinate using the MCSCF and FOCI methods. The branching ratio $S(^3P):S(^1D)$ measured for process (4) is consistent with the direct photodissociation mechanism for SH(X,v) via the excited repulsive $SH(^2\Sigma^-)$ and $SH(^2\Delta)$ surfaces, as proposed by Continetti et al[16]. The fine structure distributions $S(^3P_2):S(^3P_1):S(^3P_0)$ have been measured for processes (2) and (4) and are found to be 0.59 : 0.32 : 0.09 and 0.68 : 0.24 : 0.08, respectively.

The 193 nm photodissociation of $CH_3S(\widetilde{X})$ and SH(X,v) prepared from CH_3SH (processes (5) and (6)) have also been examined.

$$CH_3SH + h\nu(193\ nm) \rightarrow CH_3S(\widetilde{X}) + H, \quad (5)$$

$$CH_3SH + h\nu(193\ nm) \rightarrow SH(X,v) + CH_3 \quad (6)$$

The small difference in the branching ratios observed for CH_3S and SH, prepared from different parents, suggests the dependency of the branching ratios on the internal energy distributions of the intermediate radicals.

Using the N2P-PFI scheme, we have obtained the threshold PE spectra for SH and CH_3S at high resolution. The absorption cross section for the first-photon excitation for H_2S is continuous around 235 nm[17]. Therefore, the spectrum obtained by scanning the UV energy over this region reflects the cross section for the two-photon threshold photoionization of SH. Similarly, the spectrum obtained by scanning the UV energy over 267 nm for CH_3SH (Ref. 17) reflects the cross section for the two-photon threshold photoionization of CH_3S. The assignment of the rotationally resolved N2P-PFI-PE spectrum allows a highly accurate determination of the IE for SH. The improved value for the IE for CH_3S is also obtained from the simulation spectrum. To our knowledge, this is the first application of N2P threshold photoionization to the study of free radical species.

REFERENCES

(1) A. Levy, E. L. Merryman, and W. T. Reid, Environ. Sci. Technol. 4, 653 (1970).

(2) W. B. Tzeng, H.-M. Yin, W.-Y. Leung, J.-Y. Luo, S. Nourbakhsh, G. D. Flesch, and C. Y. Ng, J. Chem. Phys. 88, 1658 (1986).

(3) S. Nourbakhsh, C.-L. Liao, and C. Y. Ng, J. Chem. Phys. 92, 6587(1989).

(4) S. Nourbakhsh, K. Norwood, H.-M. Yin, C.-L. Liao, and C. Y. Ng, J. Chem. Phys. 95, 5014 (1991).

(5) S. Nourbakhsh, K. Norwood, H.-M. Yin, C.-L. Liao, and C. Y. Ng, J. Chem. Phys. 95, 946 (1991).

(6) S. Nourbakhsh, H.-M. Yin, C.-L. Liao, and C. Y. Ng, Chem. Phys. Lett. 183, 348 (1991).

(7) C.-L. Liao, C.-W. Hsu, and C. Y. Ng, *Optical Methods for Time- and State-Resolved Selective Chemistry*, C. Y. Ng, Editor, Proc.SPIE 1638, p. 245-253 (1992).

(8) C.-W. Hsu, C.-L. Liao, Z.-X. Ma, P. J. H. Tjossem, and C. Y. Ng, J. Chem. Phys. 97, 6283 (1992).

(9) C.-W. Hsu, C.-L. Liao, Z.-X. Ma, P. J. H. Tjossem, and C. Y. Ng, Chem. Phys. Lett. 199, 78 (1992).

(10) G. Resiser, W. Habenicht, K. Müller-Dethlefs, and E. W. Schlag, Chem. Phys. Lett. 152, 119 (1988).

(11) K, Müller-Dethlefs, M. Sander, and E. W. Schlag, Z. Naturforsch. Teil A 39,

1089 (1984).

(12) K, Müller-Dethlefs and E. W. Schlag, Annu. Rev. Phys. Chem. 42, 109 (1991).

(13) C.-W. Hsu, D. P. Baldwin, C.-L. Liao, and C. Y. Ng, *Optical Methods for Time- and State-Resolved Selective Chemistry*, C. Y. Ng, Editor, Proc.SPIE, in press.

(14) C.-W. Hsu, D. P. Baldwin, C.-L. Liao, and C. Y. Ng, J. Chem. Phys., in press.

(15) C.-W. Hsu and C. Y. Ng, J. Chem. Phys., to be submitted.

(16) R. E. Continetti, B. A. Balko, and Y. T. Lee, Chem. Phys. Lett. 185, 400 (1991).

(17) J. G. Calvert and J. N. Pitts, Jr., "*Photochemistry*" (Wiley, New York, 1966).

APPENDIX.

COMPUTER PROGRAMS

```
c     ************************************************************************
c     This program is designed to analyze the rotationally resolved
c     photoionization spectrum of HS. Rotational constants for neutral
c     (HS) are obtained from Ramsey. Rotational constants for ion (HS+)
c     are taken from Horani et al.
c     ************************************************************************

      Program HSrot3

      Real*4 HSn1(15,2),HSn2(15,2),HSi1(15,1),HSi2(15,1),HSi3(15,1)
      Real*4 TP1(15,2),TP2(15,2),TP3(15,2)
      Real*4 A0,Bvn,Dvn,Lambda,Beta,Bvi,Dvi,gamma,Lamb,Q1,Q2,IP,kB
      Integer*2 K,i,jj,NPoints
      Parameter (Lambda=1.,Bvn=9.461,Dvn=0.00048)
      Parameter (Bvi=9.134,Dvi=.000489)
      Parameter (IP=83888.7,NPoints=2101,kB=0.69503)
      Real*4 width,J,step,temp1,temp2,cc,nrgmin,spect(NPoints)
      Character Fname*10,Tfname*10,Filename*8
      common/BL1/step,nrgmin
      common/BL2/spect,Filename
      common/BL3/TP1,TP2,TP3,cc,width,K

c ***  main program  ***********************************

c  HSn1(*,0..1)  : F1 levels (pi 3/2 states) of neutral (HS)
c                  J=K+1/2
c  HSn2(*,0..1)  : F2 levels (pi 1/2 states) of neutral (HS)
c                  J=K-1/2
c  HSi1(*,0),HSi2(*,0), and HSi3(*,0) : F1, F2, and F3 levels
c                  (sigmma states) of ion (HS+)
c  TP1(*,0..1), TP2(*,0..1), and TP3(*,0..1) : transition energies and
c                  transtion probabilities from neutral ground state to the
c                  F1, F2, and F3 levels of ion ground state, respectively.
c  2nd subscripts for above arrays :  0 -> energy
c                                     1 -> intensity
c  Neutral rotational constants : A,Bvn,Dvn,Lambda,Beta,Y
c  ion rotational constants : Bvi,Dvi,gamma,Lamb
c  IP : ionization potential
c  step : step size (nm) in the simulation
c  nrgmin : minimun wavenumber (cm-1)
c  currentnrg : current wavenumber (cm-1)
c  width : Gaussian FWHM (cm-1)
c  NPoints : number of points in a scan
```

```
c   temp1,temp2 : neutral rotational temperature (K) (Pi3/2 & 1/2)
c   kB : Boltzmann constant (cm-1)
c   Q1, Q2 : Rotational partition functions
c   deltaw : the energy difference between currentnrg and peak position
c   spect(j) : spectrum for each branch
c   P11..R23 : 18 sub branches   delta K = 0,-1,+1
c   O11..S23 : 12 sub branches   delta K = -2,+2
c   N11..T23 : 12 sub branches   delta K = -3,+3
c   M11..M23 :  6 sub branches   delta K = -4
c   There are 16 rotational branches in the simulation (3 sub branches for
c   each branch) shown as follows:
c   P1..R2 : 6 branches
c   O1..S2 : 4 branches
c   N1..T2 : 4 branches
c   M1..M2 : 2 branches

      Fname='hszar1.eng'
      Tfname='hstran.eng'
      step=.002
      nrgmin=41550.
      width=1.0
      gamma=-.165
      Lamb=5.71
      A0=-376.96
      cc=-0.693147/(width*width)
      write(*,'(e9.3)')nrgmin
      write(*,*)' enter the temperature for Pi(3/2) and Pi(1/2):'
      read(*,'(2f10.3)')temp1,temp2

c   Calculate Pi(3/2) state energy

      Q1=0.
      write(*,*)'  J    K  rotational  Boltzmann'
      do 211 K=1,15
        J=K+.5
        Y=A0/Bvn
        Beta=0.5*sqrt(4*(J+0.5)*(J+0.5)+Y*(Y-4)*lambda*lambda)
        HSn1(K,0)=Bvn*((J+.5)*(J+.5)-lambda*lambda-Beta)
     *          -Dvn*J*J*J*J
        HSn1(K,1)=(2*J+1)*exp((-HSn1(K,0)+HSn1(1,0))/(kB*temp1))
        Q1=Q1+HSn1(K,1)
211     continue
      write(*,*)
```

```
c   Calculate Pi(1/2) state energy

      Q2=0.
      do 212 K=1,15
        J=K-.5
        Y=A0/Bvn
        Beta=0.5*sqrt(4*(J+0.5)*(J+0.5)+Y*(Y-4)*lambda*lambda)
        HSn2(K,0)=Bvn*((J+.5)*(J+.5)-lambda*lambda+Beta)
     *            -Dvn*(J+1)*(J+1)*(J+1)*(J+1)
        HSn2(K,1)=(2*J+1)*exp((-HSn2(K,0)+HSn2(1,0))/(kB*temp2))
        Q2=Q2+HSn2(K,1)
212     continue
      do 231 K=1,15
        HSn1(K,1)=HSn1(K,1)/Q1
        write(*,220)J,K,HSn1(K,0),HSn1(K,1)
220       format(f6.1,i4,2e12.5)
231     continue
      do 232 K=1,15
        HSn2(K,1)=HSn2(K,1)/Q2
        write(*,220)J,K,HSn2(K,0),HSn2(K,1)
232     continue
      write(*,*)

c   Calculate Sigmma(F1,F2,F3) state energy

      write(*,*)'  J    K  rotational '
      do 213 K=0,15
        J=K+1
        HSi1(K,0)=Bvi*K*(K+1)+Bvi*(2*K+3)-lamb-sqrt((2*K+3)*
     *    (2*K+3)*Bvi*Bvi+lamb*lamb-2*lamb*Bvi)+gamma*(K+1)
     *    -Dvi*K*K*(K+1)*(K+1)+IP
        write(*,221)J,K,HSi1(K,0)
221       format(f6.1,i4,e12.5)
213     continue
      write(*,*)
      do 214 K=1,15
        J=K
        HSi2(K,0)=Bvi*K*(K+1)-Dvi*K*K*(K+1)*(K+1)+IP
        write(*,221)J,K,HSi2(K,0)
214     continue
      do 215 K=1,15
        J=K-1
        HSi3(K,0)=Bvi*K*(K+1)-Bvi*(2*K-1)-lamb+sqrt((2*K-1)*
```

```
     *      (2*K-1)*Bvi*Bvi+lamb*lamb-2*lamb*Bvi)-gamma*K
     *      -Dvi*K*K*(K+1)*(K+1)+IP
            write(*,221)J,K,HSi3(K,0)
215         continue
            open(3,File=Fname,status='new')
            do 111 K=1,15
              J=K+.5
              write(3,220)J,K,HSn1(K,0),HSn1(K,1)
111         continue
            do 112 K=1,15
              J=K-.5
              write(3,220)J,K,HSn2(K,0),HSn2(K,1)
112         continue
            do 113 K=1,15
              J=K+1
              write(3,221)J,K,HSi1(K,0)
113         continue
            do 114 K=0,15
              J=K
              write(3,221)J,K,HSi2(K,0)
114         continue
            do 115 K=1,15
              J=K-1
              write(3,221)J,K,HSi3(K,0)
115         continue
            close(3)
            write(*,*)
            write(*,*)' writing the energy levels file into HStran.ENG'
            open(3,File=Tfname,status='new')

c  now calculate the P1 branch:

            write(*,*)'Constructing P1 spectrum'
            write(3,*)' P11 branch, delta J=-1/2,delta K=-1'
            write(3,*)'  J    K   Energy   Intensity'
            do 301 K=1,10
              J=K+.5
              TP1(K,0)=HSi1(K-1,0)-HSn1(K,0)
              TP1(K,1)=HSn1(K,1)
              write(3,411)J,K,TP1(K,0),TP1(K,1)
301         continue
411         format(f6.1,i4,2f14.5)
            write(3,*)' P12 branch, delta J=-3/2,delta K=-1'
```

```
      do 302 K=2,10
        J=K+.5
        TP2(K,0)=HSi2(K-1,0)-HSn1(K,0)
        TP2(K,1)=HSn1(K,1)
        write(3,411)J,K,TP2(K,0),TP2(K,1)
302     continue
      write(3,*)' P13 branch, delta J=-5/2,delta K=-1'
      do 303 K=2,10
        J=K+.5
        TP3(K,0)=HSi3(K-1,0)-HSn1(K,0)
        TP3(K,1)=HSn1(K,1)
        write(3,411)J,K,TP3(K,0),TP3(K,1)
303     continue
      call HS
      Filename='HS01.wei'
      call WriteFile
      call zero

c  now calculate the Q1 branch:

      write(*,*)'Constructing Q1 spectrum'
      write(3,*)' Q11 branch, delta J=1/2,delta K=0'
      do 304 K=1,10
        J=K+.5
        TP1(K,0)=HSi1(K,0)-HSn1(K,0)
        TP1(K,1)=HSn1(K,1)
        write(3,411)J,K,TP1(K,0),TP1(K,1)
304     continue
      write(3,*)' Q12 branch, delta J=-1/2,delta K=0'
      do 305 K=1,10
        J=K+.5
        TP2(K,0)=HSi2(K,0)-HSn1(K,0)
        TP2(K,1)=HSn1(K,1)
        write(3,411)J,K,TP2(K,0),TP2(K,1)
305     continue
      write(3,*)' Q13 branch, delta J=-3/2,delta K=0'
      do 306 K=1,10
        J=K+.5
        TP3(K,0)=HSi3(K,0)-HSn1(K,0)
        TP3(K,1)=HSn1(K,1)
        write(3,411)J,K,TP3(K,0),TP3(K,1)
306     continue
      call HS
```

```
      Filename='HS02.wei'
      call WriteFile
      call zero

c  now calculate the R1 branch:

      write(*,*)'Constructing R1 spectrum'
      write(3,*)' R11 branch, delta J=3/2,delta K=+1'
      do 307 K=1,10
        J=K+.5
        TP1(K,0)=HSi1(K+1,0)-HSn1(K,0)
        TP1(K,1)=HSn1(K,1)
        write(3,411)J,K,TP1(K,0),TP1(K,1)
307     continue
      write(3,*)' R12 branch, delta J=1/2,delta K=+1'
      do 308 K=1,10
        J=K+.5
        TP2(K,0)=HSi2(K+1,0)-HSn1(K,0)
        TP2(K,1)=HSn1(K,1)
        write(3,411)J,K,TP2(K,0),TP2(K,1)
308     continue
      write(3,*)' R13 branch, delta J=-1/2,delta K=+1'
      do 309 K=1,10
        J=K+.5
        TP3(K,0)=HSi3(K+1,0)-HSn1(K,0)
        TP3(K,1)=HSn1(K,1)
        write(3,411)J,K,TP3(K,0),TP3(K,1)
309     continue
      call HS
      Filename='HS03.wei'
      call WriteFile
      call zero

c  now calculate the P2 branch:

      write(*,*)'Constructing P2 spectrum'
      write(3,*)' P21 branch, delta J=1/2,delta K=-1'
      do 310 K=1,13
        J=K-.5
        TP1(K,0)=HSi1(K-1,0)-HSn2(K,0)
        TP1(K,1)=HSn2(K,1)
        write(3,411)J,K,TP1(K,0),TP1(K,1)
310     continue
```

```
      write(3,*)' P22 branch, delta J=-1/2,delta K=-1'
      do 311 K=2,13
        J=K-.5
        TP2(K,0)=HSi2(K-1,0)-HSn2(K,0)
        TP2(K,1)=HSn2(K,1)
        write(3,411)J,K,TP2(K,0),TP2(K,1)
311     continue
      write(3,*)' P23 branch, delta J=-3/2,delta K=-1'
      do 312 K=2,13
        J=K-.5
        TP3(K,0)=HSi3(K-1,0)-HSn2(K,0)
        TP3(K,1)=HSn2(K,1)
        write(3,411)J,K,TP3(K,0),TP3(K,1)
312     continue
      call HS
      Filename='HS04.wei'
      call WriteFile
      call zero

c  now calculate the Q2 branch:

      write(*,*)'Constructing Q2 spectrum'
      write(3,*)' Q21 branch, delta J=3/2,delta K=0'
      do 313 K=1,10
        J=K-.5
        TP1(K,0)=HSi1(K,0)-HSn2(K,0)
        TP1(K,1)=HSn2(K,1)
        write(3,411)J,K,TP1(K,0),TP1(K,1)
313     continue
      write(3,*)' Q22 branch, delta J=1/2,delta K=0'
      do 314 K=1,10
        J=K-.5
        TP2(K,0)=HSi2(K,0)-HSn2(K,0)
        TP2(K,1)=HSn2(K,1)
        write(3,411)J,K,TP2(K,0),TP2(K,1)
314     continue
      write(3,*)' Q23 branch, delta J=-1/2,delta K=0'
      do 315 K=1,10
        J=K-.5
        TP3(K,0)=HSi3(K,0)-HSn2(K,0)
        TP3(K,1)=HSn2(K,1)
        write(3,411)J,K,TP3(K,0),TP3(K,1)
315     continue
```

```
      call HS
      Filename='HS05.wei'
      call WriteFile
      call zero

c  now calculate the R2 branch:

      write(*,*)'Constructing R2 spectrum'
      write(3,*)' R21 branch, delta J=5/2,delta K=+1'
      do 316 K=1,10
        J=K-.5
        TP1(K,0)=HSi1(K+1,0)-HSn2(K,0)
        TP1(K,1)=HSn2(K,1)
        write(3,411)J,K,TP1(K,0),TP1(K,1)
316     continue
      write(3,*)' R22 branch, delta J=3/2,delta K=+1'
      do 317 K=1,10
        J=K-.5
        TP2(K,0)=HSi2(K+1,0)-HSn2(K,0)
        TP2(K,1)=HSn2(K,1)
        write(3,411)J,K,TP2(K,0),TP2(K,1)
317     continue
      write(3,*)' R23 branch, delta J=1/2,delta K=+1'
      do 318 K=1,10
        J=K-.5
        TP3(K,0)=HSi3(K+1,0)-HSn2(K,0)
        TP3(K,1)=HSn2(K,1)
        write(3,411)J,K,TP3(K,0),TP3(K,1)
318     continue
      call HS
      Filename='HS06.wei'
      call WriteFile
      call zero

c  now calculate the O1 branch:

      write(*,*)'Constructing O1 spectrum'
      write(3,*)' O11 branch, delta J=-3/2,delta K=-2'
      do 319 K=2,10
        J=K+.5
        TP1(K,0)=HSi1(K-2,0)-HSn1(K,0)
        TP1(K,1)=HSn1(K,1)
        write(3,411)J,K,TP1(K,0),TP1(K,1)
```

```
319    continue
       write(3,*)' O12 branch, delta J=-5/2,delta K=-2'
       do 320 K=3,10
        J=K+.5
        TP2(K,0)=HSi2(K-2,0)-HSn1(K,0)
        TP2(K,1)=HSn1(K,1)
        write(3,411)J,K,TP2(K,0),TP2(K,1)
320    continue
       write(3,*)' O13 branch, delta J=-7/2,delta K=-2'
       do 321 K=3,10
        J=K+.5
        TP3(K,0)=HSi3(K-2,0)-HSn1(K,0)
        TP3(K,1)=HSn1(K,1)
        write(3,411)J,K,TP3(K,0),TP3(K,1)
321    continue
       call HS
       Filename='HS07.wei'
       call WriteFile
       call zero

c  now calculate the S1 branch:

       write(*,*)'Constructing S1 spectrum'
       write(3,*)' S11 branch, delta J=5/2,delta K=+2'
       do 322 K=1,10
        J=K+.5
        TP1(K,0)=HSi1(K+2,0)-HSn1(K,0)
        TP1(K,1)=HSn1(K,1)
        write(3,411)J,K,TP1(K,0),TP1(K,1)
322    continue
       write(3,*)' S12 branch, delta J=3/2,delta K=+2'
       do 323 K=1,10
        J=K+.5
        TP2(K,0)=HSi2(K+2,0)-HSn1(K,0)
        TP2(K,1)=HSn1(K,1)
        write(3,411)J,K,TP2(K,0),TP2(K,1)
323    continue
       write(3,*)' S13 branch, delta J=1/2,delta K=+2'
       do 324 K=1,10
        J=K+.5
        TP3(K,0)=HSi3(K+2,0)-HSn1(K,0)
        TP3(K,1)=HSn1(K,1)
        write(3,411)J,K,TP3(K,0),TP3(K,1)
```

```
324     continue
        call HS
        Filename='HS08.wei'
        call WriteFile
        call zero

c  now calculate the O2 branch:

        write(*,*)'Constructing O2 spectrum'
        write(3,*)' O21 branch, delta J=-1/2,delta K=-2'
        do 325 K=2,10
          J=K-.5
          TP1(K,0)=HSi1(K-2,0)-HSn2(K,0)
          TP1(K,1)=HSn2(K,1)
          write(3,411)J,K,TP1(K,0),TP1(K,1)
325     continue
        write(3,*)' O22 branch, delta J=-3/2,delta K=-2'
        do 326 K=3,10
          J=K-.5
          TP2(K,0)=HSi2(K-2,0)-HSn2(K,0)
          TP2(K,1)=HSn2(K,1)
          write(3,411)J,K,TP2(K,0),TP2(K,1)
326     continue
        write(3,*)' O23 branch, delta J=-5/2,delta K=-2'
        do 327 K=3,10
          J=K-.5
          TP3(K,0)=HSi3(K-2,0)-HSn2(K,0)
          TP3(K,1)=HSn2(K,1)
          write(3,411)J,K,TP3(K,0),TP3(K,1)
327     continue
        call HS
        Filename='HS09.wei'
        call WriteFile
        call zero

c  now calculate the S2 branch:

        write(*,*)'Constructing S2 spectrum'
        write(3,*)' S21 branch, delta J=7/2,delta K=+2'
        do 328 K=1,10
          J=K-.5
          TP1(K,0)=HSi1(K+2,0)-HSn2(K,0)
          TP1(K,1)=HSn2(K,1)
```

```
        write(3,411)J,K,TP1(K,0),TP1(K,1)
328     continue
       write(3,*)' S22 branch, delta J=5/2,delta K=+2'
       do 329 K=1,10
        J=K-.5
        TP2(K,0)=HSi2(K+2,0)-HSn2(K,0)
        TP2(K,1)=HSn2(K,1)
        write(3,411)J,K,TP2(K,0),TP2(K,1)
329     continue
       write(3,*)' S23 branch, delta J=3/2,delta K=+2'
       do 330 K=1,10
        J=K-.5
        TP3(K,0)=HSi3(K+2,0)-HSn2(K,0)
        TP3(K,1)=HSn2(K,1)
        write(3,411)J,K,TP3(K,0),TP3(K,1)
330     continue
       call HS
       Filename='HS10.wei'
       call WriteFile
       call zero

c  now calculate the N1 branch:

       write(*,*)'Constructing N1 spectrum'
       write(3,*)' N11 branch, delta J=-5/2,delta K=-3'
       do 331 K=3,10
        J=K+.5
        TP1(K,0)=HSi1(K-3,0)-HSn1(K,0)
        TP1(K,1)=HSn1(K,1)
        write(3,411)J,K,TP1(K,0),TP1(K,1)
331     continue
       write(3,*)' N12 branch, delta J=-7/2,delta K=-3'
       do 332 K=4,10
        J=K+.5
        TP2(K,0)=HSi2(K-3,0)-HSn1(K,0)
        TP2(K,1)=HSn1(K,1)
        write(3,411)J,K,TP2(K,0),TP2(K,1)
332     continue
       write(3,*)' N13 branch, delta J=-9/2,delta K=-3'
       do 333 K=4,10
        J=K+.5
        TP3(K,0)=HSi3(K-3,0)-HSn1(K,0)
        TP3(K,1)=HSn1(K,1)
```

```
        write(3,411)J,K,TP3(K,0),TP3(K,1)
333     continue
        call HS
        Filename='HS11.wei'
        call WriteFile
        call zero

c  now calculate the T1 branch:

        write(*,*)'Constructing T1 spectrum'
        write(3,*)' T11 branch, delta J=7/2,delta K=+3'
        do 334 K=1,10
          J=K+.5
          TP1(K,0)=HSi1(K+3,0)-HSn1(K,0)
          TP1(K,1)=HSn1(K,1)
          write(3,411)J,K,TP1(K,0),TP1(K,1)
334     continue
        write(3,*)' T12 branch, delta J=5/2,delta K=+3'
        do 335 K=1,10
          J=K+.5
          TP2(K,0)=HSi2(K+3,0)-HSn1(K,0)
          TP2(K,1)=HSn1(K,1)
          write(3,411)J,K,TP2(K,0),TP2(K,1)
335     continue
        write(3,*)' T13 branch, delta J=3/2,delta K=+3'
        do 336 K=1,10
          J=K+.5
          TP3(K,0)=HSi3(K+3,0)-HSn1(K,0)
          TP3(K,1)=HSn1(K,1)
          write(3,411)J,K,TP3(K,0),TP3(K,1)
336     continue
        call HS
        Filename='HS12.wei'
        call WriteFile
        call zero

c  now calculate the N2 branch:

        write(*,*)'Constructing N2 spectrum'
        write(3,*)' N21 branch, delta J=-3/2,delta K=-3'
        do 337 K=3,10
          J=K-.5
          TP1(K,0)=HSi1(K-3,0)-HSn2(K,0)
```

```
        TP1(K,1)=HSn2(K,1)
        write(3,411)J,K,TP1(K,0),TP1(K,1)
337     continue
      write(3,*)' N22 branch, delta J=-5/2,delta K=-3'
      do 338 K=4,10
        J=K-.5
        TP2(K,0)=HSi2(K-3,0)-HSn2(K,0)
        TP2(K,1)=HSn2(K,1)
        write(3,411)J,K,TP2(K,0),TP2(K,1)
338     continue
      write(3,*)' N23 branch, delta J=-7/2,delta K=-3'
      do 339 K=4,10
        J=K-.5
        TP3(K,0)=HSi3(K-3,0)-HSn2(K,0)
        TP3(K,1)=HSn2(K,1)
        write(3,411)J,K,TP3(K,0),TP3(K,1)
339     continue
      call HS
      Filename='HS13.wei'
      call WriteFile
      call zero

c  now calculate the T2 branch:

      write(*,*)'Constructing T2 spectrum'
      write(3,*)' T21 branch, delta J=9/2,delta K=+3'
      do 340 K=1,10
        J=K-.5
        TP1(K,0)=HSi1(K+3,0)-HSn2(K,0)
        TP1(K,1)=HSn2(K,1)
        write(3,411)J,K,TP1(K,0),TP1(K,1)
340     continue
      write(3,*)' T22 branch, delta J=7/2,delta K=+3'
      do 341 K=1,10
        J=K-.5
        TP2(K,0)=HSi2(K+3,0)-HSn2(K,0)
        TP2(K,1)=HSn2(K,1)
        write(3,411)J,K,TP2(K,0),TP2(K,1)
341     continue
      write(3,*)' T23 branch, delta J=5/2,delta K=+3'
      do 342 K=1,10
        J=K-.5
        TP3(K,0)=HSi3(K+3,0)-HSn2(K,0)
```

```
        TP3(K,1)=HSn2(K,1)
        write(3,411)J,K,TP3(K,0),TP3(K,1)
342     continue
       call HS
       Filename='HS14.wei'
       call WriteFile
       call zero

c  now calculate the M1 branch:

       write(*,*)'Constructing M1 spectrum'
       write(3,*)' M11 branch, delta J=-7/2,delta K=-4'
       do 343 K=4,10
         J=K+.5
         TP1(K,0)=HSi1(K-4,0)-HSn1(K,0)
         TP1(K,1)=HSn1(K,1)
         write(3,411)J,K,TP1(K,0),TP1(K,1)
343     continue
       write(3,*)' M12 branch, delta J=-9/2,delta K=-4'
       do 344 K=5,10
         J=K+.5
         TP2(K,0)=HSi2(K-4,0)-HSn1(K,0)
         TP2(K,1)=HSn1(K,1)
         write(3,411)J,K,TP2(K,0),TP2(K,1)
344     continue
       write(3,*)' M13 branch, delta J=-11/2,delta K=-4'
       do 345 K=5,10
         J=K+.5
         TP3(K,0)=HSi3(K-4,0)-HSn1(K,0)
         TP3(K,1)=HSn1(K,1)
         write(3,411)J,K,TP3(K,0),TP3(K,1)
345     continue
       call HS
       Filename='HS15.wei'
       call WriteFile
       call zero

c  now calculate the M2 branch:

       write(*,*)'Constructing M2 spectrum'
       write(3,*)' M21 branch, delta J=-5/2,delta K=-4'
       do 346 K=4,10
         J=K-.5
```

```
      TP1(K,0)=HSi1(K-4,0)-HSn2(K,0)
      TP1(K,1)=HSn2(K,1)
      write(3,411)J,K,TP1(K,0),TP1(K,1)
346   continue
      write(3,*)' M22 branch, delta J=-7/2,delta K=-4'
      do 347 K=5,10
      J=K-.5
      TP2(K,0)=HSi2(K-4,0)-HSn2(K,0)
      TP2(K,1)=HSn2(K,1)
      write(3,411)J,K,TP2(K,0),TP2(K,1)
347   continue
      write(3,*)' M23 branch, delta J=-9/2,delta K=-4'
      do 348 K=5,10
      J=K-.5
      TP3(K,0)=HSi3(K-4,0)-HSn2(K,0)
      TP3(K,1)=HSn2(K,1)
      write(3,411)J,K,TP3(K,0),TP3(K,1)
348   continue
      call HS
      Filename='HS16.wei'
      call WriteFile
      close(3)
      End


c     ***********************************************************************
c     This subroutine is used to save a spectrum (a rotational branch)
c     into a data file ( HSxx.wei ).
c     ***********************************************************************

      Subroutine WriteFile
      Integer*2 NPoints,I
      Parameter (NPoints=2101)
      Real*4 Y(NPoints)
      Character*8 Filename
      common/BL2/Y,Filename
      write(*,520) Filename
520    format(' writing spectrum to this directory as ',a8)
      open(5,File=Filename,status='new')
      do 110 i=0,NPoints-1
       write(5,'(e11.4)')Y(I)
110   continue
      write(*,*)
```

```
      close(5)
      return
      end


c   ***************************************************************************
c     This subroutine is used to calculate a spectrum (a rotational branch)
c     for a transition HS+ <- HS.
c   ***************************************************************************

      Subroutine HS
      Integer*2 K,i,jj,NPoints
      parameter (NPoints=2101)
      Real*4 TP1(15,2),TP2(15,2),TP3(15,2),spect(NPoints)
      Real*4 cc,nrgmin,currentnrg,Deltaw,sum1,sum2,sum3,width,J,step
      character Filename*8
      common/BL1/step,nrgmin
      common/BL2/spect,Filename
      common/BL3/TP1,TP2,TP3,cc,width,K
      do 515 i=0,NPoints-1
        sum1=0.0
        sum2=0.0
        sum3=0.0
        currentnrg=1.0e7/(-step*i+1.0e7/nrgmin)*2
        do 516 jj=1,K
          Deltaw=currentnrg-TP1(jj,0)
          If (abs(Deltaw).lt.(5.0*width)) then
            sum1=sum1+10.0*TP1(jj,1)*exp(cc*Deltaw*Deltaw)
          endif
          Deltaw=currentnrg-TP2(jj,0)
          If (abs(Deltaw).lt.(5.0*width)) then
            sum2=sum2+10.0*TP2(jj,1)*exp(cc*Deltaw*Deltaw)
          endif
          Deltaw=currentnrg-TP3(jj,0)
          If (abs(Deltaw).lt.(5.0*width)) then
            sum3=sum3+10.0*TP3(jj,1)*exp(cc*Deltaw*Deltaw)
          endif
516       continue
        spect(i)=sum1+sum2+sum3
515     continue
      return
      end
```

```
c   ***************************************************************************
c     This subroutine is used to reset the transition energies and transition
c     probabilities of all rotational branches to zero.
c   ***************************************************************************

      Subroutine zero
      Real*4 TP1(15,2),TP2(15,2),TP3(15,2),cc,width
      Integer*2 K
      common/BL3/TP1,TP2,TP3,cc,width,K
      do 1 i=1,5
        TP1(i,0)=0.
        TP1(i,1)=0.
        TP2(i,0)=0.
        TP2(i,1)=0.
        TP3(i,0)=0.
        TP3(i,1)=0.
1     continue
      return
      end
```

```
c     ************************************************************************
c     This program is designed to analyze the photoionization spectrum
c     of SCH3. Rotational contants for neutral (E state) are obtained
c     from T.A. Miller et.al. Rotatioal contants for ion (A state) are
c     deduced from simulation.
c     ************************************************************************
c     Please read the file 'Readme.txt' listed on page 196 in order to
c     understand the structure of the program

      Program SCH3rot1

$include:'sch31.txt'
c  ***  main program  ***********************************
      An=5.68
      Bn=.45
      ALG=3.523
      Eaa=-3.809
      Ebc=-.2583
      nkLG=.00714
      neLG=.0000151
      DNn=.0000006372
      DNKn=.000008456
      DKn=.00008873
      aSO=-255.463
      aDSO=-.00281
      DNi=.0000006372
      DNKi=.000008456
      DKi=.00008873
      step=.002
      open(1,file='sch3.par',status='old')
      read(1,'(f10.3)')IP
      read(1,'(f10.3)')Ai
      read(1,'(f10.3)')Bi
      read(1,'(f10.3)')temp1
      read(1,'(f10.3)')temp2
      read(1,'(f10.3)')width
      read(1,'(f10.3)')ratio
      read(1,'(f10.3)')nrgmin
      close(1)
      cc=-0.693147/(width*width)

c  Calculate A state energy
```

```
      do 215 K=0,Kp
       do 216 N=K,Kp+8
        SCHi(N,K)=Bi*N*(N+1)+(Ai-Bi)*K*K-DNi*N*N*(N+1)*(N+1)
     * -DNKi*N*(N+1)*K*K-DKi*K*K*K*K+IP
216     continue
215    continue

c   Calculate E(3/2) state energy

      Q1=0.
      sigma=.5
      P=.5
      J=.5
      K=0
      SCHn0(0,0)=aSO*sigma+aDSO*K*K*sigma-2*ALG*K+neLG*K*(J*(J+1)-
     * 2*P*sigma+.75)+nkLG*K*K*K+An*K*K+Bn*(J*(J+1)-P*P+.5)-DNn*(J+.5)
     *  *(J+.5)*((J+.5)*(J+.5)-4*P*sigma+2)-DNKn*K*K*(J*(J+1)-2*P*sigma
     *  +.75)-DKn*K*K*K*K+Eaa*K*sigma-Ebc*.5
      do 211 K=-Kp,Kp
       P=K+sigma
       i=abs(K)
       do 212 N=i,Kp+8
        J=N+.5
      SCHn0(N,K)=aSO*sigma+aDSO*K*K*sigma-2*ALG*K+neLG*K*(J*(J+1)-
     * 2*P*sigma+.75)+nkLG*K*K*K+An*K*K+Bn*(J*(J+1)-P*P+.5)-DNn*(J+.5)
     *  *(J+.5)*((J+.5)*(J+.5)-4*P*sigma+2)-DNKn*K*K*(J*(J+1)-2*P*sigma
     *  +.75)-DKn*K*K*K*K+Eaa*K*sigma-Ebc*.5
      SCHn1(N,K)=(2*J+1)*exp((-SCHn0(N,K)+SCHn0(0,0))/(kB*temp1))
        if(mod(K,3).eq.1) SCHn1(N,K)=2*SCHn1(N,K)
        Q1=Q1+SCHn1(N,K)
212     continue
211    continue
      do 111 K=-Kp,Kp
       i=abs(K)
       do 121 N=i,Kp+8
        SCHn1(N,K)=SCHn1(N,K)/Q1
121     continue
111    continue
      m=1
      call SCH311
      Filename='SCH301.CWH'
      call WriteFile
      call SCH312
```

```
      Filename='SCH302.CWH'
      call WriteFile

c     Calculate E(1/2) state energy

      Q2=0.
      sigma=-.5
      P=-.5
      J=-.5
      K=0
      SCHn0(0,0)=aSO*sigma+aDSO*K*K*sigma-2*ALG*K+neLG*K*(J*(J+1)-
     * 2*P*sigma+.75)+nkLG*K*K*K+An*K*K+Bn*(J*(J+1)-P*P+.5)-DNn*(J+.5)
     *  *(J+.5)*((J+.5)*(J+.5)-4*P*sigma+2)-DNKn*K*K*(J*(J+1)-2*P*sigma
     *  +.75)-DKn*K*K*K*K+Eaa*K*sigma-Ebc*.5
      do 213 K=-Kp,Kp
        P=K+sigma
        i=abs(K)
        do 214 N=i,Kp+8
          J=N-.5
      SCHn0(N,K)=aSO*sigma+aDSO*K*K*sigma-2*ALG*K+neLG*K*(J*(J+1)-
     * 2*P*sigma+.75)+nkLG*K*K*K+An*K*K+Bn*(J*(J+1)-P*P+.5)-DNn*(J+.5)
     *  *(J+.5)*((J+.5)*(J+.5)-4*P*sigma+2)-DNKn*K*K*(J*(J+1)-2*P*sigma
     *  +.75)-DKn*K*K*K*K+Eaa*K*sigma-Ebc*.5
      SCHn1(N,K)=(2*J+1)*exp((-SCHn0(N,K)+SCHn0(0,0))/(kB*temp2))
          if(mod(K,3).eq.1) SCHn1(N,K)=2*SCHn1(N,K)
          Q2=Q2+SCHn1(N,K)
214     continue
213   continue
      do 112 K=-Kp,Kp
        i=abs(K)
        do 122 N=i,Kp+8
          SCHn1(N,K)=(SCHn1(N,K)/Q2)*ratio
122     continue
112   continue
      call SCH311
      Filename='SCH303.CWH'
      call WriteFile
      call SCH312
      Filename='SCH304.CWH'
      call WriteFile
      End
```

```
      Subroutine WriteFile
$include:'sch32.txt'
      write(*,521) Filename
521    format(' writing spectrum to this directory as ',a10)
      open(1,File=Filename,status='new')
      do 110 i=0,NPoints-1
       write(1,'(e12.5)')Y(I)
110    continue
      write(*,*)
      close(1)
      return
      end

      Subroutine SCH311
$include:'sch33.txt'
      If(m.eq.1) then
        Tfname='SCHtran1.eng'
        write(*,*)'Constructing p1(PQR) (delta |K| = -1) spectrum'
        open(3,File=Tfname,status='new')
      else
        Tfname='SCHtran3.eng'
        write(*,*)'Constructing p2(PQR) (delta |K| = -1) spectrum'
        open(3,File=Tfname,status='new')
       endif
c  now calculate the pP branch:
       do 301 K=1,Kp-1
        i=abs(K)
        do 1 N=i,Kp-1+8
          TP0(N,K)=SCHi(N-1,K-1)-SCHn0(N,K)
          TP1(N,K)=SCHn1(N,K)
          write(3,411)N,K,TP0(N,K),TP1(N,K)
1       continue
301    continue
411    format(2i5,2e12.5)
       do 501 i=0,NPoints-1
        sum=0.0
        currentnrg=1.0e7/(-step*i+1.0e7/nrgmin)*2
        do 601 iii=1,Kp-1
        ii=abs(iii)
        do 701 jj=ii,N
          Deltaw=currentnrg-TP0(jj,iii)
          If (abs(Deltaw).lt.(5.0*width)) then
            sum=sum+100.0*TP1(jj,iii)*exp(cc*Deltaw*Deltaw)
```

```
          endif
701       continue
601       continue
         spect(i)=sum
501     continue
c  now calculate the pQ branch:
       do 302 K=1,Kp-1
         i=abs(K)
         do 2 N=i,Kp-1+8
           TP0(N,K)=SCHi(N,K-1)-SCHn0(N,K)
           TP1(N,K)=SCHn1(N,K)
           write(3,411)N,K,TP0(N,K),TP1(N,K)
2         continue
302     continue
       do 502 i=0,NPoints-1
         sum=0.0
         currentnrg=1.0e7/(-step*i+1.0e7/nrgmin)*2
         do 602 iii=1,Kp-1
         ii=abs(iii)
         do 702 jj=ii,N
           Deltaw=currentnrg-TP0(jj,iii)
           If (abs(Deltaw).lt.(5.0*width)) then
             sum=sum+100.0*TP1(jj,iii)*exp(cc*Deltaw*Deltaw)
           endif
702       continue
602       continue
         spect(i)=sum+spect(i)
502     continue
c  now calculate the pR branch:
       do 303 K=1,Kp-1
         i=abs(K)
         do 3 N=i,Kp-1+8
           TP0(N,K)=SCHi(N+1,K-1)-SCHn0(N,K)
           TP1(N,K)=SCHn1(N,K)
           write(3,411)N,K,TP0(N,K),TP1(N,K)
3         continue
303     continue
       do 503 i=0,NPoints-1
         sum=0.0
         currentnrg=1.0e7/(-step*i+1.0e7/nrgmin)*2
         do 603 iii=1,Kp-1
         ii=abs(iii)
         do 703 jj=ii,N
```

```
          Deltaw=currentnrg-TP0(jj,iii)
          If (abs(Deltaw).lt.(5.0*width)) then
            sum=sum+100.0*TP1(jj,iii)*exp(cc*Deltaw*Deltaw)
          endif
703       continue
603       continue
        spect(i)=sum+spect(i)
503     continue
      close(3)
      m=m+1
      return
      end

      Subroutine SCH312
$include:'sch33.txt'
      If(m.eq.2) then
        Tfname='SCHtran2.eng'
        write(*,*)'Constructing r1(PQR) (delta |K| = +1) spectrum'
        open(3,File=Tfname,status='new')
      else
        Tfname='SCHtran4.eng'
        write(*,*)'Constructing r2(PQR) (delta |K| = +1) spectrum'
        open(3,File=Tfname,status='new')
      endif
c  now calculate the rP branch:
      do 304 K=-Kp+3,0
        i=abs(K)
        do 4 N=i+2,Kp-1+8
          TP0(N,K)=SCHi(N-1,i+1)-SCHn0(N,K)
          TP1(N,K)=SCHn1(N,K)
          write(3,411)N,K,TP0(N,K),TP1(N,K)
4       continue
304     continue
411     format(2i5,2e12.5)
      do 504 i=0,NPoints-1
        sum=0.0
        currentnrg=1.0e7/(-step*i+1.0e7/nrgmin)*2
        do 604 iii=-Kp+3.0
        ii=abs(iii)
        do 704 jj=ii+2,N
          Deltaw=currentnrg-TP0(jj,iii)
          If (abs(Deltaw).lt.(5.0*width)) then
            sum=sum+100.0*TP1(jj,iii)*exp(cc*Deltaw*Deltaw)
```

```
          endif
704       continue
604       continue
         spect(i)=sum
504     continue
c  now calculate the rQ branch:
       do 305 K=-Kp+3,0
         i=abs(K)
         do 5 N=i+1,Kp-1+8
           TP0(N,K)=SCHi(N,i+1)-SCHn0(N,K)
           TP1(N,K)=SCHn1(N,K)
           write(3,411)N,K,TP0(N,K),TP1(N,K)
5         continue
305     continue
       do 505 i=0,NPoints-1
         sum=0.0
         currentnrg=1.0e7/(-step*i+1.0e7/nrgmin)*2
         do 605 iii=-Kp+3,0
         ii=abs(iii)
         do 705 jj=ii+1,N
           Deltaw=currentnrg-TP0(jj,iii)
           If (abs(Deltaw).lt.(5.0*width)) then
             sum=sum+100.0*TP1(jj,iii)*exp(cc*Deltaw*Deltaw)
           endif
705       continue
605       continue
         spect(i)=sum+spect(i)
505     continue
c  now calculate the rR branch:
       do 306 K=-Kp+3,0
         i=abs(K)
         do 6 N=i,Kp-1+8
           TP0(N,K)=SCHi(N+1,i+1)-SCHn0(N,K)
           TP1(N,K)=SCHn1(N,K)
           write(3,411)N,K,TP0(N,K),TP1(N,K)
6         continue
306     continue
       do 506 i=0,NPoints-1
         sum=0.0
         currentnrg=1.0e7/(-step*i+1.0e7/nrgmin)*2
         do 606 iii=-Kp+3,0
         ii=abs(iii)
         do 706 jj=ii,N
```

```
          Deltaw=currentnrg-TP0(jj,iii)
          If (abs(Deltaw).lt.(5.0*width)) then
            sum=sum+100.0*TP1(jj,iii)*exp(cc*Deltaw*Deltaw)
          endif
706       continue
606       continue
         spect(i)=sum+spect(i)
506     continue
        close(3)
        m=m+1
        return
        end
```

Readme.txt

```
c  SCHn0(N,K)  : F1 levels (E 3/2 states) of neutral (SCH3) ,J=N+1/2
c                or  F2 levels (E 1/2 states) of neutral (SCH3) ,J=N-1/2
c       SCHn0 -> energy
c       SCHn1 -> intensity
c  SCHi(N,K)  : A state of ion(SCH3+), ignoring spin-rotation splitting
c  TP0(N,K) : Transition energy from neutral to ion
c  TP1(N,K) : Transition probability for TP0(N,K), It is determined by
c          Boltzmann distribution for nascent SCH3 and nuclear statistics
c  Neutral rotational constants : An,Bn,ALG,Eaa,Ebc,nkLG,neLG,DNn,
c                                 DNKn,DKn,aSO,aDSO
c  Ion rotational constants : Ai,Bi,DNi,DNKi,DKi
c  IP : ionization potential
c  ratio : (E3/2)/(E1/2)
c  step : step size (nm) in the simulation
c  nrgmin : minimun wavenumber (cm-1)
c  currentnrg : current wavenumber (cm-1)
c  width : Gaussian FWHM (cm-1)
c  NPoints : number of points in a scan
c  temp1,temp2 : neutral rotational temperature (K) (E 3/2 & 1/2)
c  kB : Boltzmann constant (cm-1)
c  Q1, Q2 : Rotational partition functions
c  deltaw : the energy difference between currentnrg and peak position
c  spect(j) : spectrum for each branch
c  The rotational branches are designated as follows:
c       p(small p)  -> delta K=-1
c       R(big R)    -> delta N=+1
c  i.e.  pR represents the branch : delta K=-1 and delta N=+1.
c     ***************************************************************
c     This program only calculates the branches pP, pQ, pR, rP, rQ, and
c     rR. The calculation for the other branches can be easily modified
c     by changing the delta N or delta K.
c     ***************************************************************
```

```
      sch31.txt
      Real*4 An,Bn,ALG,Eaa,Ebc,nkLG,neLG,DNn,DNKn,DKn,aSO,aDSO
      Real*4 Ai,Bi,DNi,DNKi,DKi,IP,sigma,width,ratio,temp1,temp2
      Real*4 cc,nrgmin,currentnrg,Deltaw,J,step,P,kB
      Integer*2 K,i,jj,ii,iii,N,m
      parameter(kB=0.69503)
      parameter(Ni=65,Ki=113,Kp=56,NPoints=2001)
      Real*4 SCHn0(Ni,Ki),SCHn1(Ni,Ki),SCHi(Ni,Ki)
      Real*4 TP0(Ni,Ki),TP1(Ni,Ki),spect(NPoints)
      Character Filename*10,Tfname*12
      common/BL1/spect,Filename
      common/BL2/SCHn0,SCHn1,SCHi,TP0,TP1
      common/BL3/cc,currentnrg,Deltaw,m,step,nrgmin,width

      sch32.txt
      Parameter (NPoints=2001)
      Real*4 Y(NPoints)
      Character*10 Filename
      common/BL1/Y,Filename

      sch33.txt
      parameter(Ni=65,Ki=113,Kp=56,NPoints=2001)
      Real*4 SCHn0(Ni,Ki),SCHn1(Ni,Ki),SCHi(Ni,Ki)
      Real*4 TP0(Ni,Ki),TP1(Ni,Ki),spect(NPoints)
      Real*4 cc,width,currentnrg,Deltaw,step,sum,nrgmin
      integer*2 m,i,ii,iii,jj
      character Tfname*12,Filename*10
      common/BL1/spect,Filename
      common/BL2/SCHn0,SCHn1,SCHi,TP0,TP1
      common/BL3/cc,currentnrg,Deltaw,m,step,nrgmin,width

c     Typical parameter file 'sch3.par' for simulating PE spectrum of
c     CH3S from CH3SH is shown as follows:

74594.
5.547
.478
200.
250.
4.
0.5
37060.
```